ADDITION OF HETEROALLENES TO METAL-NITROGEN BONDS AND SUBSEQUENT C-N BOND METATHESIS REACTIONS: A POTENTIAL ROUTE TO CARBON DIOXIDE CONVERSION

M. Tyler Caudle, Ryan J. McDonnell, and Nicholas A. Straessler

Department of Chemistry and Biochemistry
Arizona State University
Box 871604
Tempe, AZ 85287-1604

Introduction

The use of CO_2 as a C_1 synthon has inspired an expanding number of research publications. For example, there has been considerable success recently in the catalytic optimization of the well-known copolymerization of CO_2 and epoxides.[1] However, the field of CO_2 utilization is still limited by a small number of fundamental chemical strategies for its incorporation into new molecular units, and can therefore benefit from new research on strategies for the fixation of CO_2 to give value-added chemical products.

Carbon dioxide-based chemistry can benefit chemical synthesis by replacing toxic or expensive C_1 synthons. Isocyanates are intermediates in the synthesis of a number of chemical classes, including several important pharmaceutical and agricultural products, Figure 1.[2] Isocyanates are commercially prepared by phosgenation of amines, which has the dual advantages that the reaction proceeds to near completion and the coproducts are easy to separate. However, the potential chemical hazard and environmental risk associated with production, storage, and transport of five million metric tons of phosgene annually has inspired research on alternative routes for isocyanate production.[2] The only commercially applied alternative to date is the Du Pont production of methyl isocyanate using the reductive carbonylation of methylamine.[3] Carbon dioxide is at the same oxidation level as phosgene, and is a potential alternative C_1 agent in isocyanate preparation from amines.[4-6] This in turn provides a route for incorporation of CO_2 into molecules derived from isocyanates.

Synthetic routes involving CO_2 also provides access to specialty products not easily prepared by other means. Carbon dioxide is readily available as a variety of isotopomers, and is a primary synthon for selective isotopic enrichment of carbon atoms in compounds. This is important in the preparation of ^{14}C radiolabeled susbtrates for the study of enzyme catalysis and biochemical pathways, for the preparation of ^{13}C-enriched compounds for characterization of new molecules by magnetic resonance and vibrational spectroscopy, and for the preparation of ^{11}C-based radiopharmaceuticals. Thus reagents that efficiently absorb and activate carbon dioxide to give reactive chemical intermediates such as isocyanates have potential applications in the synthesis of specialty compounds isotopically enriched at specific carbon positions.

The first step in CO_2 utilization via this pathway is addition of CO_2 to a primary amine gives the corresponding carbamato anion **A**[-], Figure 2. A primary challenge in is to develop chemical reagents for the extraction of O^{2-} from the carbamate. This has been accomplished using a variety of oxophilic silanes,[7] phosphate/phosphines,[4] or anhydrides[5], which yield reactive esters **A*** that can cleave the C-O bond at modest temperatures to eliminate the corresponding isocyanate, RNCO. However, these are generally not commercially appealing due to the expense of the reagents. Carbamate anions exhibit rich coordination chemistry with transition and main group metal ions,[8] and coordination to oxophilic metal complexes has been shown to facilitate C-O bond cleavage in carbamates.[9] Metal-facilitated C-O bond cleavage in carbamato anions has a number of advantages, including the possibility that the metal center could be regenerated to give a closed loop for preparation of organic isocyanates. However, it also presents fundamental challenges in basic chemistry that must be addressed before the more practical aspects of the chemistry can be productively pursued. Notably, C-N bond cleavage in **A**[-] is generally favored over C-O bond cleavage,[10] and the precise chemical basis by which a metal ion electrophile favors C-O bond cleavage is not known. To address this question we need a clear understanding of the mechanism for both C-O and C-N bond cleavage reactivity in representative metal carbamato complexes, and of how the changes in the carbamato ligand and metal complex influence the bias between the two.

Experimental

Methods and materials. Dimethylzinc and tetrachlorotitanium were obtained from Aldrich and stored and handled under nitrogen atmosphere. Primary and secondary amines were distilled prior to use. CO_2 was obtained as 99.0% and dried by passing through a column of Drierite and then a column of P_2O_5 powder. Routine ^{1}H and ^{13}C NMR spectra were measured using a Varian 300MHz (proton frequency) instrument. Infrared spectra were measured using a Nicolet Avatar 360 instrument. Compositional analyses were performed in the ASU Center for Solid State Science.

Zinc Complexes. Zinc carbamate complexes were prepared by reaction of one equiv of a primary or secondary amine, RR'NH (R = alkyl/aryl, R' = alkyl/aryl/H) with excess carbon dioxide in the presence of 0.5 equiv dimethylzinc. Under strictly anaerobic and anhydrous conditions, this gives zinc complexes of the general form $[Zn(O_2CNRR')_2]_n$, which were characterized by their compositional analysis, NMR, and vibrational spectra. Careful stoichiometric hydrolysis of $[Zn(O_2CNRR')_2]_n$ gave the tetranuclear species $[Zn_4O(O_2CNRR')_6]$, which was characterized by similar methods. Zinc dithiocarbamato complexes were prepared by reaction of one equiv of a primary or secondary amine with CS_2 in the presence of 0.5 equiv zinc chloride.

**Figure 1.** Application of organic isocyanates in specialty chemical synthesis.
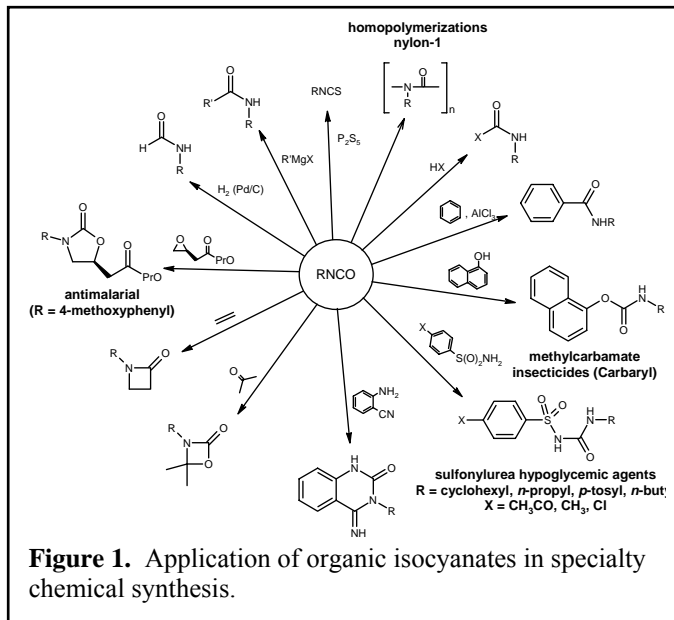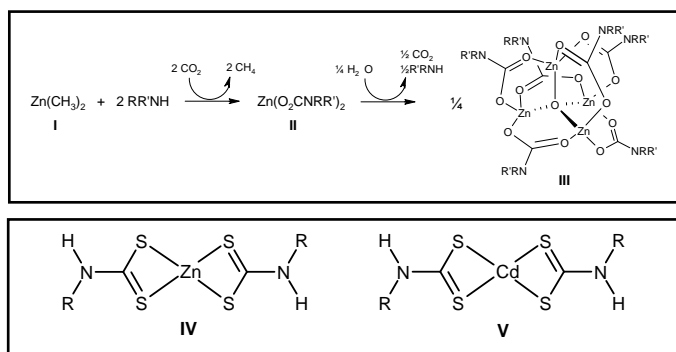
Titanium Complexes. Titanium carbamate complexes were prepared by reaction of one equiv of a primary or secondary amine, RR'NH (R = alkyl/aryl, R' = alkyl/aryl/H) with excess carbon dioxide in the presence of 0.25 equiv or 0.125 equiv tetrachlorotitanium.   Under strictly anaerobic and anhydrous conditions, this gives titanium complexes of the general form $[Ti(O_2CNRR')_2Cl_2]$ and $[Ti(O_2CNRR')_4]$, which were characterized by their compositional analysis, NMR, and vibrational spectra.

Results and Discussion

The one-pot condensation of dimethylzinc, an amine, and CO_2 gives the homoleptic carbamatozinc compounds **II**.   These are markedly unstable to hydrolysis and readily undergo reaction with H_2O to give **III**. Interestingly, compounds **III** are resistant to further hydrolysis, suggesting a clear correlation between the mode for coordination of the carbamato ligand and its chemical reactivity. The chemical reactivity of **II** and **III** are dominated by C-N bond cleavage reactions[11], and this is exemplified by the fact that the carboxyl group of **III** is readily exchanged with free $^{13}CO_2$. On the other hand, dithiocarbamatozinc derivatives of type **IV** are highly susceptible to cleavage of the C-S bond, which results in formation of the corresponding isothiocyanate derivative. Indeed, preparation of these compounds is complicated by the competition between formation of the dithiocarbamatozinc complex and its subsequent decomposition. This probably derives from the weaker dissociation energy of the C-S bond relative to the C-O bond, as well as to the thiophilic character of the Zn^{2+} ion. This is consistent with our previous work showing that cadmium derivatives **V** undergo very facile cleavage of the C-S bond to give the isothiocyanate product.[12] The C-O bond cleavage reactivity in **II** and **III** is sluggish, and appears to be in competition with C-N bond cleavage. Solid-state thermolysis of **II** leads to condensation of the alkylurea, but this probably proceeds initially via the carbamate anhydride **VI**, which subsequently rearranges to the urea and CO_2.
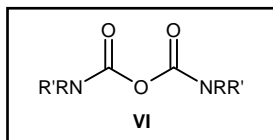

The chemistry of the titanium(IV) derivatives is markedly different. Condensation of $TiCl_4$ with excess secondary amine and CO_2 gives the tetrakis(carbamato)titanium complex **VII**, which is inert to C-O bond cleavage, although it does undergo exchange with free $^{13}CO_2$. However, condensation of $TiCl_4$ with a primary amine and CO_2 gives a substantial, though not quantitative, amount of the corresponding N,N'-dialkyurea **VIII**. Furthermore, addition of a primary amine to **VII** gives a mixture of the N,N'-dialkylurea **VIII** and N,N′,N′-trialkylurea **IX**. These observations
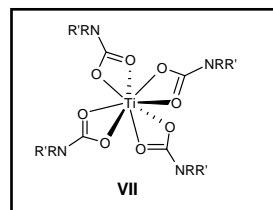
are most consistent with (1) exchange of the N,N-dialkylamino groups in **VII** with free primary amine,[11] (2) facile unimolecular C-O bond cleavage of the resulting coordinated N-alkylcarbamato ligand which is not possible for a dialkylcarbamato ligand, and (3) condensation of the resulting isocyanate with either free primary or secondary amine to give **VIII** or **IX**.
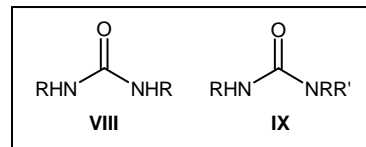
Conclusions

Simple inorganic and organometallic compounds are promising as reagents for CO_2 addition and subsequent deoxygenation by C-O bond cleavage. However, a more sophisticated understanding of this activity is a prerequisite for their application in practical CO_2 utilization chemistry.

References

(1) Darensbourg, D. J.; Rodgers, J. L.; Fang, C. C. *Inorg. Chem.* **2003**, *42*, 4498-4500; Darensbourg, D. J.; Yarbrough, J. C.; Ortiz, C.; Fang, C. C. *J. Am. Chem. Soc.* **2003**, *125*, 7586-7591; Qin, Z.; Thomas, C. M.; Lee, S.; Coates, G. W. *Angew. Chem., Int. Ed. Engl.* **2003**, *42*, 5484-5487; Moore, D. R.; Cheng, M.; Lobkovsky, E. B.; Coates, G. W. *J. Am. Chem. Soc.* **2003**, *125*, 11911-11924.
(2) Ulrich, H. *Chemistry and Technology of Isocyanates*; John Wiley & Sons: New York, 1996.
(3) Heinsohn, G. E.; Rao, V. N. M.: (du Pont de Nemours, E. I., and Co., USA). Methyl isocyanate production in a quartz reactor. US 4620030, 1986; Carcia, P. F.; Heinsohn, G. E.; Rao, V. N. M.: (du Pont de Nemours, E. I., and Co., USA). Catalytic conversion of formamides to isocyanates. US 4469640, 1984; Siefen, H. T.; Trutna, W. R.: (E. I. du Pont de Nemours & Co.). Methylformamide production at low pressures. US 2866822, 1958.
(4) Waldman, T. E.; McGhee, W. D. *Chem. Commun.* **1994**, 957-958; Saylik, D.; Horvath, M. J.; Elmes, P. S.; Jackson, W. R.; Lovel, C. G.; Moody, K. *J. Org. Chem.* **1999**, *64*, 3940-3946.
(5) McGhee, W. D.; Paster, M.; Riley, D.; Ruettimann, K.; Solodar, J.; Waldman, T. *ACS Symp. Ser.* **1996**, *626*, 49-58; Belforte, A.; Belli Dell'Amico, D.; Calderazzo, F. *Chem. Ber.* **1988**, *121*, 1891-1897.
(6) McGhee, W.; Riley, D.; Christ, K.; Pan, Y.; Parnas, B. *J. Org. Chem.* **1995**, *60*, 2820-2830; Riley, D.; McGhee, W. D.; Waldman, T. *ACS Symp. Ser.* **1994**, *577*, 122-132; Molina, P.; Alajarin, M.; Arques, A. *Synthesis* **1982**, 596-597.
(7) Hedaya, E.; Theodoropulos, S.: (Union Carbide Corp., USA). Halosilyl carbamates and isocyanates derived therefrom. CA 1108174, 1981.
(8) Belli Dell'Amico, D.; Calderazzo, F.; Labella, L.; Marchetti, F.; Pampaloni, G. *Chem. Rev.* **2003**, *103*, 3857-3897.
(9) Guiducci, A. E.; Cowley, A. R.; Skinner, M. E. G.; Mountford, P. *J. Chem. Soc., Dalton Trans.* **2001**, 1392-1394; Blake, A. J.; McInnes, J. M.; Mountford, P.; Nikonov, G. I.; Swallow, D.; Watkin, D. J. *J. Chem. Soc. Dalton Trans.* **1999**, 379-392; Dubberley, S. R.; Friedrich, A.; Willman, D. A.; Mountford, P.; Radius, U. *Chem.-Eur. J.* **2003**, *9*, 3634-3654; Babcock, J. R.; Liable-Sands, L.; Rheingold, A. L.; Sita, L. R. *Organometallics* **1999**, *18*, 4437-4441; Ciruelos, S.; Cuenca, T.; Gomez, R.; Gomez-Sal, P.; Manzanero, A.; Royo, P. *Organometallics* **1996**, *15*, 5577-5585.
(10) Rüger, C.; Schwetlick, K.; Kammer, H. *Z. Chem.* **1974**, *14*, 152.
(11) McCowan, C. S.; Caudle, M. T. *J. Chem. Soc., Dalton Trans.* **2004**, *in press.*
(12) Van Poppel, L.; Groy, T. L.; Caudle, M. T. *Inorg. Chem.* **2004**, *43*, 3180-3188.

METALLIC NANOFUELS: COMBUSTION IN THE SOLID STATE

D. B. Beach[1], B. G. Sumpter[2], S. D. Labinov[3]

[1]*Chemical Sciences Division*
[2]*Computer Science and Mathematics Division*
[3]*Engineering Science and Technology Division*
Oak Ridge National Laboratory
*Oak Ridge, TN 37831*

Introduction

Limited reserves of liquid fossil fuel, security issues due to foreign oil dependence, and the air pollution caused by the burning of fossil fuels are the major drivers for the search for alternative fuels for transportation. We suggest the use of engineered clusters of metallic nanoparticles as a fuel for vehicles. When compared to conventional liquids, this metallic fuel features greater energy capacity per volumetric unit, lower flammability, is virtually explosion, and does not require any special storage conditions. With the same size fuel tank, a vehicle using iron as a fuel will cover without refueling a distance two times greater than that covered by a car using gasoline, aluminum – three times greater and boron - five times greater! The combustion products of the metals are solid oxides that can easily be stored and transported to reduction facilities or directly reduced/recycled as part of the engine utilizing the energy produced. Metallic fuel, in spite of all of the advantages just mentioned, has not been used in vehicles with the exception for solid-propellant rocket boosters. Certain unique aspects of metal combustion account for this fact.[1] The process of metal oxidation with gaseous oxygen (air) is accompanied by the formation on the metal surface of an oxide film that prevents oxygen molecules entering into the zone of reaction. The passivating action of the film is increased with increasing film thickness. To avoid this phenomenon, the temperature of reaction has to be above the temperature for oxide film evaporation, about 2,500-3,000 K for the majority of metals. At this temperature, metal evaporation takes place on the surface and the oxidation reaction progresses in the gas phase. Outside of the high-temperature zone of combustion, the metal oxide is condensed and solidifies, forming particles of solid ash which is carried-over by the air flow and is deposited on the walls of a combustion chamber and other parts of an engine. Obviously, such a fuel is unfit for any conventional engine. The high temperature of metal combustion contributes to intensive formation of nitrogen oxides in the heated air thus adding to atmospheric pollution. Also, there are few structural materials that can stand the high temperature of metal combustion. In summary, the following problems have not yet been solved: (a) the control of the metallic fuel combustion process; (b) the quick decrease or increase of released heat quantity depending on engine load, and (c) systems providing for fuel delivery to a combustion chamber and for ash removal.

We have investigated a possible solution to these problems by using an engineered metallic fuel cluster composed of individual nano-particles. The underlying basis for this approach is that the ignition and combustion temperature of metallic particles[2] decreases rapidly with decreasing particle size, while the speed of combustion and intensity of heat release are increased. These desired effects are primarily due to the fact that as the particle size decreases, the surface-to-volume ratio rapidly increases. A cluster of nano-particles should thus be capable of providing the desired combustion properties of intensive and rapid heat release but occur at temperatures below 1600 K in the solid state without significant production of volatile species. The goal of this project was to experimentally verify and test this fundamental hypothesis.

Technical Approach

Nano-particles were arranged in "fuel clusters". A theoretical analysis based on chemical kinetics and heat balance indicated that clusters arranged into thin pellets would provide the optimal combustion properties. Each disk shaped cluster included a large number of nano-particles that could be appropriate for the elementary heat output in a combustion chamber. Proof-of-concept experiments were performed to establish the following: (1) A fuel cluster consisting of certain number of metallic nano-particles manufactured with determined configuration and adequate mechanical strength sufficient to sustain transport and storage. (2) A fuel cluster can be ignited in air under a given temperature and pressure with the help of a laser, electrical or electro-magnetic short-time pulse, or self-ignition. (3) The metal nano-particles composing a cluster are oxidized by atmospheric oxygen on a relatively short timescale with the maximum combustion temperature no higher than 1500^0 C and without forming volatile components. (4) After a fuel cluster is burnt, it preserves its configuration and continues to strongly bind to the carrier. (5) The combusted nano-fuel cluster can be reduced back to its original metallic form by using the reducing it with hydrogen.[3]

An experimental apparatus for examining the peak combustion temperature of the engineered cluster of metallic iron nano-particles was designed. Following combustion of the metal cluster, the cluster can be removed and examined via microscopy or x-ray diffraction to determine if the combustion produced significant amounts of volatile products instead of occurring mainly in the solid/condensed phase. The approximate fuel cluster size and shape to achieve the necessary heat flow was determined from computation and a method for experimentally producing this thin disk-shaped pellet composed of iron nano-particles was designed. The experimental method employed was relatively simple, using commercial grade iron nanoparticles (a TEM of the iron nanoparticles is shown in Fig. 1) which were sintered on a glass substrate using magnetic forces. The designed iron clusters consisted of ~16 mg/pellet, giving a disk with ~ 1 mm height and 2 cm in diameter. The glass slide containing the iron cluster was mounted into an infrared temperature sensor based on heterodyne or radiometric measurements to determine the combustion temperature. The infrared temperature sensor was constructed to specifically monitor time dependent temperature changes on a sample. The focusing optics was aligned through the 2 millimeter aperture that was replaced with a sample for performing measurements. The high speed response of the Mercury-Cadmium-Telluride (MCT) detector and the integration nature of heterodyne detection allowed measurements to be performed at speeds up to one millisecond.
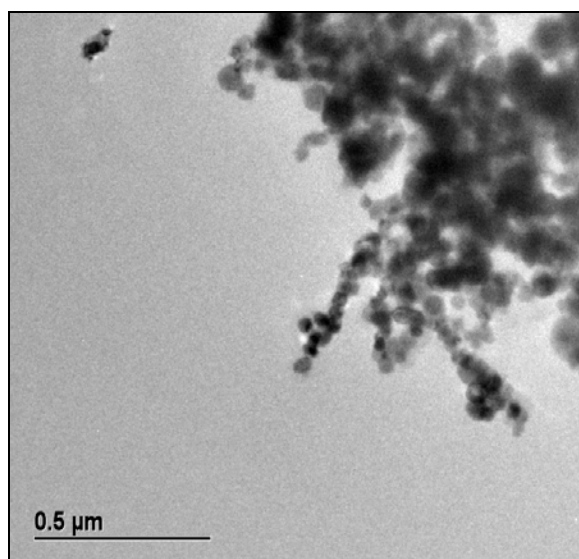
Figure 1. Iron nanoparticles TEM: diameter ~ 50nm

Results and Discussion

Multiple samples were tested, and in all cases, combustion proceeded rapidly (~0.5 sec), generating peak temperatures between 1000 and 1200 K, without the observable production of volatile products. Radiometry measurements are shown in Fig. 2 and clearly demonstrate combustion of the iron cluster occurs rapidly (~500 milli-seconds) with a peak temperature in near 1000K. The combustion process did not produce any visually notable volatile products or ash. The reproducibility of the process is very good and since the temperature is well below that required to form NO_x, it is reasonable to assume there is virtually none formed from the combustion process. Visual observations of the combustion process were quite dramatic as one can clearly follow the wave front of combustion through the cluster by noting the change in color which goes from black to red. Additional and more substantial evidence for solid-state combustion was obtained from x-ray diffraction of the iron cluster before and after combustion (Fig. 3) combined with gravimetric analysis. These results clearly show that the combustion process oxidizes ~94% of the iron into primarily hematite (Fe_2O_3) and maghemite, only leaving ~6% of the iron in its original state.
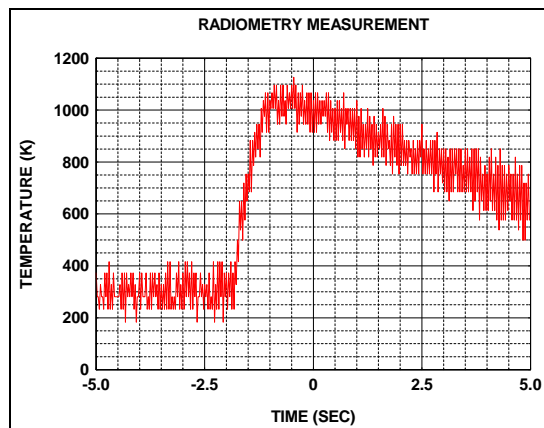
Figure 2. Radiometry measurements (**not** heterodyne) - Rough error estimate is +/- 100K
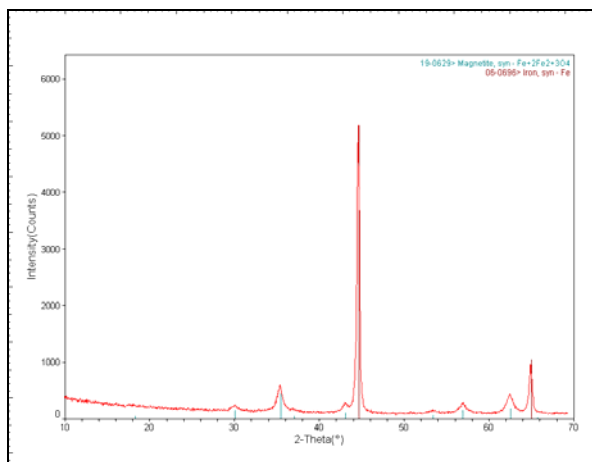
Figure 3a. X-ray diffraction results for the iron cluster before combustion with the peak for magnetite marked with stick spectra.
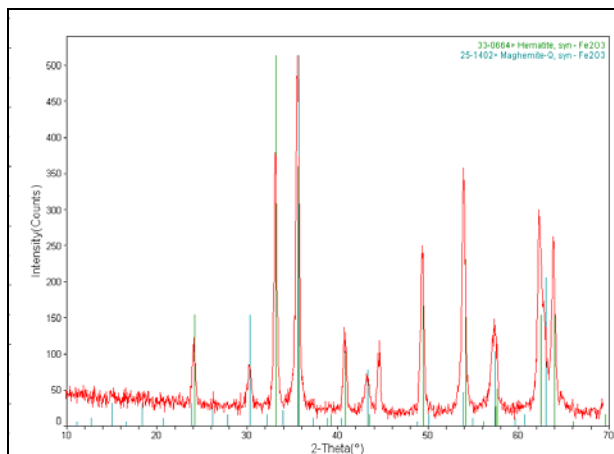
Figure 3b. X-ray diffraction results for the iron cluster after combustion with the peaks for magnetite and maghemite marked with a stick spectra.

References

[1] Glassman, I. Combustion , Academic Press: San Diago, 1996.
[2] Li, X.G; Chiba, A.; Takahashi, S.; Sato, M *J. Appl. Phys.* **1998,** 83(7), 3871.
[3] Mattisson, T.; Lyngfelt, A.; Cho, P. *Fuel* **2001,** 80, 1953.

DIMETHYL ETHER OXIDATION AT ELEVATED TEMPERATURES

Claudette M. Rosado-Reyes, and Joseph S. Francisco

Department of Chemistry and
Department of Earth and Atmospheric Sciences
Purdue University
West Lafayette, IN 47907

Joseph J. Szente, M. Matti Maricq, and Lars Froesig Oestergaard

Research Laboratory
Ford Motor Company, P.O. Box 2053, Drop 3083
Dearborn, MI 48121

Introduction

The fact that current diesel engine emissions will not meet future standards, has spurred research into alternative fuels in order to reduce emissions without compromising fuel economy. Oxygenated hydrocarbons such as ethers have been proposed for use as alternative fuels or as additives in diesel engines[1]. The chemical and thermodynamic properties of dimethyl ether (DME) make it ideal for this purpose: higher cetane number of 55-60[2], lower self ignition temperatures, NO_x emissions and engine noise[3], and no soot formation. The determination of alternative fuels emissions under operating conditions (high pressure and temperature) is required to assess the impact of these materials on the atmospheric reactivity of tailpipe emissions[4].

The use of DME as a fuel for solid oxide fuel cells (SOFCs) has also been under consideration[5]. There are potential applications for its use in vehicle based fuel cells. Direct oxidation of hydrocarbons eliminates the need for fuel reformers and can reduce the cost and weight of SOFC systems. The temperature dependence of DME thermal decomposition is important in determining the power output of SOFCs and their contamination by coking.

Under laboratory conditions, chlorine atoms - produced by the photolysis of Cl_2 - initiate the chemistry. Methoxymethyl radicals (CH_3OCH_2) are produced as a result of the abstraction of a methyl hydrogen from DME. Under high O_2 concentrations, methoxymethyl radicals combine with oxygen to produce methoxymethyl peroxy radicals ($CH_3OCH_2O_2$). Previous product studies of chlorine initiated chemistry at low temperature showed a dependence on total pressure, where production of formaldehyde and methyl formate compete against each other[6]. This pressure dependence was explained by proposing and showing that the oxidation of dimethyl ether proceeds via two different competitive pathways: a pressure dependent and a pressure independent pathway.

In the pressure dependent pathway, the energetically excited peroxy (RO_2^*) is collisionally deactivated into a stabilized peroxy radical that can continue reacting by usual peroxy radical reactions. From these methoxymethyl peroxy radical reactions, methyl formate ($CH_3OC(O)H$) is formed as a main by-product. Also a significant yield of formic acid ($HC(O)OH$) has been previously reported[7], although it is not clear how the proposed mechanism can account for it. The pressure independent pathway takes place via the intramolecular rearrangement of peroxy radical followed by dissociation into two molecules of formaldehyde and one molecule of hydroxyl radicals (2 $HC(O)H$ + OH). This pressure independent pathway is of particular interest with respect to combustion because OH radicals are an important reactive intermediate in combustion processes. The production of hydroxyl radicals can initiate and sustain a chain reaction between DME and OH. The original study of the dimethyl ether photoinitiated chemistry intended to determine the branching ratio of $CH_3OCH_2 + O_2$ reaction with respect to pressure[6]. Time-resolved UV/IR spectroscopy was utilized to perform real time kinetic measurements of this reaction at temperatures between 230 and 350 K, pressures between 10 and 200 Torr, and a time regime of up to 60 microseconds. At room temperature, the peroxy radical stabilization becomes more significant as pressure increases, but the dissociation pathway becomes insignificant to sustain combustion chain reactions. As the temperature increases the reaction shifts to the formaldehyde production, but this change is not as significant as the one dependent on pressure. The investigation of the kinetics of the photo-initiated $CH_3OCH_2 + O_2$ chemistry at elevated temperatures above 295 K revealed thermally induced reactions taking place independent of photolysis. Also these results raised the possibility that at even higher temperatures >350K, the dissociation channel might become significant enough to sustain DME + OH chain reaction, and be even more significant near or at combustion temperatures. This study intends to determine the branching for the $CH_3OCH_2 + O_2$ reaction pathways at pressures of 20-200 Torr and temperatures of 295-700 K, and the importance of dimethyl ether degradation in the presence of O_2 over the temperature range of 295-700 K.

Experimental

To investigate the temperature dependence on the degradation of dimethyl ether and consequently on the $CH_3OCH_2 + O_2$ branching ratio, the kinetics of the reaction of $CH_3OCH_3 + Cl_2$ in the presence of O_2 is being studied at elevated temperatures. Flash Photolysis/Transient Infrared Spectroscopy is used to evaluate the yield and kinetics of Formaldehyde, Methyl Formate, and Formic Acid, at the 1709 cm^{-1}, 1742 cm^{-1}, 1791 cm^{-1} vibrational lines respectively. The measurements include the direct probing of product concentration for the first 900 μsec after Cl_2 photolysis, and in the absence of Cl under steady state, at three different dimethyl ether concentrations (6, 12, 20 × 10^{16} molecules/cm^3). These experiments were carried out at three different total pressures (60, 250, 600 × 10^{16} molecules/cm^3) and eight different temperatures between 295 and 700 K (increments of 50K).

The Flash Photolysis/Time-Resolved IR Spectroscopy experimental apparatus is described as follows. A reagent gas mixture is inserted into a quartz cylindrical reaction cell. The gas mixtures for these experiments consisted of dimethyl ether (1-7 Torr), 4.8% chlorine/N_2 (2-11 Torr), O_2 (11-38 Torr), and N_2 to make up the balance. The reaction cell is wrapped with electrical heaters and insulated for thermal stability. Temperature is monitored and controlled by thermocouples positioned along the outside of the cell. The gases are pre-heated prior to entering the cell. Photo-dissociation of Cl_2 is initiated by 351 nm light from a Lambda Physik model LPX 301 excimer laser. Two dichroic beam-steering mirrors, placed at opposite ends of the reaction cell, reflect the UV laser light into the reaction cell while allowing the transmission of IR light. Conditions were such that the reaction cell was well evacuated and the gas mixture replenished between laser pulses. A high-resolution, cryogenically cooled, Pb-salt diode laser is used as the infrared light source to probe the ro-vibrational carbonyl stretch mode of by-products at frequencies between 1700 and 1800 cm^{-1}. After passing though a mode selecting monochromator, it is directed through the reaction cell where it counterpropagates relative to the excimer laser. The IR light is focused to a LN_2 cooled HgCdTe detector with a response time of 0.3 μsec. Frequency drift is prevented by frequency locking the laser radiation to the ro-vibrational absorption line being monitored. The IR light intensity is measured for several milliseconds following the laser photolysis pulse to obtain time

dependent absorbances. In order to quantify the concentrations of the by-products, their IR absorption cross sections (σ) at the respective IR absorbance lines are determined by introducing a known amount of by-product into the reaction cell of pathlength l. The concentration is then calculated by Beer's Law via,

$$c(t) = \left(\frac{1}{l\sigma}\right) \ln\left(\frac{I_0}{I}\right)$$

The initial halogen radical concentration from photolysis is calculated indirectly by substituting methanol for DME and measuring the formaldehyde yield from the photoinitiated oxidation reaction.

Results and Discussion

For the thermally induced chemistry measurements, the gas mixture of DME/O$_2$/N$_2$ was allowed to equilibrate to the selected temperature while flowing through the cell. Residence time in the cell was between 2 and 4 seconds. Figure 1 shows the formaldehyde yield, in the absence of chlorine, relative to dimethyl ether initial concentrations at temperatures between 295K and 700K. At temperatures between 450K and 500K, dimethyl ether thermally-induced oxidation is starting to take place. Above these temperatures, main by-products are being produced reaching maximum concentrations between 600K and 650K, starting then to decline. At low pressure conditions, formaldehyde yield is lower compared to medium and high pressure conditions. The change in formaldehyde yield is not significant going from 250×10^{16}/cm^3 to 650×10^{16}/cm^3 total pressure. Methyl formate and formic acid yields follow a similar trend, although formaldehyde yield is greater by a factor of 2 and 10 respectively. Figure 1 clearly shows a total pressure dependency as a function of temperature in the methoxymethyl peroxy radical chemistry, but also shows that the formaldehyde yield is independent of DME initial concentration.
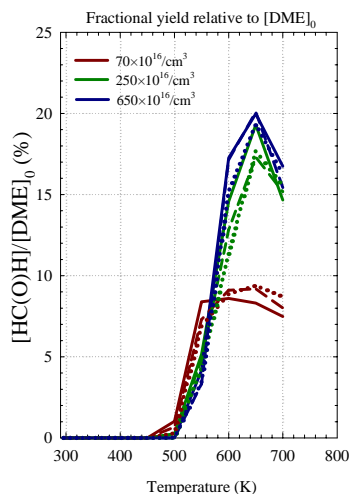

Figure 1. Formaldehyde yield relative to dimethyl ether initial concentration in the temperature regime of 295-700K at three different total pressure conditions.

Figures 2 and 3 show the pressure dependent yields of the three main by-products from photo-initiated DME oxidation experiments at 295K and 500K respectively. Due to the high initial radical concentrations, $> 10^{14}$/cm^3, for these measurements, the products are monitored for only a few milliseconds after the chemistry is initiated by chlorine atoms. At a given temperature, the formation of

formaldehyde shows pressure dependence due to the change in the fraction of peroxy radicals that undergo dissociation. In contrast, methyl formate yield remains essentially the same over this pressure range. No detectable levels of formic acid are measured during the first millisecond of the reaction.
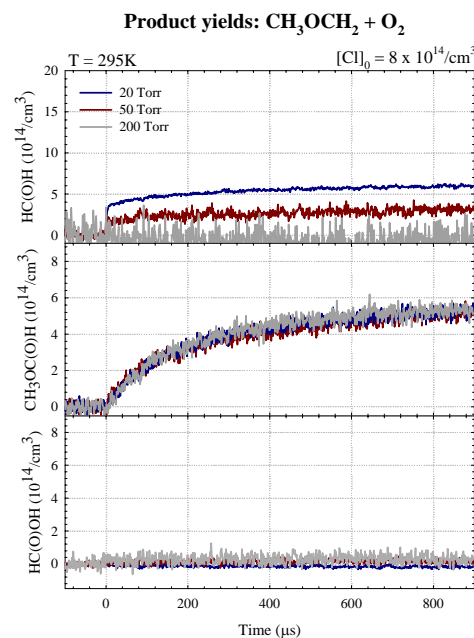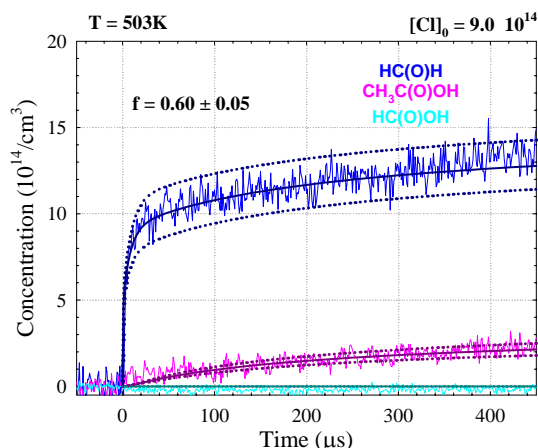

Figure 2. Formaldehyde, methyl formate, and formic acid concentration vs time profile from Cl$_2$-initiated DME degradation at room temperature as a function of pressure.
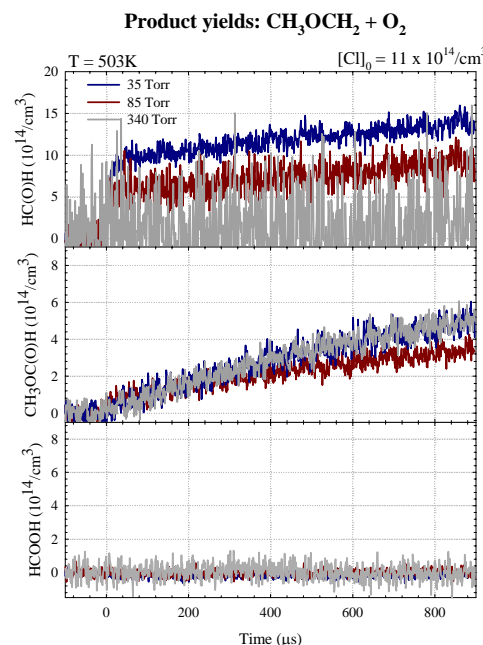
Figure 3. Formaldehyde, methyl formate, and formic acid concentration vs time profile from Cl$_2$-initiated DME degradation at 503K as a function of pressure.

As the temperature is raised from 295K to 503K, the formaldehyde yield increases, by as much as a factor of 3, with the greatest increase occurring at low pressures, and becoming less at the higher pressure. As total pressure is increased, IR detection of the products becomes increasingly difficult due to both the smaller product concentrations and the pressure broadening effect on absorbance cross section. While the methyl formate yield reaches similar levels at both temperatures, the rate of formation is slower as temperature increases.

A reaction mechanism for the oxidation of DME is being used to predict the temperature and pressure dependence of the methoxymethyl peroxy stabilization vs. dissociation branching ratio as well as the peroxy radical self reaction rate constant.

Figure 4. Formaldehyde, methyl formate, and formic acid yields predicted from kinetics model at 503K and 60×10^{16} molecules/cm^3.

A kinetics model based on the proposed reaction mechanism for the oxidation of DME is created to describe the chemistry taking place inside the reaction cell. The model consists of 35 different chemical reactions. For each species participating in the reaction mechanism, its differential equation for the production rate is solved for each individual set of experimental conditions. Figure 4 shows the prediction of formaldehyde, methyl formate and formic acid yields from the kinetics model at a temperature of 503K and low pressure conditions. The solid line represents the predicted yield, which is graphed over the data. The dashed line represents the predicted product yield over a change of $\pm 8\%$ on the calculated branching ratio. The large shift on the theoretical yields over a small change on the calculated branching ratio shows that the proposed reaction mechanism was able to accurately describe the DME oxidation under our experimental conditions.

The methoxymethyl peroxy radical chemistry will be further described by Lindemann and Arrhenius analysis of these parameters.

References
1. Leppard, W. R.; *SAE Trans*., **1991**, 912313.
2. Kapus, P. E.; Cartellieri, W. P.; *SAE Trans*., 1995, 952754.
3. Roubi, M. A,; *Chem. Eng. News*, **1995**, 44, 37.
4. Japar, S. M.; Wallington, T.J.; Richert, J. F. O.; Ball, J. C.; *Int. J. Chem. Kinet*., 1990, 22, 1257.
5. Murray, E. P.; Harris, S. J.; Jen, H; *J. Electrochem. Soc.*, **2002**, 149, A1127.
6. Maricq, M. M.; Szente, J. J.; Hybl, J. D.; *J. Phys. Chem. A.* **1997**, 101, 5155.
7. Liu, I.; Cant, N. W.; Bromly, J. H.; Barnes, F. J.; Nelson, P. F.; Haynes, B. S.; Chemosphere, **2001**, 42, 583.

NEW ADSORBENTS FOR DESULFURIZATION OF TRANSPORTATION FUELS

Gokhan O. Alptekin, Margarita Dubovik, and John Monroe

TDA Research, Inc.
12345 W. 52nd Avenue
Wheat Ridge, CO 80033

Introduction

To reduce the emissions of the environmental pollutants, U.S. Environmental Protection Agency announced new regulations that mandate refineries to reduce sulfur levels of the transportation fuels down to 30 ppmw in gasoline and 15 ppmw in diesel by 2006[1,2]. Refineries in the U.S. and worldwide are facing new challenges to produce very low sulfur highway and non-road fuels, while the crude oils refined in the U.S. are getting higher in sulfur content and getting heavier. In the future, the requirements for deep desulfurization of transportation fuels will become even more stringent because of the possibility that these fuels can be used on-board or on-site to support the operation of fuel cells for mobile, portable and transportation applications. Both high and low temperature fuel cells require clean feed streams with very low levels of sulfur[3,4]. To use gasoline or diesel fuels, which are ideal for fuel cells because of their high energy density, ready availability, safety and ease of storage, the sulfur concentration preferably should be below 0.2 ppmw[5].

Conventionally, the deep desulfurization can be achieved by a multi-step process including, hydrodesulfurization (HDS) over $CoMo/Al_2O_3$ and $NiMo/Al_2O_3$ catalysts and subsequent removal of H_2S with a sorbent. However, the HDS process is not suited well to produce ultra clean (essentially sulfur free) transportation fuels, particularly for fuel cell applications. At the severe reaction conditions required for effective sulfur removal, the olefins and aromatics in the gasoline are saturated leading to a decrease in the octane number. In addition, the current HDS process cannot adequately remove the refractory sulfur compounds present in the diesel and jet fuels. It has been shown that the HDS reactor size needs to be increased by a factor of 7, in order to be able to reduce the sulfur content of the diesel from 500 to 15 ppmw[6]. Clearly, more effective and affordable methods are needed to reduce the sulfur content of the transportation fuels to ultra low levels.

Previously, a new sorbent material was developed by TDA Research, Inc. for natural gas and liquefied petroleum gas (LPG) desulfurization, where the sorbent effectively removed sulfur-bearing odorants (e.g., thiophenes, mercaptans) with very high capacity[7]. The regeneration potential of the sorbent applying a mild temperature swing (by heating up the sorbent bed to 250-300°C) through several consecutive adsorption/regeneration cycles were also demonstrated[8]. Molecular theory and preliminary findings suggest that the same family of sorbents also have the potential to remove refractory sulfur species from higher hydrocarbon fuels. The challenge is to develop effective sorbents that are selective to the sulfur compounds. This paper summarizes the initial testing results of these new sorbent materials for deep desulfurization of transportation fuels.

Experimental

Sorbent Synthesis. Synthesis method of the sorbent was described in detail in prior literature[8]. As part of this work, several formulations were screened according to their physical properties, including porosity, surface area, crush strength of the pellet and active material content. In the selection of proper active material and support, the material costs were taken into consideration. The choice of substrate materials included conventional supports, which are low-cost and have high surface area (150 to 580 m^2/g measured by the manufacturers). The best formulations with the desired physical properties were tested for their sulfur removal performance under simulated conditions.

Test Setup. Preliminary tests for desulfurization of the fuels were performed in a batch reactor. As reported in a similar study[9], for these experiments a fixed fuel:adsorbent ratio was used to quickly screen various sorbent candidates at a baseline conditions. In a typical test, about 2 g of sorbent was mixed with 60 ml of a model or actual fuel containing about 2,000 ppmw of sulfur compounds in a round bottom flask (corresponding to a fuel:adsorbent ratio of 12.0). After mixing, the fuel and sorbent was continuously stirred while 50 μl liquid samples were taken out every hour for 4-6 hrs. A heating mantle and a water reflux combination provided the capability of running experiments at elevated temperatures as high as 80°C. These static experiments were used for quick screening to identify potential candidates to be tested in a flow system where the adsorbent will be tested in a tubular reactor setup.

Analytical System. The analysis of the sulfur compounds were carried out using a gas chromatogram equipped with a Flame Photoionization Detector (FPD) with 0.1 ppmv sulfur detection limit. A 30 m Restek XTI-1 column (30m x 0.25mm x 0.25μm) was used for the separation of sulfur compounds. After the tests, selected sorbent samples were sent to analysis in a local laboratory for chemical analysis using Inductively Coupled Plasma Atomic Absorption to confirm to sulfur uptake of the sorbents.

Results and Discussion

The composition of the transportation fuels vary widely depending on the crude oils used in the refining process, the product demand and specifications. Branched and n-alkanes are the main ingredients of these fuels accounting more that 70%. The major normal alkanes and the main branched alkanes are C5 to C8 compounds. The aromatics content constitutes about 30% of the fuel, mainly benzene, toluene, xylenes and alky benzenes. Thiophene, benzothiophene dibenzothiophene and their alkylated derivatives are the major sulfur compounds remaining in the fuel after HDS.

In the preliminary screening tests, we used n-heptane and benzene as model fuels to measure the efficacy of the sorbents in removing sulfur. **Figure 1** shows the gas chromatograms of the liquid samples extracted from the batch reactor at different time intervals.
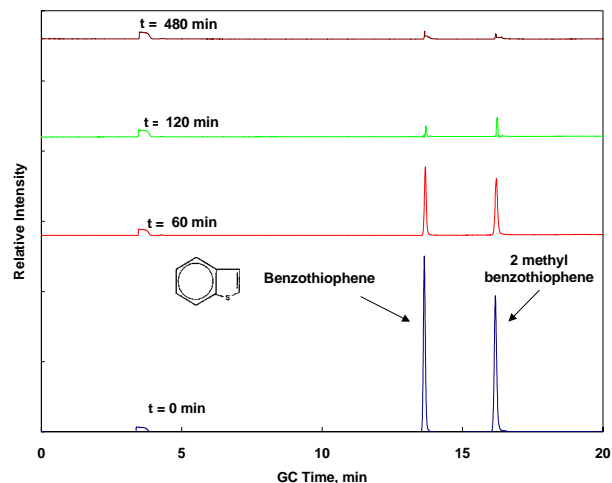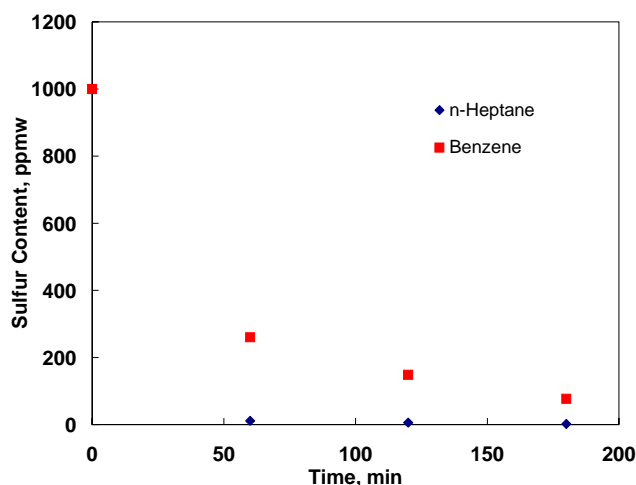

Figure 1. GC-FPD chromatograms for a model fuel sulfur analysis during a static experiment. 1,000 ppmw benzothiophene and 1,000 ppmw of 2-methyl benzothiophene in n-heptane. T=60°C.

In this experiment, n-heptane fuel containing 1,000 ppmw of benzothiophene and 1,000 ppmw of 2-methyl benzothiophene were mixed with a sorbent sample and the sulfur uptake capacity of the sorbent was measured as a function of time. The temperature of the reactor was maintained at 60°C throughout the test. As indicated by **Figure 1**, the sorbent could remove potentially all the sulfur in 6 hrs and more than 98% of the original amount in less than 2 hrs.
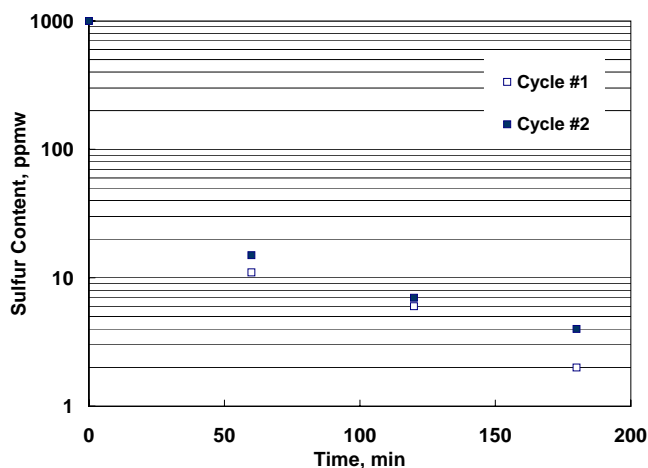
Once a promising candidate was identified, more tests were performed to evaluate its effectiveness in different fuel environments. **Figure 2** shows the change in the 2-methyl benzothiophene concentration in the batch reactor as a function of time. The removal rate and the overall sulfur uptake capacity of the sorbent were reduced by the presence when benzene was used as the model fuel. Although reduced, in the presence of benzene the sulfur adsorption capacity of the sorbent exceeds 0.85% on weight basis (based on 3 hr adsorption), where the adsorption capacity is defined as lb of sulfur removed per lb of sorbent.

Figure 3. The sulfur removal performance of the fresh sorbent and the sorbent regenerated at 300°C in N₂ flow. 1,000 ppmw benzothiophene and 1,000 ppmw of 2-methyl benzothiophene in n-heptane. T=60°C.

References
1. Ma, X., Sun, L., Song, C., *Catalysis Today*, **2002**, 77, 107.
2. Song, C., *Catalysis Today*, **2002**, 77, 17.
3. De Wild, P., R.G., Nyqvist and F. Bruijn, *Proc. of the Fuel Cell Seminar*, **2002**, 227.
4. Israelson, G., *J. of Materials Eng. And Performance*, **2004**, 282, 13, 3.
5. Yang, R.T., Hernandez-Maldonado, A., and Yang, F., H., *Science*, **2003**, 301, 79.
6. Hernandez-Maldonado, A., and Yang, R.T., *Ind. Eng. Chem. Res.*, **2003**, 42, 123.
7. Alptekin, G.O., DeVoss, S., Dubovik, M., and Monroe, J., 2004, *Proc. of the Fuel Cell Seminar*, **2004**, 864.
8. Alptekin, G.O., *J. of Power Resources*, **2004**, (in press).
9. Velu, S., Ma, X., and Song, C., *Ind. Eng. Chem. Res.*, **2003**, 42, 5293.

Figure 2. 2-methyl benzothiophene removal performance of the sorbent in different model fuels. 1,000 ppmw benzothiophene and 1,000 ppmw of 2-methyl benzothiophene in n-heptane and benzene. T=60°C.

The regeneration potential of the sorbent were also evaluated by applying a mild temperature swing. In these experiments, the sorbent was first exposed to n-heptane fuel containing 1,000 ppmw of benzothiophene and 1,000 ppmw of 2-methyl benzothiophene at 60°C. After the sorbent is saturated with sulfur, the solution was filtered to recover the sorbent. The tested sorbent was then heated to 300°C under 200 ml/min nitrogen flow overnight in a tube furnace. It was anticipated that this mild thermal treatment was sufficient to drive off the physically adsorbed sulfur species from the sorbent. The sorbent was then cooled to room temperature in nitrogen flow and then placed into the batch reactor again to test its performance using an identical sulfur-laden fuel. The comparison of the sorbent performance for removing 2-methyl dibenzothiophene from n-heptane fuel in two adsorption cycles are presented in **Figure 3**. In both cycles, the sorbent also removed all the benzothiophene.

These results suggest that the sulfur can be driven off from the sorbent by a simple thermal process heating the sorbent to 300°C. It is also suggested that the regenerated sorbent may maintain a stable cyclic capacity.

SIMPLE APPROACH FOR DETERMINATION OF THE AUTOTHERMAL REFORMING EFFICIENCY

Bijan F. Hagh

ES Logic, LLC
4231 E. Regency Avenue
Orange, CA. 92867

Introduction

Efficient generation of hydrogen is an important enabling technology for commercialization of fuel cells for homes and cars of the future.

There are a number of fuel processing technologies for hydrogen generation from hydrocarbon fuels and oxygenates, but in actuality these technologies are points along a spectrum that spans combustion and partial oxidation (POX) through steam reforming (SR) (1). Autothermal reforming (ATR) combines partial oxidation (POX) and SR, in a single process. POX reaction is exothermic or produces heat, while SR reaction is endothermic and heat must be generated external to the reformer process.

The thermal efficiency of an ATR process is usually determined by multiplying the hydrogen yield by the ratio of hydrogen and fuel Lower Heating Values (LHV). However, this approach overestimates the efficiency since it neglects to account for the heat input to the reactor. In a previous study, the efficiency for autothermal reforming of a generalized fuel was determined to be dependent on fuel atomic analysis and fuel heat of formation by assuming maximum efficiency at the thermoneutral point (2). Other researchers have determined the efficiency of a steam reformer to be only dependent on fuel atomic analysis and steam-to-carbon ratio (S/C) by assuming a minimum S/C of 2 (3). In this study, the efficiency of the fuel processing, in the full range of combustion to steam reforming, is shown to be only dependent on fuel atomic analysis and oxygen-to-carbon ratio (O_2/C) without any assumptions. Based on this simple approach, the efficiency of autothermal reforming of methane, propane, isooctane, dodecane, and hexadecane is compared.

In this study, H_2 yield from fuel processing is determined based on energy and material balance coupled with chemical equilibrium requirements. The assumptions inherent in the ATR energy and material balance are as follows:

- Complete consumption of O_2 without formation of carbon soot, which is a reasonable assumption at a S/C level of 2 or above (4).
- The carbon in the fuel is reformed to CH_4, CO or CO_2 only. For reforming of methane, CO and CO_2 constitute the only carbon containing reforming products (5).
- SR, WGS and methanation (for non-methane fuels) reactions are assumed to be at equilibrium at ATR outlet temperature. This is again a reasonable assumption based on previous studies (6).
- Adiabatic reaction

Maximum Hydrogen Yield

ATR reaction stoichiometrics for a generalized fuel, $C_xH_YO_Z$, can be represented as:

$$C_xH_YO_Z + a\,O_2 + b\,H_2O = c\,CH_4 + d\,CO + e\,CO_2 + f\,H_2$$
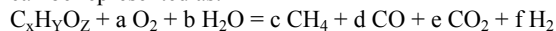
Where,

Table 1. Fuel Properties

Fuel - $C_XH_YO_Z$	X	Y	Z	Max Yield = (y/2)+2x-z	$°H_f$ (kJ/mole) @ 25°C	LHV (kJ/mole)
Hydrogen	0	2	0	1	0	229.16
Methanol	1	4	1	3	-178.96	663.40
Ethanol	2	6	1	6	-203.59	1,251.96
Methane	1	4	0	4	-56.89	785.47
Propane	3	8	0	10	-66.86	2,001.89
Isooctane	8	16	0	24	-174.33	4,731.24
Dodecane	12	26	0	37	-195.10	7,392.41
Hexadecane	16	34	0	49	-248.52	9,791.77

The reference point for all enthalpies is 0 degrees absolute.

$a = O_{2,\,Feed} / C_xH_YO_{Z,Reformed}$
$b = H_2O_{Reacted} / C_xH_YO_{Z,Reformed}$
$c = CH_{4,Reformate} / C_xH_YO_{Z,Reformed}$
$d = CO_{Reformate} / C_xH_YO_{Z,Reformed}$
$e = CO_{2,Reformate} / C_xH_YO_{Z,Reformed}$
$f = H_{2,Reformate} / C_xH_YO_{Z,Reformed}$

The above assumes that all O_2 is consumed in the ATR without formation of carbon soot. Based on atomic balance for O, C and H, it can be shown that:

$b = d+2e-z-2a$
$c = x-d-e$
$f = y/2+b-2c$

Combining all three Equations and rearranging:

$$f = (y/2+2x-z) -2a - (d+4c) \tag{1}$$

The above equation indicates that maximum theoretical hydrogen yield occurs when all the carbon in the fuel is reformed to CO_2 (i.e., no CH_4 or CO produced), which is consistent with previous literature [5]. For maximum hydrogen yield, Equation (1) reduces to:

$$f_{max} = (y/2+2x-z) - 2a \tag{2}$$

Table 1 summarizes the values of (y/2+2x-z), standard heat of formation and LHV for a number of fuels and Figure 1 shows the linear relationship between LHV and (y/2+2x-z). Defining Stoichiometric Ratio (SR) as the ratio of oxygen reacted to stoichiometric oxygen required for combustion, the maximum hydrogen yield for any fuel can be represented by the following Equation:

$$f_{max}/(y/2+2x-z) = 1 - SR \tag{3}$$
where, $SR = 2a/(y/2+2x-z)$
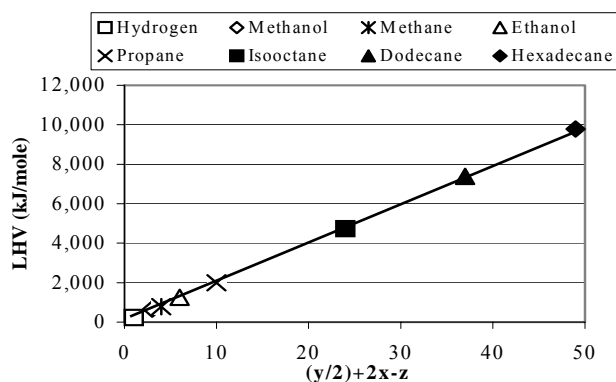
Figure 1. Maximum hydrogen yield for steam reforming of various fuels

**Thermal Efficiency**

The reformer thermal efficiency is commonly obtained by multiplying the hydrogen yield by the ratio of LHV of H2 to fuel. However, this standard definition may result in efficiencies greater than 100% as discussed elsewhere (3). In addition to the fuel that is reformed to hydrogen, extra fuel is necessary to supply the required heat for the reforming process. This extra fuel provides external heat to a steam reformer, whereas for an autothermal reformer, the extra fuel is consumed in the reactor to provide internal heat. A more accurate approach, proposed in this study, is to determine the fuel processor efficiency by dividing the hydrogen yield by fmax, which represents the maximum theoretical hydrogen yield at a given oxygen level.

To see how the proposed approach compares to the standard method of determining the fuel processor efficiency, let us express the ratio of hydrogen and fuel LHVs in terms of standard heats of formation of the respective combustion products:

$$\frac{LHV_{H2}}{LHV_{Fuel}} = \frac{-\Delta H^{\circ}_{f,H2O(g)}}{\Delta H^{\circ}_{f,Fuel} - x\Delta H^{\circ}_{f,CO2} - (y/2)\Delta H^{\circ}_{f,H2O(g)}} \quad (6)$$

Consider the autothermal reforming of a generalized fuel for maximum hydrogen yield (i.e., no CH4 or CO produced):

$$CxHYOZ + a\ O2 + b\ H2O\ (g) = e\ CO2 + f\ H2 \quad (7)$$
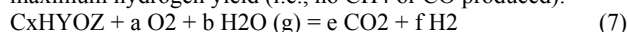
The water in Equation (7) is in form of steam in recognition of high temperatures necessary for fuel reforming. Based on atomic balances for O and C, it can be shown that:

b = 2x-z-2a
e = x

The standard heat of reaction for equation (7) is:

$\Delta H^{\circ}R = -\Delta H^{\circ}f$,Fuel $+ x *\Delta H^{\circ}f$,CO2 $- (2x-z-2a)* \Delta H^{\circ}f$, H2O(g) (8)

Substituting Equation (8) into Equation (6) and assuming that LHVfuel and $\Delta H^{\circ}R$ refer to the same state of fuel:

$$\frac{LHV_{H2}}{LHV_{Fuel}} = \frac{-\Delta H^{\circ}_{f,H2O(g)}}{-(y/2+2x-z-2a)\Delta H^{\circ}_{f,H2O(g)} - \Delta H^{\circ}_{R}} \quad (9)$$

If we divide the numerator and denominator with $-\Delta H^{\circ}f$, H2O(g) and rearrange:

$$\frac{LHV_{H2}}{LHV_{Fuel} + \Delta H^{\circ}_{R}} = \frac{1}{(y/2 + 2x - z)(1 - SR)} \quad (10)$$

The following expression for the thermal efficiency, η, can be obtained by substituting Equation (3) in (10):

$$\eta = \frac{HydrogenYield * LHV_{H2}}{LHV_{Fuel} + \Delta H^{\circ}_{R}} = \frac{f}{f_{max}} \quad (11)$$

where, $\Delta H^{\circ}R$ represents the heat necessary to produce maximum hydrogen from autothermal reforming of a given fuel. The efficiency can also be expressed in terms of HR by substituting Equation (3) into (11):

$$\eta = \frac{HR}{(1-SR)} \quad (12)$$

Figures 8, 9 and 10 show the efficiency, as defined by Equation (12), for hexadecane, dodecane, isooctane, propane and methane as a function of SR for various inlet temperatures at S/C=3 and S/C=2, assuming adiabatic conditions. Figure 11 shows that methane has the highest efficiency compared to other fuels, consistent with previous literature (2, 3), and the efficiency increases as the inlet temperature decreases. This is somewhat counterintuitive since higher inlet temperatures results in higher hydrogen yield. However, higher inlet temperatures lead to lower SR, which increases the denominator of Equation (12), hence resulting in lower efficiency.

Equation (12) does not explicitly show the effect of S/C and water consumption in the reforming process. Substituting Equation (1) into the numerator of Equation (11):

$$\eta = 1 - \frac{d + 4c}{f_{max}} \quad (13)$$

Let us consider the idealized autothermal reforming reaction, where CO and CH4 are not produced (i.e., η=1):

$$CxHYOZ + a\ O2 + b\ H2O = e\ CO2 + f\ H2 + g\ H2O \quad (14)$$

Using stoichiometric analysis, we can drive the following relationship between water and oxygen consumption:

$$b = \frac{x}{2} * (S/C + 2) - \frac{z}{2} - a \quad (15)$$

The above equation shows that for a given oxygen feed to the reactor (i.e., SR), water consumption, b, increases with S/C. This in turn reduces CO and CH4 formation in the autothermal reactor by the WGS and reverse methanation reactions, resulting in higher efficiency.

It is important to note the limitations of Equation (12) for determination of efficiency. The maximum standard heat of reaction for autothermal reforming is not necessarily represented by $\Delta H^{\circ}R$, as defined by Equation (8). Due to the exothermic nature of the WGS reaction, the maximum standard heat of reaction would occur when all carbon in the fuel is reformed to CO. The standard heat of reaction also does not include the total heat required for bringing the reactants to the temperature of the reaction. However, the implication of the first limitation is small and the second limitation is mitigated by the inclusion of the oxygen consumed in the autothermal reaction (i.e., SR) in Equation (12).

Conclusions

The stoichiometric analysis of the autothermal reaction for a generalized fuel is used to determine the reforming reaction space for methanol, ethanol, methane, propane, isooctane, dodecane, and hexadecane, in the full range of steam reforming to combustion. A simple approach is proposed for determination of the thermal efficiency for autothermal reforming based on fuel atomic analysis and oxygen consumption. The thermal efficiency appears to increase with S/C and to be inhibited by higher inlet temperatures. The simulation data and conclusions of this paper are applicable to any ATR regardless of size and are independent of feed flowrates.

References

[1] Hagh, B.F. *International Journal of Hydrogen Energy*, **2003**, 28, 1369-1377.
[2] Ahmed, S.; Krumpelt, M. International Journal of Hydrogen Energy, 2001, 26, 291-301.
[3] Lutz, AE, Bradshaw, RW, Keller, JO, Witmer, DE. International Journal of Hydrogen Energy, 2003, 28, 159-167.
[4] Douvartzides, S.L.; Coutelieris, F.A.; Demin, A.K.; Tsiakaras, P.E. *AIChE Journal*, **2003**, 49, 248-257.
[5] Ming, Q.; Healey, T.; Allen L., Irving, P. *Catalysis To*day, **2002**, 51-64.
[6] Brown, L.F. *International Journal of Hydrogen Energy*, **2001**, 26, 381-397.

Figure 3. Inlet temperature = 670°C, P = 5 psig (136 kPa)

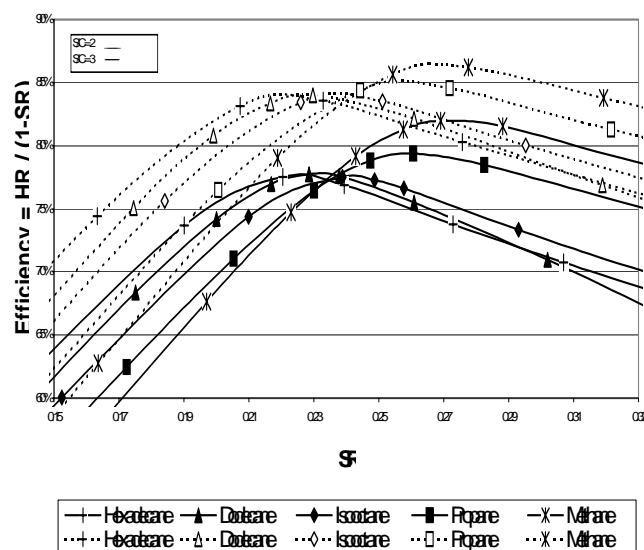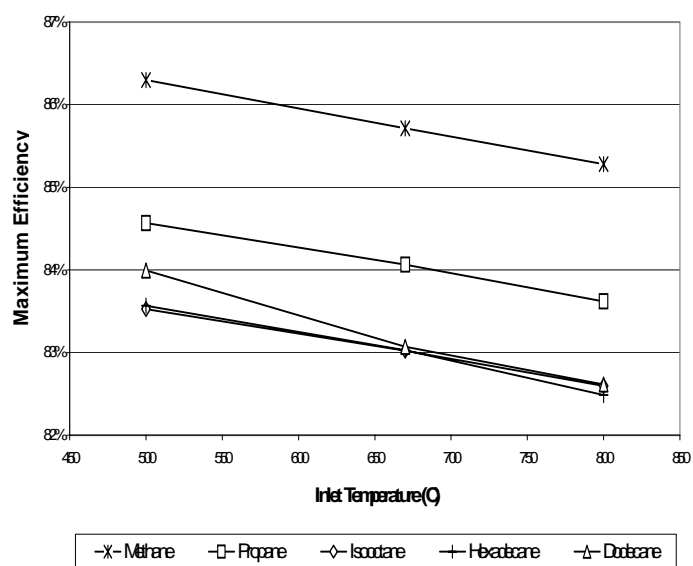**Figure 2.** Inlet temperature = 500°C, P = 5 psig (136 kPa)

Figure 4. Inlet temperature = 800°C, P = 5 psig (136 kPa)

Figure 5. Maximum efficiency at S/C = 3, P = 5 psig (136 kPa)

BIODESULFURIZATION OF DIBENZOTHIOPHENE BY A NEWLY ISOLATED BACTERIUM *Agrobacterium tumefaciens* UP-3

Hou Yingfei, Kong Ying, Yang Jinrong, Zhang Jianhui, Chen Rong

Biochemical Engineering Laboratory,
College of Chemistry and Chemical Engineering,
University of Petroleum,
Shandong, Dongying 257061, China

Introduction

The trend of the 21st century is environmental protection and continuable development. In order to decrease the influence of acid rain and air pollution caused by sulfur dioxide released from the combustion of fuel oils, more and more regulations on sulfur content in fuel oils are being implemented [1]. The current industrial method for removing sulfur from fuels is hydrodesulfurization (HDS). HDS is costly and energy-intensive for deep desulfurization, requiring high temperature and high pressure. Furthermore, HDS is not effective for removing heterocyclic sulfur compounds such as DBT and DBT derivatives. Biodesulfurization (BDS) is a process that removes sulfur from fossil fuels using a series of enzyme-catalyzed reactions [2]. It leads to the development of highly efficient reactions and environmentally friendly technologies. BDS, which operates under ambient temperature and pressure, is expected to be a complement and a promising alternative to HDS [3].

A lot of attempts have been made to develop BDS process. A few strains that can desulfurize DBT and DBT derivatives have been isolated, such as *Rhodococcus erythropolis* H-2 [4], *Paenibacillus sp.* A11-2 [5], *Mycobacterium phlei* GTIS10 [6], *Rhizobium meliloti* Orange 1 [7], *Gordona sp.* CYKS1 [8], and *Rhodococcus erythropolis* KA2-5-1 [9]. Two pathways for DBT metabolism are now recognized, namely, the ring-destructive pathway, represented by the Kodama pathway and the sulfur-specific pathway, the so-called 4S pathway. In this paper, the DBT metabolism of UP-3 (CGMCC No.0973), which was isolated from soil and sewage in the Shengli Oilfield, was identified as *Agrobacterium tumefaciens*. To improve stability and longevity of biocatalyst, BDS was carried out using immobilized *Agrobacterium tumefaciens* UP-3 in model system by using polyvinyl alcohol (PVA) and sodium alginate (SA) as supports.

Experimental

Chemicals. DBT (analytical grade), was purchased from Fluka Chemical Co. (France). The n-hexadecane was obtained from Haltermann Company (Germany). Sodium alginate was supplied by Shanghai Chemistry Reagent Plant. All other chemicals were of analytical grade, commercially available and used without further purification.

Microorganism. *Agrobacterium tumefaciens* UP-3 was isolated from the soil and sewage contaminated by sulfur-containing petroleum in the Shengli Oilfield. Strain UP-3 was grown aerobically in Seuton's medium (peptone 10g, yeast extract 2g, casein 2g, NaCl 6g, glucose 10g, distilled water 1000ml, pH7.5) at 30°C for 24h. Cells were then collected by centrifugation, washed with sodium phosphate buffer (pH 7.5). Strain UP-1 was washed by 0.9% (w/w) NaCl before immobilization.

Identification of strain UP-3. According to the reference [10], the species was identified by measuring traditional physiological and biochemical characteristics, and determining the DNA sequence of the 16S-rDNA gene. Then compare the homology with a library of known DNA sequence in GenBank+EMBL+PDB database project and make sure the genus.

Immobilization methods. The mixture of SA and PVA was selected as the carriers. The pH and temperature of immobilization were 7.3~7.5 and 4℃ respectively. The process of immobilization was as follows: support materials were dissolved in deionized water at 100°C. Then the support solution was cooled to room temperature, cell suspension was added to the solution and thoroughly mixed. This mixture was then dropped into 2% (w/w) $CaCl_2$ solution and boric acid saturation solution to form the immobilized cells beads with the diameter of 3-5 mm. The immobilized cells were washed three times with deionized water.

Experiment of BDS. BDS was carried out using immobilized cells (10g beads) or non-immobilized cells (1.0g wet cells) as biocatalyst in model system containing DBT (2.7mM) in a 250ml flask with shaking (200rpm) at 30°C. The amount of residual DBT was measured as described below. DBT in the reaction mixture was extracted with n-hexane after acidifying the samples to pH2.0. The hydrocarbon phase was separated from aqueous-phase containing cells by centrifugation at 10000rpm for 15min. The non-immobilized cells were washed thrice with sodium phosphate buffer and the immobilized cells were reactivation aerobically in 0.9% w/w NaCl solution. Each batch of immobilized cells was carried out for 100h, and that of non-immobilized cells was carried out for 20h. The concentration of DBT was analyzed by gas chromatography.

Results and Discussion

Identification of UP-3. The bacterial community of UP-3 is white, dope and surface velvet. The cell of UP-3 is bacilliform, gram-negative，no sporangium, moving with ambient flagellum. Fig.1 was the transmission electron micrograph of strain UP-3. UP-3 isn't antacid. Growth hormone and glutamic acid are its limiting factors.
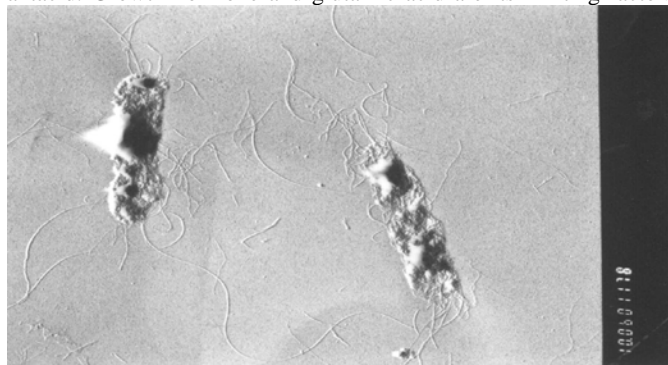

Figure 1. Transmission electron micrograph of strain UP-3.

The sequence length of UP-3 16S rDNA gene sequence was 1387bp. The registered number is AY364329, and the number of CGMCC is 0973. Table 1 shows the analytic results of homology by Blast software. UP-3 has high homological with some *Agrobacterium* sp. According to the classified principle in the ninth version of 《Bergey˙s Manual of determinative Bacterium》 and the physiologic and biochemical characteristic, UP-3 belongs to *Agrobacterium tumefaciens*. The *Agrobacterium tumefaciens* stain for BDS has not been reported previously.

Determination of DBT-desulfurizing performance. UP-3 could grow in Seuton's medium with DBT as the sole source of sulfur. The time curve of DBT concentration and cells concentration at 30°C by growing cells of UP-3 was determined as shown in Fig.2. The growth curve of UP-3 was determined by spectrophotometer. Inoculation time was defined as 0h. It was found that the concentration of DBT was reduced 87.5% within 50h, and the

concentration of cells began to decrease after 40h. It was confirmed that UP-3 has DBT-desulfurizing performance, and death phase of this strain began at 40h. However, the resting cells could not utilize DBT as the sole source of sulfur. The DBT was not degraded completely because of feedback inhibition of metabolites.

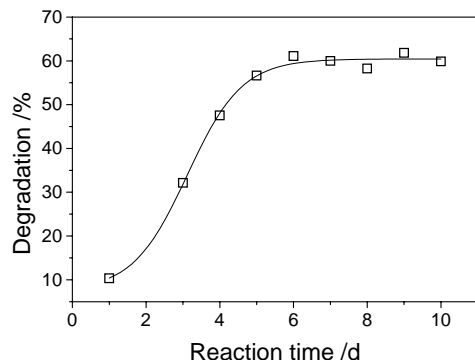On the other hand, experiment of utilizing carbon sources was also investigated. Here n-dodecane, n-hexadecane, paraffine liquid and naphthalin represent as n-paraffin, iso-paraffin and unsaturated aromatic respectively. The results indicated that UP-3 could not utilize the above hydrocarbon as the sole source of carbon. Therefore, UP-3 has good application prospect for petroleum desulfurization.

Table 1.   Blast analysis of UP-3 16S rDNA sequence

Sequences Producing Significant Alignments	Score（bits）	Similarity（%）
Agrobacterium albertimagni 16s ribosomal	2738	99%
Arsenite-oxidizing bacterium BEN-5 16s ribosomal	2694	99%
Agrobacterium tumefaciens partial 16s ribosomal	2615	99%
Agrobacterium sp.IrT-JG14-14 partial 1	2595	98%
Agrobacterium sp.IrT-JG14-33 partial 1	2585	98%
Agrobacterium tumefaciens 16s rRNA gene	2569	98%
ATU389903 Agrobacterium tumefaciens gene	2474	97%
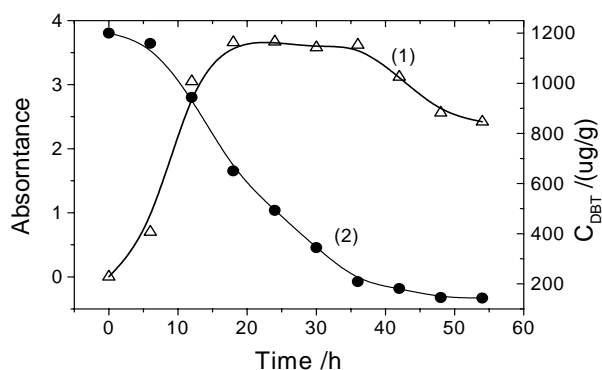
Figure 2. Time courses of DBT concentration and cell concentration (1) Growth curve; (2) Degradation curve

The performance of immobilized cells. In fact, the activity of most microorganisms will decrease after immobilization, so is UP-3. Figure 3 showed the curve of degradation of immobilized UP-3. The results showed that more than 65% DBT was degraded, and DBT degradation stopped after 5d. This may be related to the diffusion restriction of the support materials, and also related to feedback inhibition of products.

Figure 3.   Relationship of DBT degradation with degradation time

Conclusions

BDS is an environmental friendly technology. UP-3 (CGMCC No.0973) was isolated from soil and sewage contaminated by sulfur-containing petroleum in the Shengli Oilfield. The species was identified by measuring biochemical characteristics and the DNA sequence of the 16S-rDNA gene. The results indicate that UP-3 belongs to *Agrobacterium tumefaciens.* The *Agrobacterium tumefaciens* strain for BDS has not been reported previously. The pathway of DBT metabolism is neither Kodama pathway nor 4S pathway. That needs to be more research. It has ability to use DBT as the sole source of sulfur for growth at 30 ºC and without degrading n-dodecane, n-hexadecane, paraffine liquid and naphthalin. The total content of DBT was reduced 87.5% using growth cells of UP-3 within 50h. Its resting cells show no obvious desulfurizing capability. When the concentration of DBT was 500µg/g, more than 65% DBT was degraded by immobilized cells. In a word, UP-3 exhibits industrialized potential and good prospect for petroleum desulfurization.

References
1. Xu Cheng'en, Petroleum Refining Engineering, 2000, 30(3), 1-4.
2. Qian Bozhang, Wu Hong, Petroleum Refining Engineering, 1999, 29(8), 26-31.
3. Kilbane, Ⅱ, John J., US Patent 5,104,801.
4. Ohshiro T, Hirata T, Izumi Y., FEMS Microbiology Letter, 1996, 142, 65-70.
5. Kobayashi M,Onaka T, Ishii Y, FEMS Microbiology Letters, 2000,187, 123-26.
6. Kayser K.J., Cleveland H.S., Park J.H., Applied Microbiology and Biotechnology, 2002, 59, 737-45.
7. Frassinetti S., Setti L., Corti A., Canada Journal of Microbiology, 1998, 44, 289~97.
8. Chang J.H., Chang Y.K., Ryu H.W., FEMS Microbiol Letter, 2000, 182, 309-12.
9. Manabu Naito, Takuo Kawamoto, Kazuhito Fujino, Appl Microbiol Biotechnol, 2001, 55, 374-78.
10. Paabo S.，Wilson A. C., Nature, 1988, 334, 387-88.

PRODUCTION OF HYPERCOAL FROM LOW-RANK COALS
- EVALUATION OF NON-COVALENT BONDS -.

Nao Kashimura, Kensuke Masaki, Toshimasa Takanohashi, Shinya Sato, Akimitsu Matsumura, and Ikuo Saito

Energy Technology Research Institute,
National Institute of Advanced Industrial Science and
Technology 16-1 Onogawa, Tsukuba, Ibaraki 305-8569, Japan

Introduction

In power generation, the direct combustion of coal in a gas turbine increases power output, while reducing CO_2 emissions. However, most of the mineral matter (ash) in coal must be removed before it is injected into the gas turbines for this type of system to run successfully. Currently, the potential of thermal extraction using cost-effective industrial solvents is being assessed in Japan with a view to producing an ashless "HyperCoal" for direct gas turbine combustion.[1-8] In this process, the target value for extraction yield is > 60% with the HyperCoal having an ash content below 200 ppm. In previous work, extraction yields higher than 60% were obtained for several bituminous coals using a flowing solvent extractor with non-polar solvents, while, the extraction yields of subbituminous coal were generally lower than 60% with those solvents.[3-5]

Low-rank coals are known to have aggregated structures through non-covalent interactions among several functional groups such as hydroxyl, carboxyl and metal carboxylate groups. Li *et al* reported a polar solvent, *N*-methyl-2-pyrrolidinone, gave much higher extraction yields for subbituminous coals than a non-polar solvent, 1-methynaphthalene.[6] This is explained by that thermal-induced relaxation of the aggregate occurred in extraction in the latter solvent, while not only thermal-relaxation but also solvent-induced relaxation did in the former solvent. Thus, the solvent-induced relaxation can be effective for release of the non-covalent interactions, leading to the high extraction yields of the coals.

Liotta reported that *O*-methylated coal gave higher extraction yields with several solvents in a Soxhlet extractor than the raw coal, and the effect was attributed to release of hydrogen bonds by the *O*-methylation.[10]

In this work, an attempt was made to evaluate effect of release of several oxygen-containing functional groups on thermal extraction of subbituminous coals. Subbituminous coals were *O*-acetylated and *O*-methylated, and those treated coals were extracted at 360°C.

Experimental

Materials. Wyodak Anderson (WY) and Pasir (PA) subbituminous coals (< 150 μm) were used. All samples were dried under vacuum at 80°C for 12 h, and then were stored in a desiccator prior to use. Table 1 shows elemental and ash yield of the coals. Crude methylnaphthalene oil (CMNO) and light cycle oil (LCO) were employed as extraction solvents. They are industrial solvents and mainly consist of di-aromatics; LCO was a non-polar solvent, while CMNO was a polar one which contained quinoline and its derivatives.

O-acetylation. *O*-acetylation treatment was carried out according to the method by Blom *et al.*; 2.5 g of coal sample, 72 ml of pyridine and 36 ml of acetic anhydride were put into a flask and heated at 130°C for 12 h with refluxing.[11] After then, 500 ml of distilled water was added to the flask. The residual solid in the contents was separated from the aqueous solution by filtration, washed with distilled water, and dried at 80°C for 12 h in vacuo. Hereafter, the *O*-acetylated WY and PA are referred to as WY-Ac and PA-Ac, respectively.

O-methylation. *O*-methylation was conducted according to the method by Cody *et al*; 2.5 g of coal sample, 20 ml of tetrahydrofuran, 2.25 g of 40 wt% of aqueous KOH solution and 4 g of iodemethane were charged into a flask and stirred for 12 h at an ambient temperature.[12] Tetrahydrofuran, unreacted iodemethane and water were removed from the residual solid by evaporation. HCl aqueous solution (1 N) was added to the solid until pH of the solution was 2.5 and filtrated. The solid was washed with distilled water and dried at 80°C for 12 h in vacuo. Hereafter, the *O*-methylated WY and PA are referred to as WY-Me and PA-Me, respectively.

Thermal Extraction. A flowing solvent extractor was employed as an apparatus for extraction. Details of extraction procedure were described elsewhere.[3-7] Approximately 0.25 g of coal sample was charged into a stainless steel cell fitted with stainless steel filters (0.5 μm). Thermal extraction preceded by supplying fresh solvent at a flow rate of 0.1 mL / min under a nitrogen atmosphere of 1.0 MPa and at extraction temperatures of 360°C. The residual solid left in the cell was recovered, washed with toluene and acetone and dried at 80°C for 12 h in vacuo. Extraction yield of coal was calculated using the following equation,

$$\text{Extraction yield} = (1 - m_r/m_c)/(1 - A_c/100) \times 100$$

where A_c is ash content of the initial coal and m_r and m_c are masses of residue and initial coal, respectively.

Results and Discussion

Effect of *O*-acetylation on Extraction Yield. Figure 1 shows extraction yields of WY-Ac and PA-Ac. The extraction yields of WY-Ac in both solvents were higher than those of WY. While, the extraction yield of PA-Ac in LCO was equivalent to that of PA, although in CMNO the effect of *O*-acetylation was seen. These results suggest that the effect of *O*-acetylation on the extraction yield depends on the coal type. In *O*-acetylation, hydrogens in phenolic hydroxyl groups were replaced by acetyl groups, resulting in release of hydrogen bonds between phenolic hydroxyl groups.[11] In addition to this, acetic acid can be formed through *O*-acetylation. Li *et al* reported that acid pretreatment for WY coal, increased the extraction yield, and the effect was attributed to release of ionic cross-links by removing ion-exchangeable metals.[6] Therefore, it is expected that not only hydrogen bonds between phenolic hydroxyl groups but also ionic cross-links would be released by *O*-acetylation. Ash removal by *O*-acetylation is defined as

$$\text{Ash removal [wt\%]} = (1 - m_c \times A_c/m_a/A_a) \times 100$$

where m_c and m_a are masses of initial and *O*-acetylated coals, and A_c and A_a are ash contents of initial and *O*-acetylated coals, respectively. Ash removals of WY-Ac and PA-Ac were 49 and 6%. This result suggests that for WY coal not only hydrogen bonds but also ionic cross-links were released by *O*-acetylation, while for PA coal, the release of ionic cross-links was not significant. Thus, the difference in extraction yields between WY and WY-Ac can be explained by releases of ionic cross-links as well as hydrogen bonds.

Acid-treated WY (WY-A) was prepared using a 1 mol/L of methoxylethoxyacetic acid (MEAA) aqueous solution. WY-A was further subjected to *O*-acetylation. The *O*-acetylated WY-A is referred to as WY-A-Ac. Figure 2 shows the extraction yields of WY-A and WY-A-Ac. In the case of LCO, the extraction yield of WY-A-Ac was higher than that of WY-A, while, in CMNO the extraction yields were almost similar. Ash removals of WY-A and WY-A-Ac were 55 and 51%, respectively, showing that removal of mineral matter hardly progressed during *O*-acetylation of WY-A. Thus, the difference in extraction yields between WY-A and WY can be explained by effect of release of hydrogen bonds between phenolic hydroxyl groups. As shown in Fig. 2, the effect was observed only for non-polar solvent, LCO. There can be a plausible

explanation for the results; the polar solvent CMNO releases hydrogen bonds between hydroxyl groups, while the non-polar solvent LCO hardly releases them.

Effect of *O*-methylation on Extraction Yield. Figure 3 shows that the extraction yields of *O*-methylated coals in both solvents were higher than those of raw coals. Liotta *et al* reported that both of carboxyl and phenolic hydroxyl groups were *O*-methylated.P[10] In addition, ash removals of WY-Me and PA-Me were 63 and 20%, respectively, indicating the ionic cross-links were also released during *O*-methylation as well as *O*-acetylation above. Thus, hydrogen bonds through carboxyl and phenolic hydroxyl groups, and ionic cross-links were released during *O*-methylation.

Effect of Release of Non-Covalent Bonds on Extraction Yield. As described above, acid treatment releases ionic cross-links, acid treatment/*O*-acetylation does ionic cross-links and hydrogen bonds between phenolic hydroxyl groups, and *O*-methylation does ionic cross-links and hydrogen bonds between carboxyl groups as well as phenolic hydroxyl groups. Thus, effects of release of such non-covalent bonds on the extraction yields were evaluated by differences in the extraction yields between raw coal and acid-treated coal, acid-treated and acid-treated/*O*-acetylated coals, and acid-treated/*O*-acetylated and *O*-methylated coal, respectively, as summarized in Fig. 4. The extraction yield of WY with LCO was increased by the release of every non-covalent bond, while, that with CMNO was greatly increased by the release of ionic cross-links and hydrogen bonds between carboxyl groups. In contrast, the extraction yields of PA with both solvents hardly depended on the release of either ionic cross-links, or hydrogen bonds between phenolic hydroxyl groups, however, was highly enhanced by the release of hydrogen bonds between carboxyl groups.

Conclusion

1. For two subbituminous coals, extraction yields higher than 60% were obtained by release of hydrogen bonds and ionic cross-links by means of *O*-methylation before extraction.

2. A polar solvent releases weaker non-covalent bonds such as hydrogen bonds between phenolic hydroxyl groups. While, strong bonds such as hydrogen bonds between carboxyl groups and ionic cross-links were hardly released by not only a non-polar solvent, LCO but also a polar solvent, CMNO.

References
(1) Okuyama, N.; Deguchi, T.; Shigehisa, T.; Shimasaki, S. *Proceedings of 17th Annual International Pittsburgh Coal Conference* **2000**.
(2) Okuyama, N.; Deguchi, T.; Shigehisa, T.; Shinozaki, S. *International Conference on Clean Coal Technologies for Our Future* Sardinia, Italy, **2002**.
(3) Yoshida, T.; Takanohashi, T.; Sakanishi, K.; Saito, I.; Fujita, M.; Mashimo, K. *Energy Fuels*, **2002**, *16*, 1006.
(4) Yoshida, T.; Li, C.; Matsumuya, A.; Sato, S.; Saito, I. *Proceedings of 9th APCChE Congress and CHEMICA*, **2002**.
(5) Li, C.; Takanohashi, T.; Yoshida, T.; Saito, I.; Iino, M. *Proceedings of China International High-tech Symposium on Coal Chemical Industry and Conversion.* **2002**, 170.
(6) Li, C.; Takanohashi, T.; Yoshida, T.; Saito, I.; Aoki, H.; Mashimo, K. *Fuel* **2004**, *83*, 727.
(7) Masaki, K.; Takanohashi, T.; Yoshida, T.; Li, C.; Saito, I. *Energy Fuels* **2004**, *18*, 995.
(8) Takanohashi, T.; Li, C.; Saito, I.; Aoki, H.; Mashimo, K. *Proceedings of 12th International Conference on Coal Science* **2003**, 12P10.
(9) Liotta, R. *Fuel* **1979**, *58*, 724.
(10) Liotta, R.; Rose, K.; Hippo, E. J. *J. Org. Chem.* **1981**, *46*, 277.
(11) Blom, L.; Edelhausen, L.; van Krevelen, D. W. *Fuel* **1967**, *36*, 135.
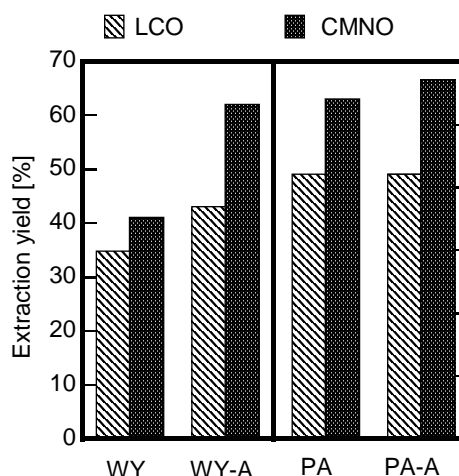(12) Cody, G. D.; Thiyagarajan, P.; Botto, R. E.; Hunt, J. E.; Winans, R. E. *Energy Fuels* **1994**, *8*, 1370.

Table 1. Elemental analysis and ash content of coal used.

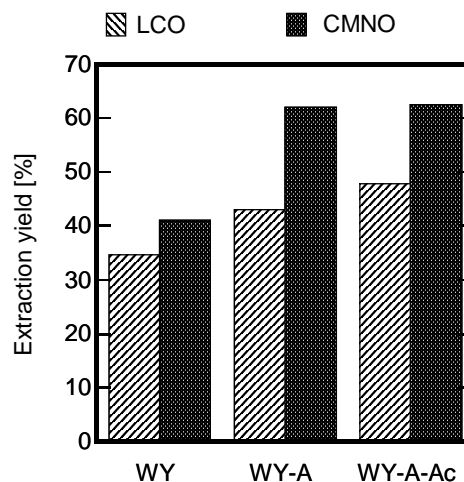| coal | symbol | ultimate analysis [wt%, daf[1)]] | | | | | ash [wt%, db[3)]] |
		C	H	N	S	O[2)]	
Wyodak Anderson	WY	75.0	5.4	1.1	0.5	18.0	8.8
Pasir	PA	73.5	5.3	1.9	0.2	19.1	4.9

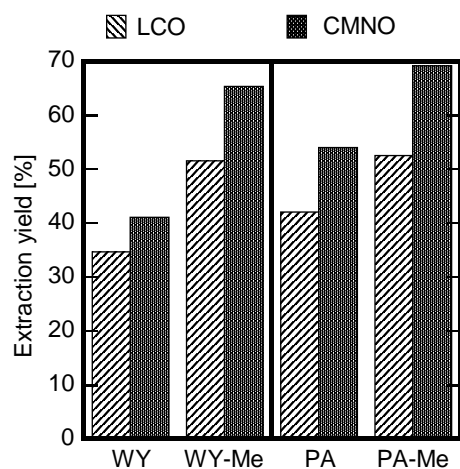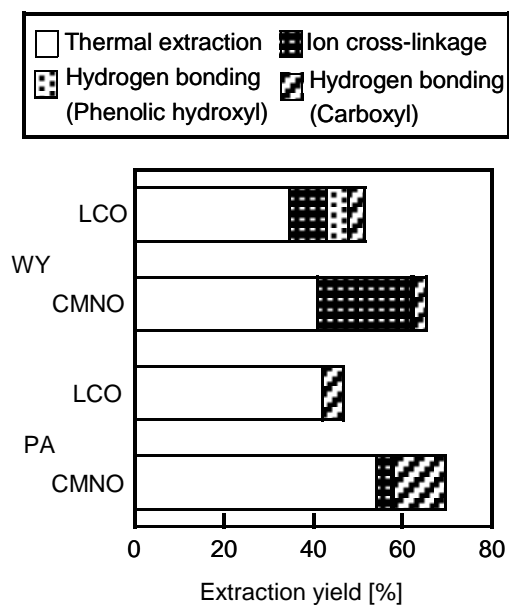a) dry ash free basis
b) by difference
c) dry basis

Figure 1. Extraction yields of WY-Ac and PA-Ac.

Figure 2. Extraction yields of WY-A and WY-A-Ac.

Figure 3. Extraction yields of WY-Me and PA-Me.

Figure 4. Effect of release of non-covalent bonds on the extraction yield.

STUDY ON THE OXIDATION-EXTRACTION DESULFURIZATION TO FCC GASOLINE

Part I The Affects of the Selected Oxidation System on the Desulfurization

Yuhai Wang, Daohong Xia, Yuzhi Xiang

(College of Chemistry & Chemical Engineering, University of Petroleum (East China), Dongying 257061, China)

Introduction

Sulfur compounds exist in various light oils made from petroleum. Such as mercaptan, hydrogen sulfide, which have been undesirable compounds in petroleum since the early days of the industry. In recent years, allowable sulfur levels in fuels have been drastically lowered by government regulations to combat air pollution. The upper limit of sulfur in gasoline in US and Canada for 2005 has been set to 30ppmw[1]. Moreover, the introduction of 'sulfur free fuels(<10ppmw)'has been proposed in Europe for year 2007[2]. The fluid catalytic cracking gasoline contributes to more than 90% to the total gasoline pool sulfur content in China, therefore, it is an urgent problem to reduce sulfur content in FCC gasoline.

At present, there are many studies on the desulfurization methods to light oils. But only seldom are industrialization, such as: solvent extraction, acid and alkaline refining, adsorption desulfurization[3-5]. They all have abuses: there is a lot of waste acid and alkaline which brings great pressure to the environment protection; the adsorption capacity of sorbent is small and it will consume much energy to regenerate the sorbent; the solvent extraction has low rate of desulfurization and oil will lose. So we empoldered a new method-- oxidation-extraction desulfurization. On the result of experiment it has the virtue of high desulfurization efficiency and regenerate simply. This paper reports the effect of factors of oxidation system, including the best condition of the oxidation system, the effects of the circular use of the whole oxidation system, the effect of the proportion of the gasoline with acid and oxidant, the oxidation time and temperature to the desulfurization.

Experimental

Oxidation System. The oxidation system should have strong oxidation ability and no pollution to the environment. On the basis of experiments, catalyst A and oxidant B together was selected as the oxidation system.

Experimental Oil. The FCC gasoline was produced from Shenghua refinery, which was caustic washed with 10m% sodium hydroxide solution.

Chemicals and Apparatus. All solvents and chemicals used in this study were of analytical-reagent grade.
A model of microcoulometric total-sulfur analyzer was used to determine the total sulfur in oil samples. The total sulfur of oil sample(S) was determined with oxidative microcoulometric method.

Materials Calculation. The desulfurization rate of oxidation system(x_1%) as follows:

$$x_1\% = \frac{C_0 - C_1}{C_0} \times 100$$

where:

C_0：the initial total sulfur in oil sample   ug/g
C_1：the residual total sulfur in oil sample   ug/g

Results and Discussion

Effect of Oxidation Time

200ml experimental oil was added to a conical flask and then 20ml catalyst A and 4ml oxidant B were also added, the reaction solution was stirred at the speed of 800rpm under room temperature. Every a period of time a little oil sample was taken out and the total sulfur was determined after the sample washed with water, the results are showed in Figure 1.
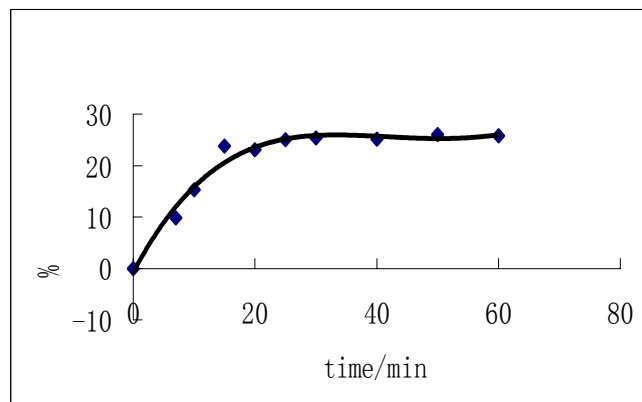

Figure 1. Oxidation time vs desulfurization rate

Figure 1 shows that before 15 min, the desulfurization rate increase rapidly but after 25min, the desulfurization rate becomes steadiness. So the oxidation time may keep in 25min.

The Effect of Quantity of A

Only changing the using quantity of A with unchanging the other oxidation conditions including the using quantity of gasoline, the oxidant B and the reaction time et al, a series experiments were made. The optimism quantity for A can be gained from **Fig.2**.
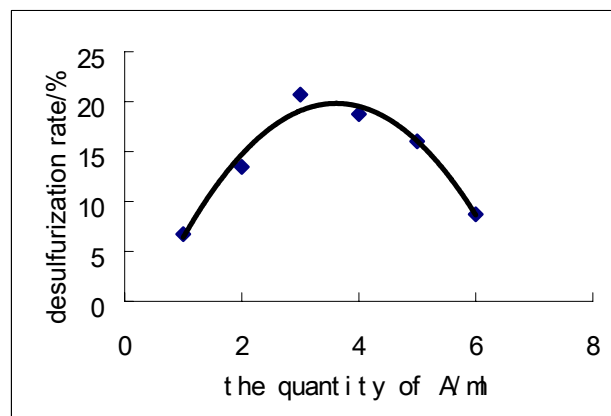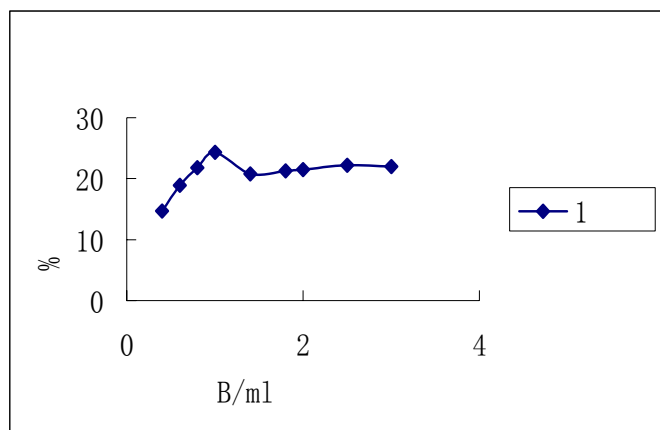

Figure 2. The optimism quantity of A in the oxidation system

From figure 2 it is known that there is an optimism quantity of catalyst A in the reaction. Due to A plays the function of catalyst in the reaction, the oxidant B can not play its function better when the quantity of A is lack. On the other hand, when catalyst A is excessive in the reaction system, it consumes some B, so the desulfurization rate declines also.

The Effect of Quantity of B

Using the same method as the determination of the quantity of A, we can acquire the suitable added quantity of B in Figure 3.

Figure 3. The optimism quantity of B in the oxidation system

The data in **Fig.3** show that with increasing the amount of oxidant B, the desulfurization rate was apt to increase. But when the quantity of B exceeded 1ml, the desulfirization rate stayed invariableness. Based on the above experiments, we can get the best proportion between the oil, catalyst A and oxidant B is 50:5:1.

The Effect of Temperature on the Oxidation System

It is reported that the temperature has effect on the oxidation reaction. Only changing the temperature with the experiments, the results are showed in Figure 4.
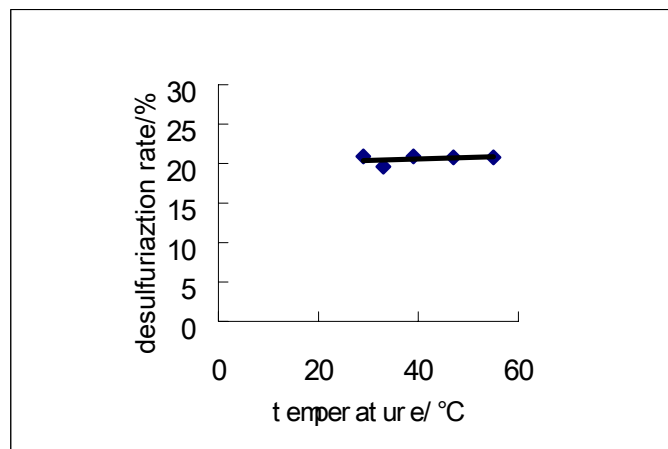
Figure 4. The effect of temperature to oxidation reaction

Figure 4 shows that in the range of 30-50℃, the desulfurization rate was invariableness. This could prove that the oxidation system was unaffected by temperature in our experiments.

Circular use of the Oxidation System

With the best proportion of gasoline, catalyst A and oxidant B, the circular use of the oxidation system was approached. After the reaction taking 25min, gasoline was separated, and the oxidation system was reused without changing other conditions. The results can be gained in Figure 5**.**
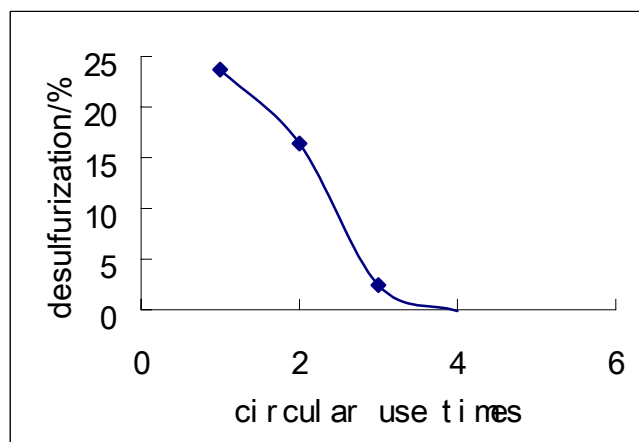
Figure 5. The circular use times of the oxidation system

We can see from Figure 5 that with the reuse times increasing of the oxidation system, the desulfurization rate is dropping. The reason may be that the oxidant B was remained less and less in the oxidation system with the increasing of the using times. At last the oxidant B was used up and the desulfurization rate become to zero.

Conclusions

1 With the acid A/oxidant B system the oxidant reaction time may keep in 25min.

2 The proportion of catalyst A /oxidant B play an important role in the reaction. The best proportion between the oil, catalyst A and oxidant B is 50:5:1.

3 In the range of 30-55℃,the temperature has no effect on the oxidation system. The more circular use the oxidation system, the lower the desulfurization rate is.

References

(1) Balko J,Podratz D,Olesen J. Proceedings of the NPRA Annual Meeting,Paper AM-00-14,St Antonio,TX 2000
(2) Nocca JL, Cosyns J,Debuisschert Q,Didillon B.Proceedings of the NPRA Annual Meeting,Paper AM-00-14,St Antonio,TX 2000
(3) Kozlowski; Eric F.,U.S.Pat. ,4,885,828,**1989**
(4) Nagji; Moez M. (Yonkers, NJ); Holmes; Ervine S.,U.S.Pat.，No.4,830,733,**1989**
(5) Brannon; Judeth H. (Baton Rouge, LA); Schorfheide; James J. (Baton Rouge, LA)，U.S.Pat.，No.4,449,991,**1984**

# TEMPERATURE DYNAMICS DURING CATALYTIC PARTIAL OXIDATION OF METHANE IN A REVERSE-FLOW REACTOR

Tengfei Liu and Götz Veser

Chemical Engineering Department
1249 Benedum Hall, University of Pittsburgh
Pittsburgh, PA 15261

Introduction

The catalytic conversion of methane to synthesis gas is a key technology in the petrochemical industry. Its importance is expected to increase in coming decades due to an ongoing shift in the petrochemical industry from oil towards natural gas as primary feedstock, as well as the increasing significance of fossil and bio-renewable methane for a future 'hydrogen economy'.

In recent years, the direct catalytic partial oxidation of methane (CPOM) has emerged as a technologically interesting alternative to the currently dominating steam reforming and autothermal reforming routes for syngas production [1]:

$$CH_4 + 0.5\ O_2 = CO + 2\ H_2 \quad (\Delta H_R = -37\ kJ/mol)$$
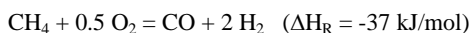
The reaction is characterized by extreme reaction temperatures exceeding 1000°C, which results in very high reaction rates and thus extremely short residence times in the millisecond range [2]. The high reaction temperatures also restrict the choice of catalyst, and noble metal catalysts (Pt, Rh) are typically used.

We have previously shown that the extreme temperatures observed at autothermal conditions arise due to a complex interplay of total and partial oxidation pathways [3]: Preferential oxygen adsorption on the catalyst surface results in a local over-oxidation of the catalyst at the front edge, which results in the strongly exothermic total oxidation of parts of the methane feed [4]. While this is obviously detrimental for syngas yields, it also yields the high temperatures that are thermodynamically necessary to shift the reaction route towards partial oxidation of methane. The need for sufficiently high temperatures therefore effectively limits the syngas yields attainable at autothermal reactor operation [3].

This thermodynamic limitation can be overcome through heat-integration in a multifunctional reactor configuration [3-5]. We have previously reported strong improvements in syngas yield for CPOM in a dynamically operated reverse-flow reactor (RFR) [3]. In this reactor configuration, very efficient heat-integration is achieved by periodically switching the flow-direction of the gases through the reactor, while heat-reservoirs (so-called inert zones) before and after the catalyst as well as the catalyst bed itself act as regenerative heat exchangers. In the present paper, we report new insights into the heat-integration in this high-temperature RFR via in-situ spatio-temporal temperature measurements.

Experimental

The experimental setup used for the investigations is shown in figure 1. The reactor consists of a quartz-glass tube with catalyst and inert-zones, which is inserted into a metal housing. The inert zones consist of cordierite extruded monoliths (1.7 cm diameter, 11cm long). In contrast to our previous studies, we used Pt-coated *extruded* alumina monolith (1.7cm diameter, 1cm long) which had been prepared by standard impregnation procedures. The straight-channel structure of the extruded monolith (in contrast to the tortuous structure of the alumiona foams [4]) allows the insertion of moveable thermocouples and thus the online measurement of the spatio-temporal dynamics of the temperature throughout the reactor and the catalyst zone at operating conditions.

Flow-reversal is accomplished with four magnetic valves, positioned as shown in figure 1. Reactor operation and data acquisition were computer controlled. The reactants (CH_4 and air) were fed via standard mass-flow controllers and product gases were analyzed with a double-oven gas chromatographic system. For direct comparison of the results at reverse-flow operation with results from conventional (i.e. steady state) reactor operation, the same reactor setup was used for steady state experiments. This assured that all differences between steady state results and results at reverse-flow operation were exclusively due to the differences in reactor operation rather than differences in the experimental setup.
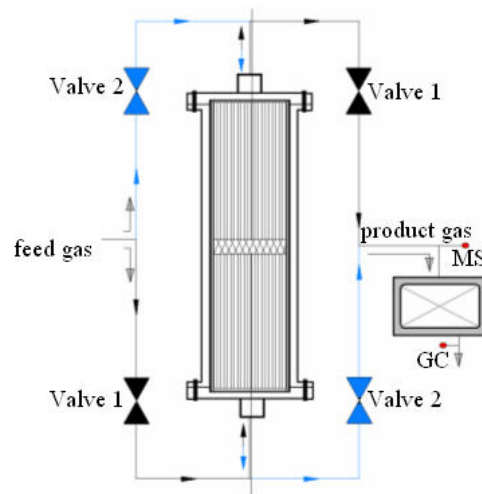

Figure 1. Schematic of the experimental reverse-flow reactor system used for investigating the partial oxidation of methane

Results and Discussion

Even without inspection of temperatures inside the catalyst, the effect of regenerative heat-integration at reverse-flow operation of the catalytic reactor is immediately apparent from temperature profiles inside the inert zones surrounding the catalyst zone. Figure 2 shows temperature profiles in one of the inert zones at steady-state ('SS') and reverse-flow operation ('RFR') for a CH_4/O_2 ratio of 2.0, and an inlet flow rate of 1 slm. For RFR operation, temperatures were averaged over one full cycling period of $\tau = 30s$. The catalyst is positioned at $z = 11 – 12cm$, i.e. to the right of the curves. Gases were fed at room temperature, and, at steady state operation, flow from left to right.

One can clearly see that the regenerative heat-integration at RFR operation leads to a strong increase of the feed gas temperature at the catalyst entrance ($z = 11cm$): the temperature increases strongly from about 400°C at steady state operation to about 800°C at RFR operation. It is interesting to note that even at steady state operation the temperature of the inlet gases is significantly increased above room temperature before reaching the catalyst zone. This increase is due to heat conduction in the solid phase of the inert zone. In contrast to that, the much stronger temperature increase at reverse-flow operation is due to direct heat transfer between the inert zones and the gas phase, as will become more apparent further below.

The temperature profiles in figure 2 also show that temperatures at the entrance of the inert zone are increased by less than 100°C through reverse-flow operation despite the strong increase in temperatures at the catalyst. This indicates how efficiently heat is truly *integrated* in the reverse-flow operation of the reactor. The resulting "cold in – cold out" effect is an additional benefit of heat-integration for high-temperature catalysis, where the temperature of the reactor effluent can lead to significant problems in the downstream handling of the product gases.
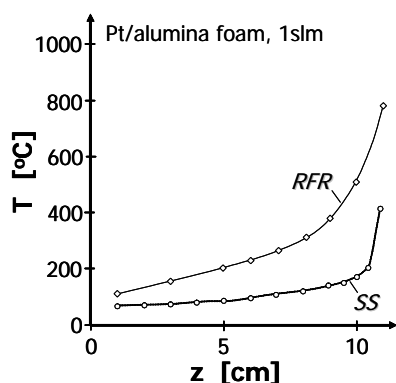
Figure 2. Temperature profiles in the upstreams inert zone at steady state operation (circles, 'SS') and temperatures in the inert zone (averaged over one full period) at RFR operation (diamonds, 'RFR').

The above outlined operational principle of the RFR becomes more apparent in the full, time-dependent temperature profiles throughout the catalyst zone and one of the inert zones at RFR operation shown in figure 3. Time-dependent temperature profiles are shown for two full periods with three different periodicities (top row and bottom right graph) along with methane conversions and syngas selectivities as a function of period (bottom left). The catalyst is positioned at z = 0 – 10 mm in the temperature profiles. In all graphs flow direction is initially from left to right.

One can again recognize strongly increased catalyst inlet temperatures at all three periodicities: the gases reach the catalyst zone at temperatures well above 800°C. (The increase over the temperatures shown in fig. 2 is due to the higher flow rate of 2 slm for the data in fig. 3 vs 1slm for fig. 2). However, the flat contour lines for a flow reversal period of 2s (top left graph) indicate that this period is too short to allow the heat integration to function efficiently: flow reversal is too fast for the thermal dynamics of the inert zones to follow, and an (almost) time-invariant temperature profile develops in the inert zones. Poor heat integration also results in (relatively) low conversion and selectivities as seen in the bottom left graph.

Increasing the period to 25 s, the reverse-flow operation starts to 'pump' the heat reservoirs very efficiently as apparent from the strong temporal temperature gradients (top right graph). This results in even higher preheat temperatures and hence strongly increased temperatures in the catalyst zone (>1200°C) which lead to further increases in syngas yields.

Further increasing the period to 100s, the efficiency of the heat integration is significantly reduced again, resulting in a drop in conversion and selectivity. The reason for this lies in the exhaustion of the heat reservoir supplied by the inert zones, as apparent in the spatio-temporal temperature profiles (bottom right graph): After less than 50s in each half cycle the contour lines for the temperature close to the catalyst (z = 10-40mm) flatten, indicating that no further heat exchange is occurring in these areas. Hence, as soon as the temperature profiles in the inert zones start to flatten, maximum temperatures inside the catalyst zone decrease, which then leads to less selective reactions, i.e. a drop in selectivity and conversion.

Interestingly, despite the very high flow velocities in these reaction systems, the reaction front remains 'pinned' to one spot at reverse-flow operation, rather than showing the traveling front that is typically observed in a RFR. Clearly, the kinetics of the catalytic oxidation reaction is so fast at these high temperatures that no displacement can be induced by the gas flow, and the kinetic and thermal dynamics of the reactor hence become completely uncoupled.
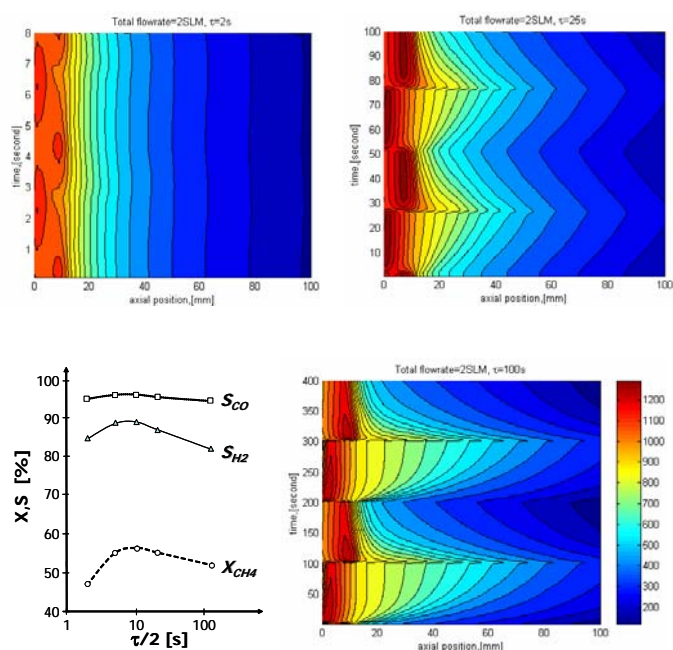
Figure 3. Spatio-temporal temperature profiles inside the catalyst (z = 0-10mm) and one inert zone during four half-periods (i.e. four flow reversals) for a flow reversal half-period of 2 s, 25s and 100s, respectively (clockwise from top left). The bottom left graph shows the corresponding methane conversion (circles), H_2 selectivity (triangles) and CO selectivity (squares) as a function of periodicity.

Conclusions

We presented results from an investigation of spatio-temporal temperature profiles during CPOM in a reverse-flow reactor. The measurement of temperature profiles throughout the reactor and the catalyst illustrate the operation principle of the RFR at high-temperature conditions. The importance of the cycling period and its influence on syngas yields could be explained by the lack of sufficient time for heat transfer at very short periods, and the exhaustion of the heat reservoirs at very long periods. Finally, a complete decoupling of the kinetic and thermal dynamics of the reactor was observed at these high-temperature conditions. This opens up easy ways for process improvement through optimization of the inert zones.

Future Work. We are currently investigating the influence of RFR operation on catalyst stability, which poses a significant problem for high-temperature catalysis. Interestingly, first results indicate that dynamic heat-integration can also lead to a (partial) compensation of catalyst deactivation.

References

(1) Prettre, M., C. Eichner, and M. Perrin, *Trans. Faraday Soc.*, **1946**. 43: p. 335.
(2) Hickman, D.A. and L.D. Schmidt, *Science*, **1993**. 259: p. 343.
(3) Neumann, D., and G. Veser, *AIChE J.,* **2004**, in print.
(4) Veser, G. and J. Frauhammer, *Chem. Eng. Sci.*, **2000**. 55: p. 2271-2286.
(5) Friedle, U. and G. Veser, *Chem. Eng. Sci.*, **1999**. 54(10): p. 1325-1332.

THE SYNTHESIS OF CERTAIN AZIDES FOR IMPROVED CETANE NUMBER BY PHASE TRANSFER CATALYSIS

Wenxun Yan   Yuzhi Xiang   Daohong Xia

(College of Chemistry & Chemical Engineering, University of Petroleum, Dongying 257061, China)

INTRODUCTION

Stringent diesel engine emissions regulations are being implemented worldwide. It is widely accepted that increasing the cetane number is one way to produce cleaner burning diesel fuels[1,2]. This increase can be done by lowering the aromatic content of the fuel through hydrotreatment, adding chemical cetane improvers, or both. It is generally recognized that the use of chemical cetane improvement additives is less expensive than hydrotreatment. Moreover, deep hydrotreat- ment to reduce aromatics tends to adversely affect some fuel properties.

Alkylazide was first recognized as effective cetane improver in the 1980s[3]. Traditional way for the synthesis of alkylazide is as following[3]:

$$RX \ + \ NaN_3 \xrightarrow{\text{DMF or DMSO}} RN_3 \ + \ NaX$$

RX is alkyl halide, X=Cl, Br. By reaction of alkyl halides with sodium azide in dipolar aprolic solvents such as dimethylformamide (DMF) and dimethyl sulfoxide (DMSO). Low yield, the high temperature of reaction and difficulty for the division of the product are the obvious disadvantages of this way. In order to overcome all of the disadvantages above,, this paper has designed a new method for the synthesis of alkylazides, which is a reaction of phase transfer catalysis. Alkylazides such as n-butylazide, isobutylazide, isopropylazide, amylazide, isoamylazide, octylazide and so on, can be synthesized by phase transfer catalysis. The synthesis of n-butylazide is stated in this paper to expound this reaction of phase transfer catalysis.

EXPERIMENTAL

Sodium azide were purchased from Aifute company(JiNan,China) and other chemicals are of analytical grade quality. IR spectrum obtained from *Nicolet–FTIR*, and Elemental analyses for C, H, N were carried out on an Elementar Vario EL–III analyzer.

Preparation of the complexes. The 13.7g(0.1mole) of n-Butyl bromide was dissolved in 50 ml of dichloromethane, this solution was then added to a solution of 7.15g(0.11mole) of sodium azide in 50 ml of water containing 0.21g phase transfer catalyst (tetrabutyl ammonium bromide). The addition was carried out under reflux conditions(41centigrade) with agitating for 3 hours. 9.03g of product was then separated from the mixture as achromatous liquid through distillation of decompression, and yield rate reaches to 91.1%. The solvent of dichloromethane and the phase transfer catalyst can be recycled.

Physical measurement. The purity of the product was measured by gas chromatography on *3420-gas chromatogram*, and was found 98.9%. The product was found to have a boiling point at 50centigrade–51centigrade under the pressure of 60mmHg, and the refractive index measurements were carried out on the refraction apparatus of WZS–at 25centigrade, that is n_D^{25}=1.4188(from document[4], n_D^{20}=1.4196). The density of the product is measured under 25centigrade by using pycnometer, that is d_4^{25}=0.992g/ml.

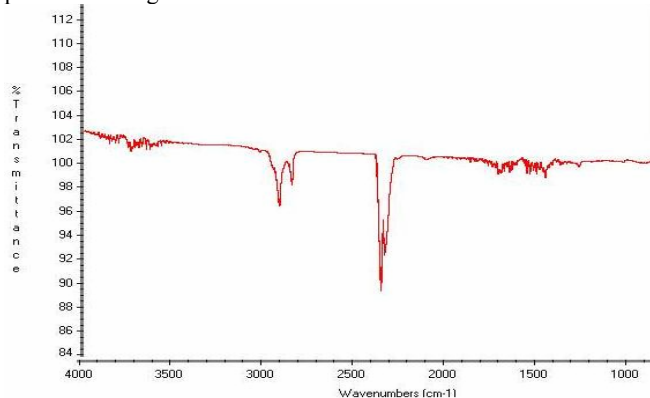**The structural characterization.** The IR spectrum of the product is as fig.1.

Figure 1. The IR spectrum of the product

The IR spectrum exhibits the existence of –N_3 at 2300 cm^{-1}. The datum of Elemental analysis are found: C, 48.50; H, 9.10; N, 42.36(%). Calc. for $C_4H_9N_3$: C,48.48; H, 9.09; N, 42.42(%).

Both IR spectrum and Elemental analysis show that the synthesis product is just what the author needs and the structure of the product can be confirmed as following: $CH_3CH_2CH_2CH_2$–N_3.

RESULS AND DISSCUSSION

The phase transfer catalysis mechanism of this reaction [5]. The mechanism of this reaction of phase transfer catalysis is as figure2, and RX stands for n-Butyl bromide, Q^+ stands for the cation of the phase transfer catalyst.
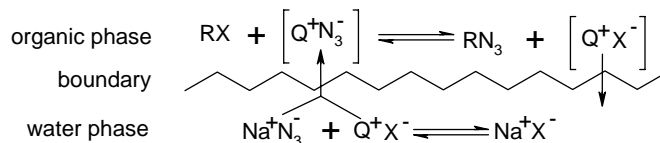

Figure 2. The mechanism of this reaction

In the figure, the N_3^- was extracted to the organic phase by phase transfer catalyst in the water phase through the process of exchange of ions, after the N_3^- was reacted with RX, the cation of phase transfer catalyst transmitted the ruptured X^- to the water phase. This process was repeated without cease as long as the reaction was uncompleted, therefore the N_3^- was extracted to the organic phase until the reaction being completed.

The advantages of the phase transfer catalysis. Using traditional way [5], the temperature of reaction is 90centigrade or so, the yield rate is 70% or so, the separation and recycle of the solvent are complex because of the strong polarity of the solvent. Compared with the traditional way, the way of phase transfer catalysis the author designed has several advantages: the temperature(41centigrade) of reaction is lower, the yield rate(91.1%) is higher and the separation of the product is easier because of the tiny polarity of the solvent, the solvent can be recycled more easily because of the low boiling point(40.5centigrade) of the solvent. All of the advantages show that the way of phase transfer catalysis the author designed is reasonable and feasible.

The contribution to cetane number of the synthesis product. The synthesis product was directly added to diesel fuel which obtained from *general petrochemical factory of Shengli* and whose primal cetane number is 39 to examine the contribution to cetane number, the cetane number of the diesel fuel is measured in

Qilu petrochemical factory. The datum are as tab.1.

Table 1. The examination of contribution to cetane number

Contration(m%)	0.30	0.50	0.70
ΔCN	+2	+4	+5

Tab.1 shows that the product can do good to cetane number of diesel fuel considerably.

CONCLUSIONS

1. The phase transfer catalysis applied to the synthesis of alkylazides such as n-butylazide, isobutylazide, isopropylazide, amylazide, isoamylazide, octylazide is appropriately feasible. Compared with the traditional procedure, the temperature of reaction is lower, the yield rate is higher and the separation of the product is easier, the solvent can be recycled easily.

2. The addition of n-butylazide can improve the cetane number of diesel fuel considerably, when it is added into diesel fuel at concentration of 0.70m%, cetane number can be improved 5. It can be considered as a   kind of promising cetane number improver.

LITERATURE CITED

[1] Nandi M.K., Jacobes D.C., Kesling H.S. The performance of a peroxide-based cetane improvement additive in different diesel fuels, SAE Paper 942019, October 1994.
[2] Nandi M.K., Jacobes D.C. Cetane response of different di-tertiary-butyl peroxides in different diesel fuels, SAE Paper 952369, October 1995.
[3] Frankel, Milton B. Azido additives for liquid hydrocarbon motor fuels USP4303414,1981
[4] Reeves,W.P.et al, The synthesis of alkyl azides, *Synthesis*,1976,823.
[5] Wang naixing, Organic Reaction–The Reactions Of Polynitrogen Compounds And Some Theoretic Questions, *Publishing Company of Chemical Industry*, BeiJing,2003, Page185-186.

HYDROGEN ADSORPTION OF SINGLE-WALLED CARBON NANOTUBES UNDER HIGH PRESSURE: A COMBINED NUCLEAR MAGNETIC RESONANCE AND RAMAN STUDY

Kai Shen[1], Seamus Curran[2], Huifang Xu[3], Yingbing Jiang[4], James Dewald[2], Jamal Talla[2], and Tanja Pietraß[1]

(1) Department of Chemistry, New Mexico Tech, Socorro, NM 87801, tanja@nmt.edu, (2) Department of Physics, New Mexico State University, (3) Department of Geology and Geophysics, University of Wisconsin, Madison (4) Department of Earth and Planetary Sciences, University of New Mexico

Introduction

Hydrogen storage on carbon nanotubes (CNTs) has attracted intensive research activities since Dillon et al claimed a possible 5-10 wt% storage capacity under ~ 1 atm hydrogen pressure.[1] Subsequent studies, however, show a wide divergence in the reported hydrogen storage capacities of CNTs.[2,3] In our previous studies, hydrogen adsorption has been demonstrated to be physisorption-like under hydrogen pressures up to ~1.5 MPa.[4] Under pressures higher than 4 MPa, a sudden increase in tube distance in single-walled carbon nanotube (SWNT) ropes was proposed to account for a storage capacity up to 8.25 wt%.[5] In this study, we employed nuclear magnetic resonance (NMR) and Raman spectroscopy to reveal the hydrogen adsorption behavior in SWNT ropes at room temperature and pressures over 4 MPa.

Experimental

High pressure samples were prepared by exposing an arc-discharge produced SWNT sample (MER Corp., AZ) to a hydrogen pressure of 14.3 MPa for 24 h. The pressure was released and the sample was sealed in an inert atmosphere. Prior to hydrogen exposure, the samples were heated under vacuum (10^{-3} Pa) at 853 K for 2 h to remove any adsorbates. ^{1}H and ^{2}H NMR spectra of the SWNT sample were acquired at room temperature and at a Larmor frequency of 400.127 and 61.423 MHz, respectively. ^{2}H NMR facilitates differentiation between the adsorption and gas phase. Raman spectra were acquired on a Renishaw inVia Raman Microscope equipped with different laser excitation wavelengths. The metal content was measured using inductively coupled plasma/mass spectrometry (ICP-MS) and the SWNT morphology was studied using transmission electron microscopy (TEM).

Results and Discussion

Structural features characterization. Figure 1 shows the transmission electron micrograph of the SWNT sample. The average bundle size, obtained from 120 measurements, is ~ 18 nm. The content of metallic impurities (Figure 1) , mainly Co and Ni, in the pristine sample is 32 wt%.[6]

The radial breathing mode (RBM) at different excitation lines is used to determine the diameter range of the tubes.[7] Raman excitation at 1.58 eV is resonant with semiconducting tubes within a diameter range of 0.9 – 1.1 nm, while 2.41 eV excitation can either be in resonance with 1.2 – 1.4 nm semiconducting tubes or metallic tubes of 0.9 – 1.1 nm diameter. It is estimated that the diameter range for all type tubes is 0.9 – 1.4 nm.
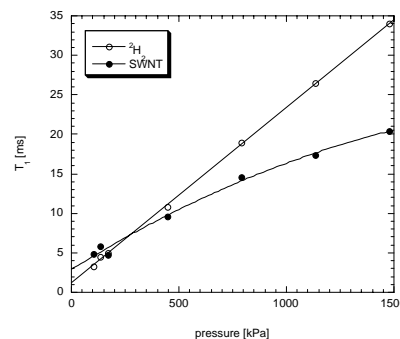
Hydrogen adsorption at low pressures. ^{2}H NMR spin-lattice relaxation times T_1 as a function of H_2 pressure are shown in Fig. 2 for the SWNT sample and pure deuterium gas. T_1 linearly increases with pressure for the pure gas.[8] The spin relaxation times for the unpurified SWNT sample are not linear with pressure and

significantly shorter at pressures greater than 500 kPa. Pure deuterium T_1s follow a spin-rotation mechanism while this is not the case for deuterium in contact with the SWNT sample. Here, relaxation may be induced by interaction with conduction electrons or paramagnetic impurities which is in agreement with the observed shifts. It should be noted that the ^{2}H signal disappeared completely upon evacuation, indicating physi-sorption.

Figure 1. TEM micrograph of the parent SWNT sample.
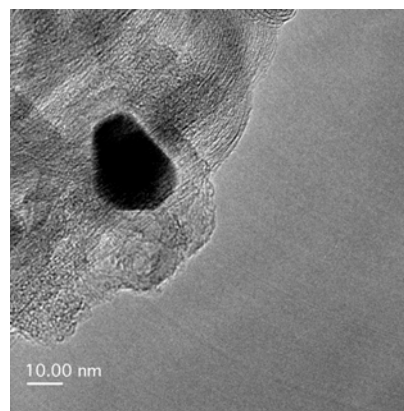
Figure 2. ^{2}H NMR spin-lattice relaxation data for SWNTs exposed to deuterium gas, and for pure gas as a function of pressure at ambient temperature. For H_2, the line is a linear fit to the data points, while it merely serves to guide the eye for the SWNT sample.


Hydrogen adsorption at high pressures. Although the excess pressure was released prior to sealing, intensive ^{1}H signals persisted. This is a clear indication that hydrogen is bound to the sample either by strong physisorption or even chemisorption. In order to test this hypothesis, ^{1}H NMR T_1s of the adsorbed phase for the high (14,489 kPa) and low pressure sample (136 kPa) were compared. T_1 is significantly longer at high pressure. We measured T_1s of 205 ms and 12 ms, respectively. The pronounced difference in relaxation rates suggests either different physisorption sites or a different adsorption type, i.e. chemisorption. The magnetization profile of the high pressure sample can be fitted with a single exponential function, implying that only one relaxation mechanism is dominant. The pressure dependence of T_1 is linear over the entire pressure range (Figure 3).

To elucidate hydrogen adsorption behavior, the high pressure sample was heated at 373 K for 5 min. The intensity of the broad adsorption peak decreased with a sharp gas peak dominating the ^{1}H NMR spectrum. Therefore, the desorption of adsorbed hydrogen renders chemisorption an unlikely scenario, because a much higher

temperature is required to break C-H bonds and to release hydrogen gas. The ^{1}H NMR T_1 of the high pressure sample was significantly reduced to 87 ms after heating, indicating a more efficient relaxation after hydrogen desorption. This is most likely due to a decrease in interaction of hydrogen with the SWNT surface, and the contribution of spin-rotation to T_1 becoming once more predominant.

Figure 3. ^{1}H NMR spin-lattice relaxation data for SWNTs exposed to hydrogen gas as a function of pressure. The T_1 dependence on pressure is linear over the entire pressure range.
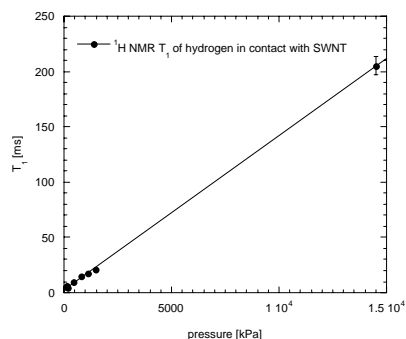
These phenomena can be explained by the adsorption of hydrogen molecules in the interstitial channel (IC) sites within SWNT bundles. It has been demonstrated that IC sites have the highest adsorption potentials among all possible adsorption sites in the bundle.[9] The relatively inefficient relaxation for the high pressure sample can be ascribed to the confinement of hydrogen molecules in IC sites. Although dipolar relaxation can also play a role in relaxation,[10] it is unlikely that dipolar relaxation contributes significantly. If dipolar relaxation among ^{1}H molecules were dominant, a shorter T_1 would be expected at higher pressures which is not observed. When heating to 373 K, a substantial amount of hydrogen desorbs from the sample surface.

In a bundle composed of tubes with a dispersion in diameters as suggested from the Raman results, the coupling between the tubes is reduced due to a mismatch in the SWNT lattice.[11] The localized coupling facilitates the expansion of SWNT bundles as suggested by Ye et al.[5] and therefore may assist hydrogen molecules to access IC sites.

Conclusions

Hydrogen adsorption at pressures up to 15 MPa was studied by a combination of NMR and Raman spectroscopy. Hydrogen most likely physisorbs inside the interstitial channels at room temperature. The adsorption activation energy is estimated to be less than 23 kJ/mol.

References
(1) Dillon, A. C.; Jones, K. M.; Bekkedahl, T. A.; Kiang, C. H.; Bethune, D. S.; Heben, M. J. *Nature* **1997**, *386*, 377.
(2) Ding, R. G., Lu, G. Q., Yan Z. F. and Wilson, M. A. *J. Nanosci. Nanotechnol.* **2001**, *1*, 7.
(3) Hirscher, M.; Becher, M. *J. Nanosci. Nanotechnol.* **2003**, *3*, 3.
(4) Shen, K.; Pietraß, T. *J. Phys. Chem. B* **2004**, *108*, 9937.
(5) Ye, Y.; Ahn, C. C.; Witham, C.; Fultz, B.; Liu, J.; Rinzler, A. G.; Colbert, D.; Smith, K. A.; Smalley, R. E. *Appl. Phys. Lett.* **1999**, *74*, 2307.
(6) Shen, K.; Tierney, D. L.; Pietraß, T. *Phys. Rev. B* **2003**, *68*, 165418.
(7) Kataura, H.; Kumazawa, Y.; Maniwa, Y.; Umezu, I.; Suzuki, S.; Ohtsuka, Y.; Achiba, Y. *Synth. Met.* **1999**, *103*, 2555.
(8) Lipsicas, M.; Bloom, M. *Can. J. Phys.* **1961**, *39*, 881.
(9) Adu, C. K. W.; Sumanasekera, G. U.; Pradhan, B. K.; Romero, H. E.; Eklund, P. C. *Chem. Phys. Lett.* **2001**, *337*, 31.
(10) Armstrong, R. L. Longitudinal nuclear spin relaxation time measurements in molecular gases. In *NMR*; Diehl, P., Fluck, E., Kosfeld, R., Eds., 1976; Vol. 13; pp 71.
(11) Maarouf, A. A.; Kane, C. L.; Mele, E. J. *Phys. Rev. B* **2000**, *61*, 11156.

IN-CYLINDER COMBUSTION VISUALIZATION OF ULTRA LOW SULFUR, NEAT BIODIESEL AND BIODIESEL BLENDED FUELS

Mahabubul Alam, Juhun Song and André Boehman

The Energy Institute
The Pennsylvania State University
405 Academic Activities Building
University Park, PA 16802

Introduction

The Environmental Protection Agency (EPA) has proposed an ultra low (15ppm) sulfur diesel fuel beginning in 2006. The introduction of ultra low sulfur diesel fuel might reduce particulate emissions, particularly the particulate matter (PM) associated with sulfates. Also, sulfur sensitive exhaust gas aftertreatment may be used to reduce other emissions from the exhaust gas [1]. Many studies have been performed with biodiesel and oxygenated diesel fuels and almost all of them showed a significant potential to reduce emissions [2-3].

Biodiesel and oxygenated fuel blends are currently of great interest and active research for PM reduction from diesel engines to meet future, stringent emissions regulations. Biodiesel fuels contain roughly 11 wt.% oxygen and the addition of oxygen containing hydrocarbons to diesel fuel offers an effective means to reduce particulate emissions [3]. The higher cetane number of biodiesel and many oxygenates may enhance combustion performance in compression ignition engines.

In this paper, we present results from in-cylinder imaging in a Cummins 5.9L, turbocharged, six-cylinder, 4-stroke direct injection (DI) diesel engine using an engine videoscope system. The imaging studies provide a comparison of the fuel injection timing, ignition timing, spray formation and flame luminosity between different fuels. Results are presented for an ultra low sulfur diesel fuel with 15 ppm sulfur content ("BP15"), a 100% biodiesel ("B100") and for a 20 wt.% biodiesel blended with BP15 ("B20"). Table 1 shows some selected properties of these test fuels.

Table 1. Selected fuel properties

Fuel	Density gm/cm3	Cetane Number	Viscosity cSt @40C
BP15	0.837	50.5	2.48
B100	0.866	55.0	3.56
B20	0.846	52.5	2.73

Experimental

Experiments were conducted with a Cummins direct injection (DI) diesel engine. The experimental system consisted of an engine, dynamometer, controller, combustion analysis instrumentation, emissions analyzers and an AVL 513D engine videoscope. The engine was fitted with an electronic control module (ECM) that monitors engine performance and controls different events automatically, especially the start of injection (SOI), injection timing advancement or retardation, etc.

Figure 1 shows how the light source and the endoscope are mounted in the engine. The windows installed into the cylinder head were designed to withstand the high temperatures and pressures prevailing within the combustion chamber and to stay clean under engine operating conditions, since the deposition of soot particles on the window surface would reduce visibility. Figure 2 represents a sketch of the geometric relationship between the fuel injector and videoscope probes. Note that the viewing angle of all the endoscopes was 80 degrees. The depth of field was from 1 mm beyond the lens to infinity and therefore a sharp picture of the combustion chamber was obtained without any focus adjustment.

The engine has been heavily instrumented, with a 0.1 crank angle resolution crank shaft encoder, a cylinder pressure sensor, and a needle lift sensor. The engine and dynamometer are operated through an automated control system. Results are presented at an engine setting of 1800 rpm and 10% load.
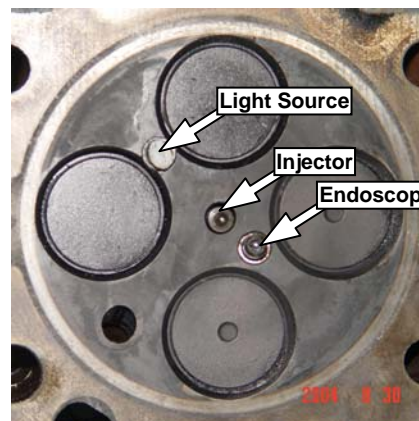

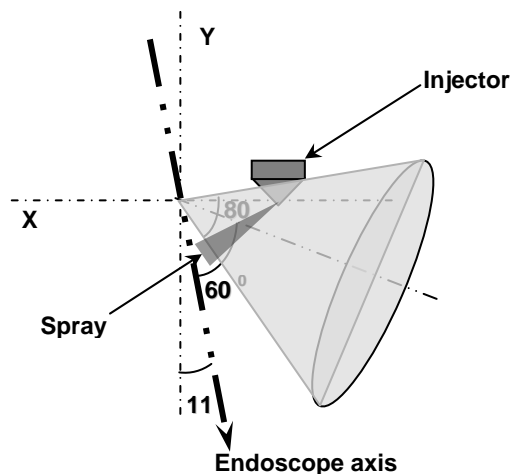**Figure 1.** Endoscope and light source installed on the Cummins 5.9L test engine

Figure 2. A Sketch of the geometric relationship between injector and videoscope probes.
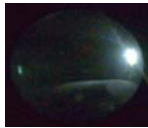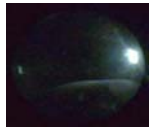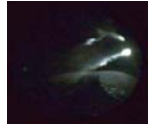
Results and Discussion

The following is a qualitative and quantitative analysis of the spray and combustion characteristics of ultra low sulfur diesel fuel and blends with biodiesel and neat biodiesel. It should be noted that the present study was conducted with an electronically controlled fuel injection system so that injection timing is dictated by the protocols in the ECM. For all the results presented here, the engine was operated at 10% rated load at a constant speed of 1800 rpm.

Figure 3 shows spray images with 0.1 crank angle degrees (CAD) resolution and depicts the start of injection (SOI) with BP15, B20 and B100. For the B100, the injection event starts 0.4 CAD earlier compared to the base diesel fuel whereas, B-20 shows 0.2 CAD earlier injection compared to the base fuel. The density of B-100 is higher than the base fuel, BP15 and the density of B20

blended biodiesel will be higher than the BP15. Therefore, the

advanced injection timing with B20 and B100 is consistent with

Crank angle / Fuel	6.1 deg BTDC	5.9 deg BTDC _SOI B-100_	5.7 deg BTDC _SOI B-20_	5.5 deg BTDC _SOI BP-15_	5.3 deg BTDC	5.1 deg BTDC	4.9 deg BTDC
BP15							
B20							
B100							

Figure 3. Start of injection with ultra low sulfur diesel (BP15), neat biodiesel (B100) and B20 blend.

reported results and arises from an increased fuel density and bulk modulus of compressibility relative to the base diesel fuel [4].

Figure 4 shows rate of heat release (ROHR) and average cylinder temperature analysis of the fuels used in these experiments. The early start of the heat release with B100 is explained by the early start of injection and the cetane number of the fuel. The BP15 fuel shows the highest premixed burn peak among the fuels and all the fuels show that the majority of the combustion occurs during the premixed phase. This is true since the load is only 45 ft-lb and at high load diffusion burning dominates the combustion event [5].
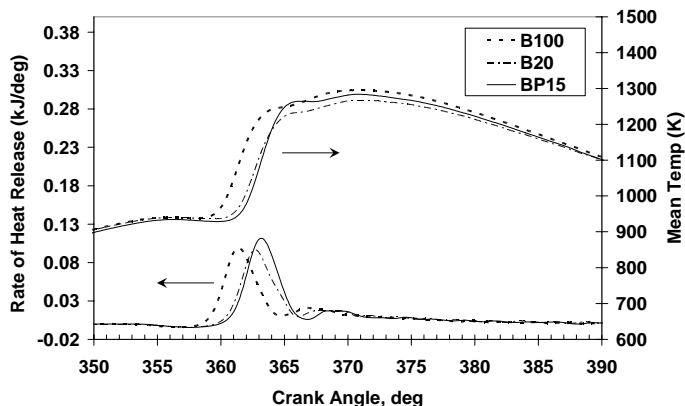
Figure 4. Calculated rate of heat release and average cylinder temperature of the fuels.

The start of combustion is indicated by the CAD when the ROHR curve moves from negative to positive value. In that case, most of the test fuels show that the start of combustion occurs before TDC, whereas the combustion images (Figure 5) show visible flame (VF) after TDC. This might be because the start of premixed combustion is flameless [6] and the viewing window with the endoscope was only 60-70% of the combustion chamber and it was not possible to observe the leading edge of the spray. Therefore, the

start of combustion observed through the endoscope may not be as accurate as the heat release calculation.

The average cylinder temperature or mean temperature is shown in Figure 4. The neat biodiesel (B100) shows the highest average cylinder temperature and base BP15 shows the lowest average cylinder temperature among the fuels. Literature results show that the neat biodiesel fuel generally emits high NO_X and low PM emissions. The high average cylinder temperature might be one of the reasons for high NO_X and low PM emissions with the neat biodiesel fuel. Density and cetane number also play important role in NO_X and PM emissions [5].

Figure 6 presents different combustion events for all the fuels starting from TDC to 30 deg ATDC at an interval of 3.0 CAD. The images of the spray and combustion are at a light load condition. Therefore, combustion is mainly controlled by the premixed burning phase. Although both the B20 and B100 contain fuel oxygen, it is difficult to distinguish between the spray flames of B20, B100 and the base diesel fuel.
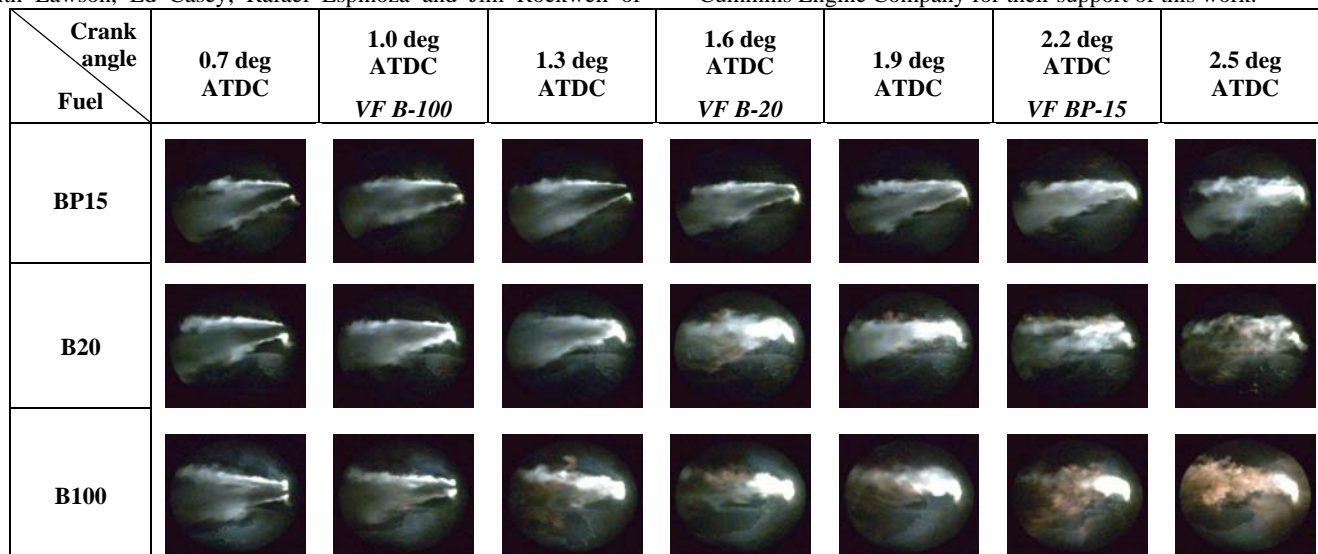
Conclusions

In-cylinder visualization of spray and combustion was performed with 0.1 crank angle degree resolution. Results obtained in this study were very light load conditions. At high loads results might be different than the presented here. Specially, premixed combustion mode and emissions results will be different. However, findings from the present study can be summarized as follows:

1. Early start of injection with B100 and B20 compared to BP15.
2. Among the test fuels, the highest premixed burned peak is observed with BP15, after that with the B-20 blend and the lowest is with B100. This trend is consistent with the cetane number of the test fuels.
3. The highest average cylinder temperature is observed with B100 and base BP15 fuel shows the lowest.
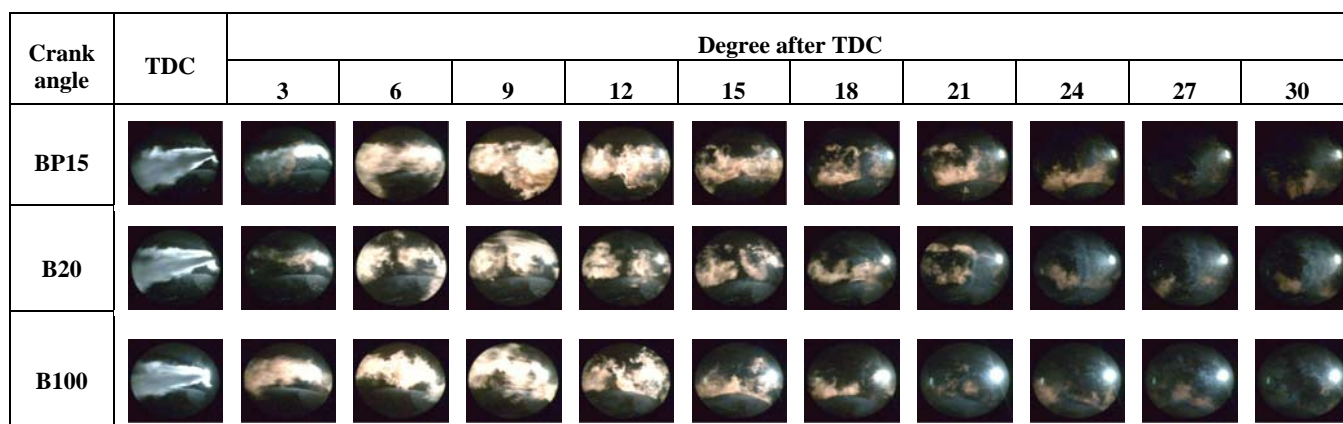
Crank angle \ Fuel	0.7 deg ATDC	1.0 deg ATDC *VF B-100*	1.3 deg ATDC	1.6 deg ATDC *VF B-20*	1.9 deg ATDC	2.2 deg ATDC *VF BP-15*	2.5 deg ATDC
BP15							
B20							
B100							

Figure 5. Start of combustion with ultra low sulfur diesel (BP-15), neat biodiesel and B-20 blend

Crank angle	TDC	Degree after TDC									
		3	6	9	12	15	18	21	24	27	30
BP15											
B20											
B100											

Figure 6. Combustion images from TDC to 30 deg ATDC of the combustion process with 3.0 CAD intervals

References

(1) Diesel Emission Control – Sulfur Effects (DECSE) Program, Final Report: Diesel Oxidation Catalysts and Lean-NO$_X$ Catalysts June 2001, Sponsored by: The U. S. Department of Energy.

(2) Giacomo, N. D., Beatrice, C., and Bertoli, C., "Diesel Combustion Improvements by the Us of Oxygenated Synthetic Fuels", SAE Technical Paper 972972, 1997.

(3) McCormick, R. L., Graboski, M. S., Alleman, T. L., and Herring, A. M., "Impact of Biodiesel Source Material and Chemical Structure on Emissions of Criteria Pollutants from a Heavy-Duty Engine", *Journal of Environmental Science and Technology*, 2001, 35 (9), 1742-1147.

(4) Szybist, J. P., and Boehman, A. L., "Behavoir of a Diesel Injection System with Biodiesel Fuel", SAE Paper 2003-01-1039, 2003.

(5) Alam, M., Song, J., Ragini, A., Boehman, A., and Miller, K., "Combustion and Emissions Performance of Low Sulfur, Ultra Low Sulfur and Biodiesel Blends in a DI Diesel Engine" SAE Paper 2004-01-3024, 2004.

(6) Ishiyama, T., Shioji, M., Ihara, T., and Katsuura, A., "Modeling and Experiments on Ignition of Fuel Sprays Considering the Interaction Between Fuel-Air Mixing and Chemical Reactions", SAE Technical Paper 2003-01-1071, 2003.

CHEMICAL REVERSAL CYCLE OF SOLID OXYGEN CARRIER FOR PRODUCING PURE OXYGEN OR OXYGEN RICH GAS STREAM

Yan Cao, Wei-Ping Pan*

Institute for Combustion Science and Environmental Technology
(ICSET)
Western Kentucky University,
Bowling Green, KY 42101

Introduction

Oxygen and nitrogen are two important feedstocks for a wide range of traditional industries[1]. Examples include the ammonia synthesis, and the gasification of many hydrocarbons to generate synthesis gas for the production of hydrogen, fuels, chemicals and other valuable products, and the growing interest in gas-to-liquids GTL processes which convert natural gas into synthetic crude oil, waxes and fuels. Recently, due to concerns on climate warming by CO_2 emission, increased attention has been focused on CO_2 sequestration in energy production industries where the majority of carbon materials are consumed to produce electricity with emission of a large amount of CO_2 [2-5]. CO_2 sequestration is proposed to inject and store in used oil, coal bed and gas fields, or in aquifers, in deep seas[3]. However, in a conventional energy production system such as combustion and gasification processes, fuel and air directly mixed and reacted that gives rise to the low partial pressure of CO_2 due to nitrogen dilution. This is main limitation to controlling CO_2 emission and will create a significant energy penalty. Methods are imminently pursued to integrate energy production with the oxygen production process[6].

Cryogenic air separation technology has been employed for a long time to supply oxygen for a wide range of industries[5]. However, this oxygen production process faces an economic challenge. Newly developed Non-cryogenic air separation technology includes adsorption such as TSA (Temperature Swing Adsorption) and PSA (Pressure Swing Adsorption)[7], a molten salt chemical process[8], polymer membrane and Ion transport membrane (ITM)[9-10]. Adsorption and polymeric membrane processes will continue to be improved in both cost and energy efficiency. Neither technology is expected to challenge cryogenics for large tonnage production of oxygen, especially at high purities. However, adsorption and membrane processes are less complex and more passive than cryogenic technology. Chemical processes offer the potential for continuous operation and economies of scale through large production output from single trains, but to date have not been able to overcome material corrosion problems. ITM technology is currently foreseen as the best candidate to challenge cryogenics for the production of high purity, tonnage quantities of oxygen.

In this paper, a new concept for oxyhen production is put forth based on a reversible chemical cycle of a solid oxygen carrier. The process analysis including tnermodynamics, kinetics, technical approaches and also potential utilization of the proposed concept will be addressed

Conceptive Development

The concept of the newly developed process for oxygen production is based on a reversible chemical cycle of a solid oxygen carrier，shown in **Figure 1**. The selected solid oxide (MeO) reacts with oxygen in an air stream to produce solid peroxide (MeO$_2$), see

Eq (1). MeO$_2$ releases its oxygen atom and then form oxygen molecule at a relatively higher temperature, see Eq (2). This chemical cycle between re-circulating of solid oxide and its peroxide forms a process for oxygen production continuously. It is important to investigate chemical properties of the solid oxide and peroxide, and the enthalpy and Gibbs free energy of the reactions so that energy input, gas stream purity and possible process configuration and utilization could be evaluated.

$$MeO\,(s) + 1/2O_2\,(g) \rightarrow MeO_2\,(s) \qquad Eq\,(1)$$

$$MeO_2\,(s) \rightarrow MeO\,(s) + 1/2O_2\,(s) \qquad Eq\,(2)$$
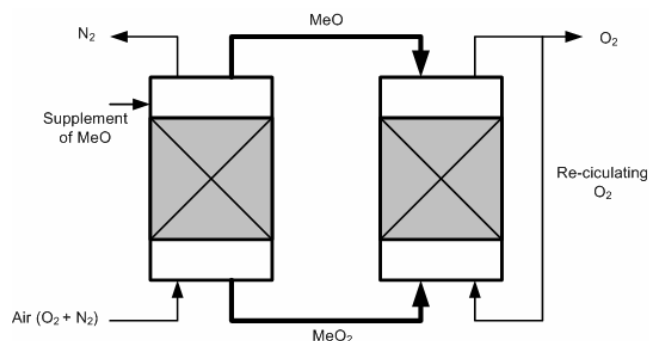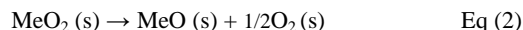
Figure 1. The process concept for oxygen production by a chemical reversal cycle of solid oxygen carrier

Process Analysis

Thermodynamics Analysis. The reversal reaction which is relative with oxygen production process presently interested is a heterogeneous reaction with only one gaseous species. In thermodynamics theory[11], if the gas is ideal then the equilibrium constant expressions for Eq (1) and Eq (2) can not include the solid phase due to the fact that pure solid phases are nearly equal to unity for moderate pressure. Thus, Equation (3) and (4) below are valid for reaction (1) and (2), respectively.

$$k_1 = P_{O_2}^{1/2} \qquad (3) \qquad\qquad k_2 = 1 \Big/ P_{O_2}^{1/2} \qquad (4)$$

The equilibrium constants of k_1 and k_2 for Eq (1) and (2) are independent of the amount of pure solid phases. Their values can be determined by calculation of Gibbs free energy of reactions ccurred. Such as reactions may go to completion if solid phase is used up. The temperature and oxygen partial pressure are the parameters to control reaction direction and extent. If we keep the solid phase is more than enough in view of oxygen, reaction (Eq (1)) can give out pure nitrogen stream. For reaction (Eq (2)), pure oxygen stream can be obtained. The rich oxygen stream can be obtained by using nitrogen as carrier gas.

Technical Approach. The thermodynamic analysis presents positive evidence for proposed concept of oxygen production. The flexible gas compositions can be achieved with obtaining a pure oxygen stream or an oxygen rich stream so that fitting it in different industry process is easy, such as energy production industries which is presently interested. Generally two modes to fit the proposed oxygen production process into the energy industry. It could be combined with the conventional coal combustion process to achieve a high combustion efficiency and CO_2 sequestration, as show in **Figure 2**. In the newly developed chemical looping combustion process, the proposed solid oxygen carrier could easily incorporate solid fuel into the cyclic system due to reaction gas (oxygen stream)

and solid (oxygen carrier) occurred, not the reaction of solid (solid fuel) with solid (solid), as shown in **Figure 3**.

We must mention enthalpy properties of reversal reactions here. If reactions in both directions can be organized into one reactor, an energy self-sustainable module for the proposed process of oxygen production can be achieved. Microchannel reactor can achieve this goal. This technology is being hailed as the next big thing for the process industries[12]. Microchannel reactors consist of stacks of closely spaced thin plates designed to form mirochannels with specific dimensions, regularity, and connectivity in spaces between the plates. Process fluids pass through the channels, which may be coated internally with catalyst or solid oxygen carrier which is presently interested in the proposed process. The microscale dimension of the channel increases the surface area per unit volume and thus increase the overall reaction reactivity and productivity of process per unit volume, and also results in much better heat conductivity for heat transfer. An added advantage is that short residence time of gas stream in the microchannels. The geometry and size of individual channels in microchannel reactors remain the same as process capacity is increased from lab scale to commercial scale. Thus, the scale-up for microchannel is just numbering-up, duplicate the single channel many times which is much different from that of conventional scale up. By connecting multiple microchannel reactors in parallel, it is then possible to achieve any desired plant capacity. That means microchannel-type chemical reversal reactor can compete with conventional cryogenic air separation process in scale with economic and energy advantages, if lab-scale concept could be verified.
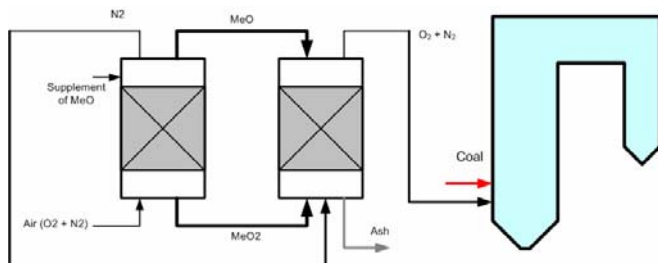
Figure 2. The integration of the proposed oxygen production process with the oxy-fuel energy process
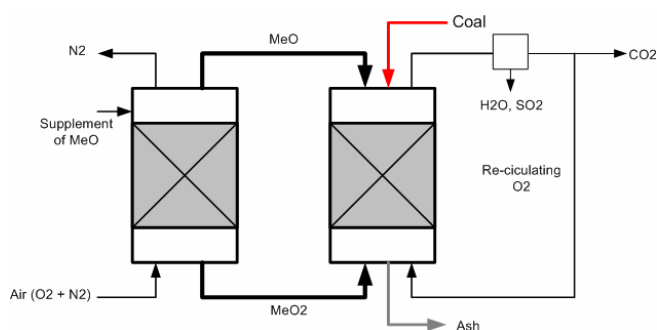
Figure 3. The integration of the proposed oxygen production process with chemical looping combustion by solid fuel or gaseous fuel

Conclusions

A new concept for production of the oxygen stream by a reversible chemical cycle of a solid oxygen carrier is developed in this paper. The possible solid oxygen carrier could be solid oxide and its peroxide. The solid oxide separates oxygen from nitrogen to form solid peroxide and its peroxide produces oxygen stream and is recovered to its solid oxide. Due to the chemical properties of the solid oxide and peroxide, and the enthalpy and Gibbs free energy of the reactions, directions in both reactions can proceed completely with less energy supply needed to operate the whole system. Thus, the newly developed oxygen concept can provide with high purity of oxygen stream and also nitrogen stream in energy economic ways. It's possible to combine reversal reactions into one reactor to achieve an energy self-sustainable module.

The proposed process can directly be integrated into a wide range of industrial processes such as energy production process which is emphasized in this paper. It could be combined with the traditional coal combustion process to achieve a high combustion efficiency and CO_2 sequestration. In the newly developed chemical looping combustion process, the proposed solid oxygen carrier could easily incorporate solid fuel into the cyclic system.

References
(1) Smith, A.R.; Klosek, J.; Fuel Processing Technology. **2001**, 70, 115–134
(2) Bredesen,R.; Jordal K.; Bolland, O. Chemical Engineering and Processing, 2004, 43, 1129–1158
(3) Klara,S.M.; Srivastava, R.D. *Environmental Progress*, **2002**, *21(4)*, 247-253.
(4) Herzog, H.; Drake, E.; Adams, E. "CO_2 Capture, Reuse, and Storage Technologies for Mitigating Global Climate Change," *A White Paper*, Jan, 1997, U.S.DOE/DE-AF22-96PC01257, Washington, DC.
(5) U.S.DOE and U.S. "Environmental Protection Agency. Carbon Dioxide Emissions from the Generation of Electric Power in the United States," Washington, DC, Oct 15, 1999, available at http://www.epa.gov.
(6) Smith, A.R.; Klosek, J.; Woodward, D.W. Next-generation integration concepts for air separation units and gas turbines, J. Eng. Gas Turbines Power, **1997**, 119 (2), 298–304, April.
(7) Cryogenics and Ceramic Membranes: Current and Future Technologies for Oxygen Supply in Gasification Systems, Gasification For The Future, 4th European Gasification Conference, April, Noordwijk, The Netherlands, **2000**.
(8) Dunbobbin, B.R.; Brown, W.R., Air separation by a high temperature molten salt process, Gas Sep. Purif. **1987**, 1, 23–29, September.
(9) Bennett, D.L.; Dyer, P.N.; Ionic transport membrane technology for gas-to-liquids processing,Gas-to-Liquids Processing Conference, San Antonio, TX. **1998,** March, 18–20.
(10) Production of oxygen by integrated ion transport membrane systems, Res. Discl. **1995**, 427–440, June.
(11) Alberty, R. A.; Silbey, R. J. *Physical Chemistry*, fifth edition, John ey & Sons, Inc. **1992**, New York.
(12) Chemical & Engineering News, **2004**, October 11, 39.

SYNTHESIS OF DIMETHYL CARBONATE FROM UREA AND METHANOL OVER ZINC OXIDE

Mouhua Wang[1, 2], Hui Wang[1,2], Ning Zhao[1], Wei Wei[1], Yuhan Sun[1]

1, State Key Laboratory of Coal Conversion, Institute of Coal Chemistry Chinese Academy of Sciences, Taiyuan, 030001 China.
2, Graduate School of the Chinese Academy of Sciences.

Introduction

The utilization of carbon dioxide has gained considerable attention for the point of view of "Sustainable Society" and "Green Chemistry" in recent years. Unfortunately, CO_2 is a thermodynamically stable molecule, which makes it difficult to be converted to useful chemicals directly [1]. The synthesis of dimethyl carbonate from urea which was synthesized from CO_2 and ammonia was considered to be a potential route for utilization of CO_2 to fine chemicals.

Dimethyl carbonate (DMC) is an environmentally friendly organic chemical. It can be used as methylating or carbonylating agent for substituting of toxic dimethyl sulfate, methyl halide and phosgene [2]. It is also believed to be an ideal fuel additive to enhance the octane number of gasoline [3].
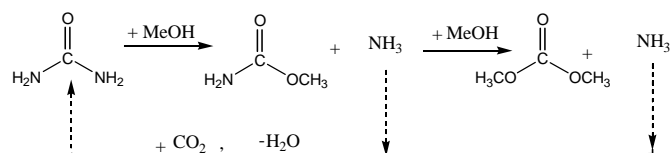
Scheme 1. Synthesis of DMC by urea methanolysis.

DMC was proposed to be synthesis from urea and methanol via two-step reaction as shown in scheme 1. The known catalysts for this method were organotin compounds and alkali metal compounds. Cho reported the using of alkali metal compounds or quaternary ammonium compound as catalyst, but the DMC yield was very low (<5%) [4]. Saleh obtained higher DMC yield and selectivity over dibutyl methoxy isocyanato tin catalyst [5]. High yield and selectivity of DMC was obtained by using dibutyl dimethoxy tin and high boiling electron donor compound (triglyme) as cocatalyst [6]. However, the preparation of these catalysts and the separation of the products was difficult. Thus, homogeneous catalysts should be disadvantageous to industrialization. In the present work, ZnO was used as an effective catalyst for this reaction and the catalytic mechanism was proposed.

Experimental

The reaction was carried out in a novel apparatus with a 250 ml stainless steel autoclave with magnetic stir and a reflux column by which ammonia could be removed easily. Methanol (4 mol) and urea (0.2 mol) as well as catalyst (1g ZnO and NaOH, 3 g $SnOBu_2$) were charged into the autoclave. The product was analyzed by GC. ZnO was prepared by calcinations of the zinc carbonate. The $SnOBu_2$ and NaOH were used as purchased.

FTIR spectra were recorded on a Nicolet Magna 550II Fourier-transform infrared spectrometer in the region 4000-400cm^{-1}. 128 scans with a resolution of 4cm^{-1} were collected. The samples of urea and urea loaded on ZnO was mixed with paraffin, then laid them on NaCl slice for scanning; self-supporting wafer was pressed at $2.5 \times 10^8 N \cdot m^{-2}$ with 15-20mg and mounted in an in-situ cell equipped with CaF_2 windows.

Results and Discussion

Table 1 shows the effect of catalyst on DMC yield from urea and methanol. It can be seen that, besides trace amount of DMC, methyl carbamate (MC) was the major product in the non-catalytic reaction (case 1). This indicated that the intermediate MC (see scheme 1) which was easily produced even in the absence of catalyst, could hardly be converted to DMC. These results were consistent with the experimental results in literature [7]. As listed in table 1, ZnO (case 2) showed higher activity for DMC synthesis than $SnOBu_2$ (case 4) and NaOH (case 5)which was used by Ryu's and Cho respectively. It should be noticed that, when MC instead of urea was used as the feed, the result was quite different (case 2, 3). ZnO only exhibited very low activity for DMC synthesis though the non-catalytic reaction afforded a high MC yield. It was concluded that the high activity of ZnO was related to urea.

The interactions of urea with ZnO were investigated by using FTIR. Fig.1 illustrated the FTIR spectra of urea and urea loaded on ZnO under room temperature. The C=O stretching vibration in spectrum (a) and (b) are 1666cm^{-1} and 1676 cm^{-1} respectively. The red shift of 10 cm^{-1} for C=O stretching vibration when urea was loaded on ZnO might suggest that ZnO acted on the oxygen lone pair to reduce the band energy of C=O. Fig 2 showed the FTIR spectra of urea loaded on ZnO at different temperature. The band at 1666 cm^{-1} diminished continuously with the increasing of temperature, and a new band at 2205 cm^{-1} with a shoulder at 2225 cm^{-1}, which were assigned to NCO species, appeared and increased simultaneously. The NCO species might promote the DMC synthesis from urea and methanol in the reaction. These results suggested that urea was activated by ZnO effectively.
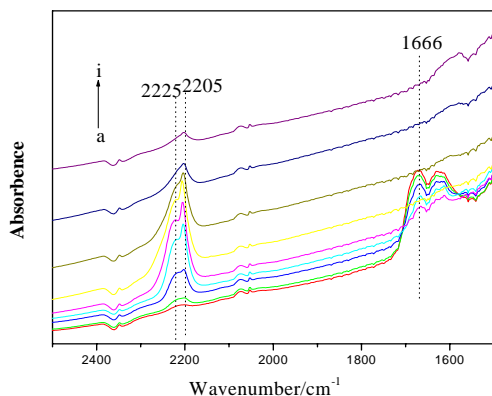
Table 1. Effect of catalyst on DMC yield.

Run	Catalyst	Reaction temperature /℃	Reaction time/h	MC,yield/ %	DMC yield/%
1	-	180	10	89	0.83
2	ZnO	170	8	48	29
3*	ZnO	170	8	-	1
4	$SnOBu_2$	170	8	73	12
5	NaOH	190	11	50	6

* Used methyl carbamate as the reactant replacing urea.
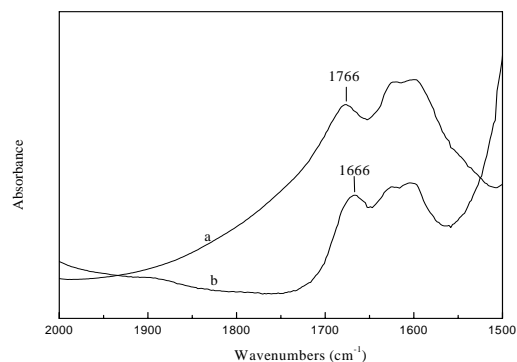
Figure 1. FTIR spectra of the urea and urea loaded on ZnO. (a) urea, (b) urea loaded on ZnO.

Figure 4. FTIR spectra of urea loaded on ZnO: a 50℃, b 75 ℃, c 100℃, d 125 ℃, e 150℃, f 200℃, g2 25 ℃, h 250℃, i 300℃

Conclusion

Dimethyl carbonate was synthesized from urea and methanol with a good yield over ZnO catalyst, so it was thought to be a potential process for conversion of CO_2 to valuable chemicals via urea. The present studies revealed that the high activity of ZnO was related to the activation of urea, and further investigation of the detailed mechanism of ZnO is now in progress.

References

1   Aresta, M. ACS Symposium Series, NO.852: *Utilization of Greenhouse gases*, **2003**，Chap 1, 2.
2   Ono, Y. *Appl. Catal. A- Ge*n., **1997**, 155, 133.
3   Pacheco, M. A.; Marshall, C. L. *Energy & Fuels*, **1997**,11,2.
4   Cho, Ts.; Tamura, T.; Cho, To; Suauki, K. US patent No. 5534649, **1996**
5   Saleh, R. Y.; Michaelson, R. C.; Suciu, E. N.; Kuhlmann, B. US patent No. 5565603, **1996**.
6   Ryu, J. Y.; Gelbein, A. P. US patent No. 6392078 B1, **2002**.
7   Ball, P.; Füllmann, H.; Schwalm, R.; Heitz, W. *C1 Mol. Chem.*, **1984**, 1, 95.

PRECURSORS OF THE FREE RADICALS GENERATED IN THE TAR AND GAS PHASES OF MAINSTREAM CIGARETTE SMOKE

Salem Chouchane[*], Narendra K. Meruva[*], Anthony P. Brown[†], and Jan B. Wooten[‡]

* Philip Morris USA Postgraduate Research Program,
† Lancaster Laboratories, c/o Philip Morris USA Research Center,
‡ Philip Morris USA Research Center,
4201 Commerce Road, Richmond, Virginia 23234, USA.

Introduction

Free radicals in cigarette smoke have been suggested to be responsible in part for the harmful effects of smoking.[1,2] Free radicals are present in both the tar and gas phase of cigarette smoke. The gas phase radicals, which are unstable, have been suggested to be continually formed by a steady state process where NO in the gas phase is oxidized to NO_2 which in turn oxidizes alkenes such as isoprene or butadiene to form alkyl radicals and ultimately peroxyl and alkoxyl radicals.[3] The tar radicals, which are very stable, have been reported to be hydroquinone/semiquinone/quinone in a polymeric matrix formed during the burning of polyphenolic compounds found in tobacco.[4] However another report suggests there is little correlation between cigarette smoke mainstream smoke particulate phase radicals and hydroquinone yield.[5]

In this study, primary emphasis was placed on investigating the possible precursors of free radicals in cigarette smoke. Formation of free radicals in both the gas and tar phases of cigarette smoke from different cigarettes was investigated using electron paramagnetic resonance (EPR) and EPR spin-trapping techniques. The yield of free radicals in the tar and the gas phases of smoke from different cigarettes was investigated. The yield of phenolic compounds (i.e. hydroquinone and catechol) in the tar and the amount of polyphenolic compounds (i.e. chlorogenic acid, quinic acid, cafeic acid, gentisic acid, rutin, and scopoletin) in tobacco were quantitatively determined. The possible precursors of nitric oxide in the tobacco, such as soluble ammonia and nitrates were also determined.

Experimental

Cigarette samples. Three different single component cigarettes containing only one type of tobacco each were chosen to be reasonably representative of the tobaccos used in current US commercial cigarettes products: flue cured Bright or Virginia tobacco; air cured Burley tobacco, and sun cured Oriental (also known as Turkish tobacco). Two reference cigarettes were also used: 2R4F, a low tar reference cigarette (University of Kentucky Tobacco and Health research Institute, 2003) and IM17, an industry monitor cigarette manufactured by Philip Morris USA Inc. The filler of these references represents a typical American-blend cigarette comprising of Bright, Burley and Oriental tobaccos. 2R4F and IM17 have exactly the same blend composition, and differ only in the cigarette construction. 2R4F is ventilated cigarette while IM17 is not.

Cigarettes smoking procedure. Typically, 1 cigarette was smoked on 1-port automatic smoking machines under the FTC smoking conditions (35 ml puff volume, 2 second puff duration, 60 second puff interval, 8 puffs per cigarette, and sine puff profile). The gas phase was separated from the tar by placing a cellulose filter (Osmonic Inc.) supported by a Cambridge pad between the smoking machine and the smoked cigarette. In general, three replicate smoke samples were generated per cigarette type. The gas phase and the tar were analyzed as described below.

Polyphenolics analysis in tobacco (LC/MS/MS). The major polyphenolic compounds analyzed in tobacco were quinic acid, chlorogenic acid, caffeic acid, gentisic acid, rutin and scopoletin. The tobacco filler was extracted using 50% (v/v) aqueous acetone for 24 hours at room temperature. The LC/MS/MS analysis were carried out using an Agilent Technologies 1100 series HPLC system (Palo Alto, CA, USA) interfaced with a tandem quadrupole mass spectrometer (Quattro *Ultima*™) detector from Micromass ® (Beverly, MA, USA). Chromatographic separations were performed on a C18 LC column from Waters Corporation (Milford, MA).

Phenolic analysis in tar of cigarette smoke (GC/MS). The phenolic compounds in the tar of cigarette smoke were analyzed by GC/MS. Briefly, the tar collected on the cellulose filter was extracted with 5.0 ml of acetonitrile overnight, derivatized with a silylating agent (BSTFA) containing 10% TMCS. The analysis was performed by GC/MS on an Agilent 6890 GC equipped with an Agilent 5973 quadrupole MSD analyzer using Selected Ion Mode for qualitative and quantitative analysis.

Sources of nitrogen in tobacco. The source of nitrogen in tobacco was determined by analyzing the total nitrogen, soluble ammonia and nitrates in the tobacco filler of the different cigarettes. The analyses were carried out by standard analytical methods.

EPR analysis of tar of cigarette smoke. The cellulose filter containing the tar was introduced into an EPR tube and the spectra were acquired using a Bruker EMX EPR spectrometer (Bruker Instruments, Billerica MA), X-band, 100 kHz. The following EPR parameters were used: Microwave power 2 mW; modulation amplitude 2 G; time constant 5.12 ms; conversion time 5.12 ms; number of scan 60. The concentration of free radical was determined by double integrating the EPR signal using WinEPR software and comparing with known concentration of 2,2-diphenyl-1-picrylhydrazyl (DPPH).

EPR analysis of gas phase of cigarette smoke. The cigarette smoke that was filtered by the cellulose filter was bubbled into 4 mL of the spin-trapping solution containing 100 mM N-*tert*-butyl-α-phenylnitrone (PBN) in benzene. The solution was then degassed using nitrogen gas for 5 min and then injected an AquaX cell (Bruker Instruments, Billerica MA) mounted on a Bruker high sensitivity EPR cavity and spectra were acquired using the same instrument described above. The following EPR parameters were used: Microwave power 20 mW; modulation amplitude 05 G; time constant 20.48 ms; conversion time 20.48 ms; number of scan 20. The concentration of free radical was determined by double integrating the EPR signal using WinEPR software and comparing with known concentration of 4-hydroxy-2,2,6,6-tertramethyl-piperdinooxy free radical (TEMPOL).

Results and discussion

The amount of polyphenolic compounds varied among blend type. Bright tobacco cigarettes yielded the greatest amount of polyphenolic compounds and burley the lowest (Figure 1).
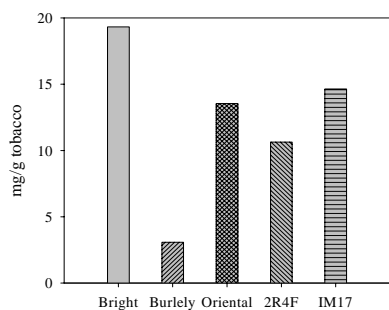
Figure 1. Total polyphenolic compounds found in the different types of cigarettes used.

The yield of radicals from these cigarettes did not correlate with the trend in polyphenolic compounds. Oriental cigarettes produced the highest yield of free radicals (Figure 2).
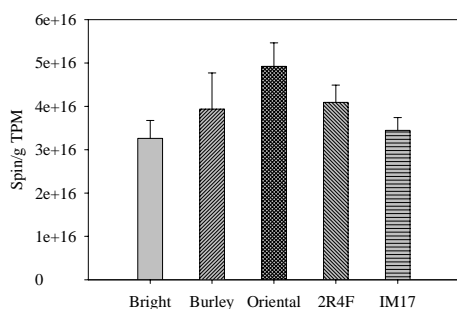
**Figure 2.** Free radical yield in the tar of cigarette smoke.

The analysis of the cigarette smoke tar by GC/MS showed the presence of several phenolic compounds. Monohydroxybenzenes such as phenol and cresol, and dihydroxybenzenes such as hydroquinone and catechol were all observed in cigarette tar. Hydroquinone and catechol were the most abundant phenolics found in the tar of cigarette smoke. Bright cigarette showed the highest yield of phenolic compounds in the tar (data not shown). A similar trend in the yield of tar radicals was observed when compared to the yield of the dihydroxybenzenes (compare Figure 2 to Figure 3), except for Bright cigarette.
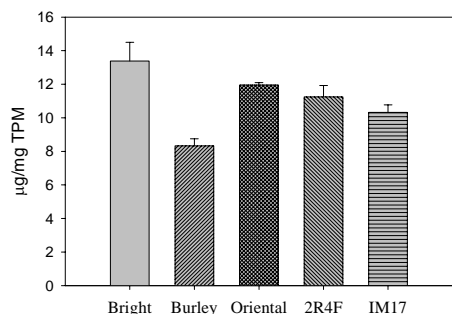
Figure 3. Yield of dihydroxybenzenes in the tar of cigarette smoke.

Burley tobacco presented the highest content of total nitrogen, soluble ammonia and nitrate, while Bright exhibited the lowest content (Figure 4). The analysis of the gas phase radicals by the EPR

spin trap technique showed that the smoked cigarette yielded significantly different amount of radicals. The yield of radicals
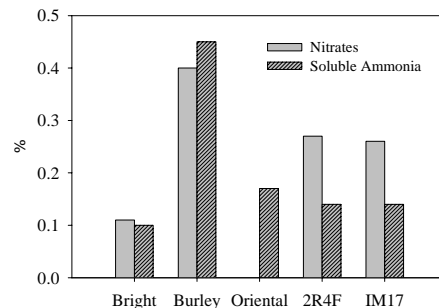
Figure 4. Nitrates and soluble ammonia contents of cigarette.

generated by the Burley cigarette was significantly higher than that of Oriental and Bright cigarettes (Figure 5), and the trend was similar to the yield of soluble ammonia in the filler of these cigarette. There was no good correlation for the reference cigarette.
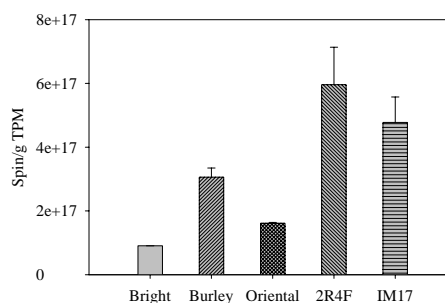
Figure 5. Yield of free radicals in the gas phase of cigarette smoke.

Although polyphenolic compounds or precursors might be involved in the radical formation, the data reported in this work indicates that there is no correlation between the polyphenolic content of the tobacco and the yield of radicals formed in the tar. Other unidentified polyphenolic compounds or precursors, however, might be involved in the radical formation. A correlation was observed between tar radical yield and dihydroxybenzenes yield in the tar, suggesting that phenolic compounds such as hydroquinone or catechol might be responsible for the radicals formed in the cigarette smoke tar. However, they still cannot account for all the radicals found in the tar of cigarette smoke. A similar trend (Burley>Oriental>Bright) was found between the yield of the free radicals in gas phase of cigarette smoke and the amount of soluble ammonia in the tobacco filler. Soluble ammonia is a possible precursor of nitric oxide in the gas phase of cigarette smoke. A cigarette with higher soluble ammonia content will generate more nitric oxide in the gas phase and ultimately more free radical through the oxidation of NO to NO_2 and subsequent reactions with unsaturated molecules such as alkenes in the smoke.

References
(1) Church D. F., and Pryor W. A., In "*Lung injury*". Ed. Crystal R. G., and West J. B., Raven press, New York, **1992**, pp 215-219.
(2) Church D. F., and Pryor W. A., *Environmental Health Perspectives*, **1985**, 64:111-126.
(3) Pryor W.A., Prier D. G., and Church D. F., *Environmental Health Perspectives*, **1983**, 47, 345-355.
(4) W. A. Pryor, Hales B. J., Premovic P. I. and Church D. F., *Science*, **1983**, 220, 425-427.
(5) Blakley R. L., Henry D. D, and Smith C. J., *Food and Chemical. Toxicology*, **2001**, 39:401-406

SYNTHESIS OF ETHYLENE CARBONATE FROM UREA AND ETHYLENE GLYCOL OVER SOLID ACID-BASE CATALYSTS

Qibiao Li[1, 2], Ning Zhao[1], Wei Wei[1], Yuhan Sun[1]*

[1]State Key Laboratory of Coal Conversion, Institute of Coal Chemistry, Chinese Academy of Sciences, Taiyuan, 030001 P. R. China; [2]Graduate School of the Chinese Academy of Sciences.
*yhsun@sxicc.ac.cn, Fax: +86-351-4041153; Tel: +86-351-405380

Introduction

As a good organic solvent with high boil point, Ethylene carbonate (EC) is widely used in many field for petroleum distillation extraction, spin dye printing, processing agent for synthetic fibers, lithium batteries electrolyte components and gas separation, etc. It can also be used as intermediate in pharmaceutical and polymer synthesis, and as feed for synthesis of dimethyl carbonate (DMC) via transesterification with methanol. Various methods are known for producing EC [1, 2]. However, these routes are suffered from hazards of poisonous or a lack of economical viability. Nowadays, EC was synthesized by cycloaddition of CO_2 and ethylene oxide in the industrial process [3]. Recently, a novel process for EC synthesis from urea and ethylene glycol (EG) was reported which attracts much attention because of many advantages compared to the traditional process: cheap and easily available raw material, mild reaction conditions, safe operations and higher EC yield. For the process of synthesis DMC via transesterification of EC with methanol, the byproduct ethylene glycol (EG) can be reconverted into the raw material EC by reacted with urea which would increase the efficiency of utilization of the raw material and greatly lower the cost of the production of DMC. The reaction of urea with EG is first reported in patent [4] by Su, et al. under atmospheric pressure in the presence of a catalyst comprising a tin-containing compound. However, the decomposition of urea is severely. Doya et al [5] increased the yield of EC by using zinc, magnesium and lead, or their compounds as catalysts under evacuation condition. Peter Ball [6] investigated the primary and secondary alcohols reacted with urea to form carbonate and found that the reaction proceeds in two steps, the first step formed carbamic ester is fast, and the rate of the second step remained much lower than that of the first. Moreover, combination of a weak Lewis acid and a Lewis base accelerated carbonate formation. The detail study about the synthesis EC from urea and EG is not appearance in the

open literature, the major aim of the present work is to discuss reaction mechanism via the effect of reaction condition and catalysts.

Materials and Methods

The synthesis of EC was carried out as follows: EG, urea and catalyst were charged into a 250-ml three-necked-flask, which armed with a stirrer, recycles reflux condenser equipped with gas-liquid separators and thermometer, heated to the reaction temperature at a reduced pressure. When reaction finished the products was analyzed by gas chromatograph (GC) equipped with flame ionization detector, capillary columnniation HP-5 after centrifugal separation from the catalyst. The identification of products was performed by GC-MS technique. CaO were prepared by decomposition of calcium carbonate at 850 for 3h, other catalysts were commercially available reagents pretreated at 500 for 3 h.

Results and Discussion

Based on the formed major products, the reaction pathways were deduced as following:
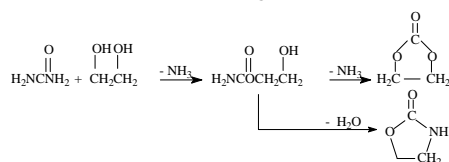
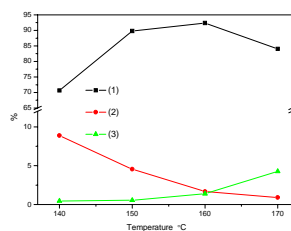
Effect of reaction time on synthesis of EC
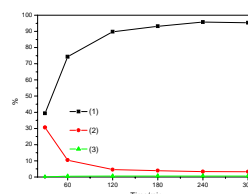
Figure 1. Effect of reaction time on synthesis of EC. (1) yield of EC, (2) yield of 2-hydroxyethyl carbamate (HEC), (3) yield of 2-oxazolidone (OZD). Remark: The yield of products based on the conversion of urea. Reaction temperature 150 at a Reduced pressure 11Kpa.Catalyst: Zinc oxide, the weight ratio of catalyst/urea is 3:100.The molar ratio of EG/urea is 1.5:1.

The results of investigation reaction time on synthesis of EC are shown in Fig.1.The yield of EC increase with the reaction time, while the yield of 2-hydroxyethyl carbamate (HEC) decreases. These results lead us to conclusion that HEC is the intermediate for the EC production form urea, and the reaction proceeds in two steps, the first step is formed HEC by EG reacted with urea, the second step is formed EC by HEC de-ammonia gas

reaction. Fig.1.indicated that before reaction run 2hours the yield of HEC decreased sharply while the yield of EC increased sharply, then both of them changed gently in finally. So we deduced that the rate of reaction of first step is much faster than that of the second. The second step form HEC to EC is a determinative process for the synthesis of EC. During the reaction process a little 2-oxazolidone (OZD) was produced by the HEC dehydration reaction.

Effect of reaction temperature on synthesis of EC

Figure 2. Effect of reaction temperature on synthesis of EC. (1) yield of EC, (2) yield of 2-hydroxyethyl carbamate (HEC), (3) yield of 2-oxazolidone (OZD). Remark: The yield of products based on the conversion of urea. Reaction time 3h.Reduced pressure from140 to 170 respectively at 8 Kpa, 11Kpa, 18Kpa, 26Kpa.Catalyst: Zinc oxide, the weight ratio of catalyst/urea is 3:100.The molar ratio of EG/urea is 1.5:1.

The results of investigation reaction temperature on synthesis of EC are shown in Fig.2 Yield of EC increased with the increase of temperature then decreased at 170 , the yield of HEC decreased and the yield of OZD increased with the increase of temperature. It can be conclude that increasing temperature are profited for the production of EC, especially are availed to HEC convert to EC, the most unfavorable factors is promoted HEC dehydration reaction. Lead to urea decomposes and the conversion of urea decrease.

Effect of catalysts on the synthesis of EC

Table 1. Results of urea reacted with EG

| Catalysts	EC Yield (%)	HEC Yield (%)	OZD Yield (%)
---	32.30	36.82	0
CaO	65.74	0.94	13.21
La$_2$O$_3$	72.03	7.5	8.1
MgO	84.45	4.41	5.18
ZnO	93.12	3.91	0.61
Al$_2$O$_3$	28.67	42.53	0
SiO$_2$	30.2	36.49	0

The yield of products based on the conversion of urea. Reaction temperature: 150 at a reduced pressure 11Kpa.Reaction time: 3h.

the weight ratio of catalyst/urea is 3:100.The molar ratio of EG/urea is 1.5:1.

The effect of catalyst on synthesis of EC are shown in Table 1.It is found that The catalysts with alkaline such as CaO, La$_2$O$_3$, MgO, ZnO the base strength is gradually decreasing [8] and the activity of catalyst for the synthesis of EC is gradually increasing. The yield of OZD gradually increases with the base strength boosting up. It can be indicated the strong base catalyst easily made HEC dehydration reaction to form OZD, especially the catalyst performance of CaO is very obviously. Compared the HEC dehydration reaction with the HEC de-ammonia gas reaction, that formed a parallel competitive reaction. In contrast to the no-catalytic reaction, the catalysts with acidity such as Al$_2$O$_3$, SiO$_2$ almost have not any catalytic activity, to some extent restrained the formation of EC. ZnO and MgO represented very superior catalytic activity in the reaction. Both ZnO and MgO have acidic and basic properties at surface [9, 10]. We suggest that the catalysts with appropriate acidity and basicity play an important role for the synthesis of EC.

Reaction mechanism of synthesis EC

Based on the formed products and the influencing results of reaction condition and catalysts, the following possible reaction mechanism was suggested:
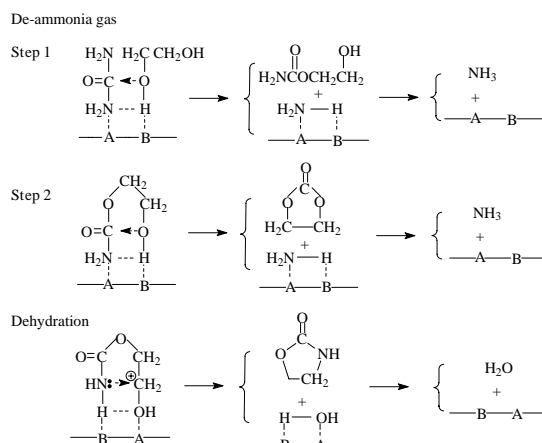
The reaction of urea with ethylene glycol via Lewis acid and Lewis base coordinated catalyze to form ethylene carbonate. When increasing the base strength dehydration reaction of 2-hydroxyethyl carbamate is promoted.

Conclusions

A novel route which is environmentally benign, efficient and available green chemical methods for synthesis of EC via the reaction between EG and urea was presented in this work. The reaction pathway is proceeded in two steps, the second step is determination step, which was deeply affected by the reaction

temperature and the performance of catalyst. Based on the experiments, a Lewis acid and Lewis base synergistic catalyze mechanism for the reaction was postulated.

References

1. M. Aresta, E. Quaranta, Chem. Tech. **1997**,27, 32.
2. M. Aresta, A. Dibenedetto, I. Tommasi, Appl. Organometal. Chem. **2000**,14 ,799.
3. D.J. Darensbourg. M.W. Holtcamp, Chem. Rev. **1996**,153, 155.
4. Su, et al US patent No. 5003084 (1991).
5. Doya, et al US patent No. 5440004 (1995).
6. Peter Ball, Heinz Fullmann, Walter Heitz Angew.Chem.Int.Engl. **1980**,19,,9
7. Bhanage, S. Fujita, Y. Ikushima and M. Arai, *Appl. Catal. A*, **2001**, 219, 259
8. Fei Jinhua , et al. Journal of Fuel Chemistry and Technology，**1994**, l22, 1
9. W.F.Holderich *Appl. Catal. A: Gen.* **1999**,257,184

AN INDUSTRIAL CR-FREE IRON-BASED CATALYST (NBC-1) FOR HIGH-TEMPERATURE WATER GAS SHIFT REACTION

Quangsheng Liu , Wenping Ma,[*] Zhanjun Mou, Qiancheng Zhang

Department of Chemical Engineering, Inner Mongolia Polytechnic University, Hohhot, P. R. China, 010062

Introduction

Iron-chromium oxide catalysts have been used industrially for the water gas shift reaction (WGS, $CO + H_2O = CO_2 + H_2$, $\Delta H_{298} = -40.6$ kJ/mol) at the high temperature range of 320-480 ^{o}C. This type of catalyst demonstrated high WGS activity and excellent stability due to Cr acting as a structural stabilizer[1] and/or a structure promoter.[2] However, it has been found that Fe based industrial WGS catalysts with 8-14% Cr generally contain ~2 wt.% of Cr^{6+}, which is highly toxic to humans and environment during their manufacture and deposition. Therefore study of Cr-free iron based WGS catalysts became a very interesting topic in recent years.

Previous studies on this issue focused on replacing Cr by various metal oxide promoters such as Al_2O_3, MnO_2, PbO, La_2O_3, CaO, ZrO_2, and etc.[3,4,10] However, these attempts to create industrial Cr-free iron based WGS catalysts have proven to be unsuccessful due to catalysts either lacking desired activity and selectivity or thermo-stability. Recent studies showed that CeO_2 was a very good choice as a promoter for high temperature WGS catalysts.[5,6] It has been reported that addition of CeO_2 to Fe-Cr and Cr-free Fe based WGS catalysts could improve catalyst performance.

Researchers at Inner Mongolia Polytechnic University (IMPU) have studied Cr-free Fe based WGS catalysts for many years.[7-9] An industrial CeO_2-Al_2O_3 promoted Cr-free Fe based catalyst, NBC-1, was invented using proper preparation procedures.[8,9] The present paper reports physical and catalytic properties of the NBC-1 catalyst. The adsorption/desorption behaviors and surface reaction of reactant species such as H_2O, CO and CO_2 were studied through Temperature Programmed Desorption (TPD), and Temperature Programmed Surface Reaction (TPSR) for the purpose of understanding the WGS mechanism on the NBC-1 catalyst.

Experimental

Catalyst Synthesis. The commercial NBC-1 catalyst was prepared using the co-precipitation technique. Details of preparation procedures were reported previously.[8,9] In brief, the NBC-1 was precipitated with industrial iron sulfite and ammonia solutions in an industrial precipitation vessel (D = 1450 mm and H = 1850 mm). Before precipitation, iron sulfite solution in the vessel was partly oxidized by air to get the desired amount of Fe^{3+} cations (Fe^{2+}/ Fe^{3+} ~ 2.0). Promoters of Al_2O_3 and CeO_2 (in powder form) were added during precipitation. The resulting slurry was subsequently aged followed by washing, drying and calcination.

Fixed-Bed Reactor Test. The activity of NBC-1 catalyst (12-14 mesh, ~2 g) was examined in a bench-scale fixed-bed stainless steel

[*] Present address: Department of Chemical Engineering, West Virginia University, Morgantown, WV. 26505

reactor (ID = 10 mm) under atmospheric pressure, 350 ^{o}C and 3000 h^{-1} (dry-gas basis). The composition of feed gas was 26% CO, 8% CO_2, 40% H_2 and 26% N_2 (internal standard). Prior to WGS reaction, NBC-1 catalyst was reduced using the same reactant gas mixture under severe conditions: 530 ^{o}C, 3000 h^{-1} for 15 h. The gas compositions before and after the WGS reaction were analyzed online by a GC-8A gas chromatograph (GC).

Characterization Methods. The BET surface areas of the catalysts were measured by isothermal adsorption of N_2 at 77K using a surface area porosity analyzer ASAP2010. The desorption behaviors of H_2O, CO_2 or CO species and their surface reaction property on the catalyst surface were characterized by the TPD and TPSR using a Micrometrics Autochem 2910 instrument.

Results and Discussion

Table 1 lists the bulk composition, BET surface areas before and after WGS reaction and CO conversion (X_{CO}, %) at 350 ^{o}C of the NBC-1 catalyst. The same experimental data of a commercial Fe-Cr WGS catalyst denoted as C12-4, which was supplied by United Catalyst Inc. (UCI), are also listed in Table 1 for comparison. The NBC-1 contains higher amount of Fe_2O_3 than the C12-4 (88.8% *vs.* 81.2%) The BET surface areas of both catalysts before reaction are nearly the same (70-73 m^2/g). After WGS reaction, the BET surface areas of NBC-1 and C12-4 catalysts were decreased to 35.2 m^2/g and 40.4 m^2/g, respectively. Hence the BET surface area of NBC-1 catalyst after reaction is lower than that of C12-4 catalyst by 12.9%. CO conversions at 350 ^{o}C during steady state for both catalysts are high and nearly the same (53-54%), which was not quantitatively correlated well with their surface areas. Due to the NBC-1 and C12-4 catalysts experiencing very severe thermo-resistance test during reduction period (530 ^{o}C and 15 hours), the high CO conversions showed that both catalysts had excellent thermo-resistance property.

Table 1. Summary of BET and Reaction Results of NBC-1 and C12-4 Catalysts

Catalyst ID	Catalyst weight composition [a]	BET surface area, m^2/g		X_{CO},% [b, c]
		Before reaction	After reaction	
NBC-1	88.6% Fe_2O_3/2.0% Al_2O_3/0.5% CeO_2	72.8	35.2	53.0
C12-4	81.2% Fe_2O_3/8.8% Cr_2O_3	70.3	40.4	53.8

(a) Balanced by graphite and water

(b) X_{CO}, % = (CO mole flow rate in - CO mole flow rate out)/ CO mole flow rate in × 100

(c) Reaction conditions: 350 ℃, 1 atm, H_2O: gas=1:1 and 3000 h^{-1} (dry-gas basis).

The H_2O, CO_2 or CO TPD profiles for the NBC-1 catalyst were illustrated in Figures 1a-c. Two H_2O desorption peaks appear in the H_2O TPD profile (Figure 1a). The first big peak located between 300 and 470 K is assigned to desorption of physisorbed water on the catalyst, whereas the second peak occurred between 470 and 673 K is ascribed to the desorption of chem-adsorbed water on the NBC-1 surface, which might reflect some information of water desorption behavior at real reaction conditions. It is interesting that a huge CO_2 desorption peak was found between 300 and 570 K (Figure 1b). This indicates that the NBC-1 catalyst has high CO_2 adsorption ability at room temperature, but adsorbed CO_2 can be desorbed completely from the catalyst surface at about 570 K. There is one smaller CO desorption peak (Figure 1c). It can be seen that the maximum CO

desorption signal occurs at around 373 K, and no more CO can be detected beyond 500 K.

According to these findings, we may describe the H_2O, CO and CO_2 desorption behaviors on the NBC-1 catalyst at real WGS temperature of 350 °C. It was impossible that adsorbed CO was on the catalyst surface at 350 °C because CO desorption signal at this temperature in the CO TPD profile is close to nothing. In this case, CO must be in gas phase to participate the WGS reaction. A part of H_2O might be in adsorbed state on the catalyst surface at 350 °C because H_2O was desorbed completely after 500 °C (773 K). Generally, the WGS reaction can be interpreted by the two prevailing WGS reaction mechanism models, i.e. redox regenerative model and associative model.[1,10] In the associative model, it is assumed that CO_2 and H_2 were formed through formate species from adsorbed CO and H_2O. In redox regenerative model, it is assumed that the catalyst surface is oxidized and reduced by CO and H_2O, and CO_2 can be produced through CO reacting with an O site. Therefore, it is quite possible that the WGS reaction on the NBC-1 catalyst proceeded via the redox regenerative mechanism, which is consistent with studies on iron based WGS catalysts.[10,11] Further, CO_2 was desorbed easily below 570 K (Figure 1b), which is not consistent with the slow CO_2 formation step through the associative mechanism, and this is also indicative of the redox regenerative mechanism taking place on the NBC-1 catalyst surface at real reaction conditions.
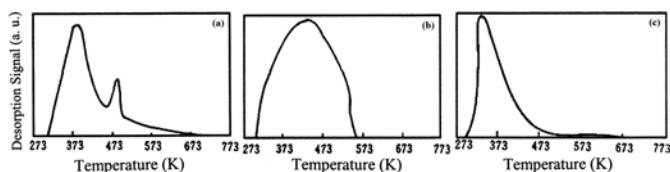

Figure 1. TPD profiles of H_2O (a), CO_2 (b) and CO (c) on the NBC-1 catalyst.

The reduced NBC-1 catalyst adsorbed H_2O at room temperature for 1 hours, and then the H_2O + CO TPSR was carried out by flowing gas mixture of 5%CO/N_2 when the catalyst bed temperature was increased from room temperature to 773 K at 3 K/min. H_2 effluent was monitored by a GC with a TCD. Figure 2 shows the result of H_2O + CO TPSR on the NBC-1 catalyst.

Clearly, the surface reaction between adsorbed H_2O and CO was initiated at 513 K according to the H_2 signal at this temperature (Figure 2). H_2 amount continued to increase with increasing temperature and reached maximum at about 573 K. After that the H_2 curve went down up to the temperature of 773 K. It is believed that some adsorbed H_2O still existed on the catalyst surface at 513 K. With increasing temperature, two possible reactions took place for the adsorbed H_2O remained on the catalyst surface. One possibility was that adsorbed H_2O was desorbed from the catalyst surface (H_2O-s = H_2O + s, where s represents a vacant site) as temperatures increasing and became a gas reactant. This is consistent with the above discussion in light of Figure 1a. Another possibility was that remaining adsorbed H_2O oxidized active metal site and H_2 was released simultaneously (H_2O-s + M = H_2 + O-s-M, where M represents active metal site). It might be that the rate of oxidation reaction of the adsorbed H_2O increased with temperature between 513 and 573 K, which resulted in the increased H_2 signal with temperature. It is not surprising that H_2 amount was decreased after

573 K, because most of water has been desorbed before 573 K and no enough adsorbed H_2O took part in the oxidization reaction. Thus the H_2O + CO TPSR experimental result also reflects that the WGS reaction on the catalyst may take place through the redox mechanism.
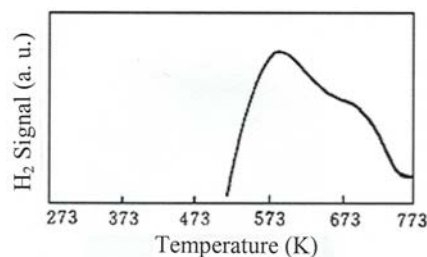
Figure 2. H_2O + CO TPSR profile on the NBC-1 catalyst.

Concluding Remarks

The NBC-1 is an excellent Cr-free iron based catalyst high-temperature WGS catalyst. Its activity is high and comparable to the commercial C12-4 Fe-Cr catalyst. Thermo-stability of the NBC-1 is excellent too. It is a good alternative to the traditional high-temperature Fe-Cr WGS catalysts.

The H_2O, CO and CO_2 TPD and H_2O + CO TPSR studies provided evidence of the WGS reaction proceeding through the redox regenerative mechanism on the NBC-1 catalyst surface under real reaction condition. This fundamental knowledge makes it possible to study kinetic model of WGS on the NBC-1 catalyst in future.

References
(1) Newsome, D.S. *Catal. Rev. Sci. Eng.,* **1980**, 21, 275.
(2) Mars, P. *Chem. Eng. Sci.,* **1961**, 14, 375.
(3) Chinchen, G.C. *Euro Patent* A-0 062410, **1982**.
(4) Shirokov, Y.G. *Khim. Khim. Tekhnol,* **1978**, 21, 1339.
(5) Ladebeck, J.; Kochloefl, K. *Stud. Surf. Sci. Catal.,* **1995**, 91 (5), 1079.
(6) Hu, Y.; Jin, H.; Hao, D. *Chem. Eng. Japan,* **2000**, 78, 147.
(7) Ma. W.P. *M.S. Dissertation (Preparation of Cr-Free iron based catalysts for the water gas shift reaction), Inner Mongolia Polytechnic University, Hohhot, China.* **1995**.
(8) Jin, H.F.; Liu, Q.S.; Mou, Z.J. et al. *Chinese Paten,* CN 1133754, **1996**.
(9) Jin, H.F.; Liu, Q.S.; Mou, Z.J. *Chinese Patent,* ZL95 121834.4, **1999**.
(10) Rethwisch, D.G.; Dumesic, J.A. *Appl. Catal.* **1986**, 21, 97.
(11) Chinchen, G.C.; Spencer, M.S.; Waugh, K.C.; et al. J. Chem. Soc. Faraday Trans. **1987**, 183, 2193.

STUDY ON TEMPERATURE FIELD DISTRIUTION IN A TURBULENT CONTACT ABSORBER

Manyin Hu[1], Hezhong Tian[2], Zhong Liu[1], Shuo Zhang[1], Lifeng Li[1]

1. School of Environmental Science and Engineering, North China Electric Power University, Baoding 071003, China
2. Department of Environmental Science and Engineering, Tsinghua University, Beijing 100084, China

Introduction

With the rapid economic growth and industry expansion, sulfur dioxide (SO_2) emissions and acid deposition has become one of important factors influencing sustainable development in China. In 2003, the total SO_2 emissions in China reached as high as 21.59Mt, and the areas suffering acid rains accounted for over 1/3 of whole country territories[1]. Therefore, it is of great significance to develop and apply desuphurization installations to control SO_2 emissions and pollution.

By now, many types of flue gas disposal process and devices have been developed and exploited throughout the world. Among which, the Turbulent Contact Absorber (TCA) can achieve desulphurization and dust removal simultaneously in one tower. TCA has such features and merits as follows:

(1) Treated Flue gas rate can be very high. It could maintain stable manipulation even when the flue gas flux fluctuated largely.

(2) Desulphurization efficiency can be as high as above 90%, and dust removal efficiency was comparatively higher.

(3) The TCA tower was not apt to be blocked when the flue gas contained some dust and reaction resultant contained solid materials.

(4) The phenomena of deviate current flow can be avoided.

In addition, the capital cost of TCA was relatively low, and its operation and maintenance was simple. So, TCA could be used for all kinds of flue gas desulphurization and dust removal in China.

In this paper, temperature field distribution in a TCA tower was investigated through numerical simulation and calculation, which were based on a self-made TCA tower. It will be helpful for the research of chemical reaction dynamics and design and operation of a TCA tower in reality.

Methodologies and Mathematical models

TCA introduction. TCA is a counter three phases fluidized bed in which the gas phase acts as a sequence phase. The schematic drawing of a TCA tower was shown in **Figure 1**. Many stuffing balls were filled between the two fences, most commonly are hollow balls which are made of polyethylene or polypropylene, or polyethylene foam balls whose density is 100~400 kg/m³, diameter is 10~38mm.The section area of below fence is commonly above 70%, which facilitates gravity release. The interval of up and bottom fences is usually three times of the length of ball bed layer when is at static.

Flue gas enters TCA through inlet pipeline, the stuffing ball is at even and flow state, reagent sprays from top to bottom with equality velocity, the surface of small ball is wetted and absorbs SO_2.The surface liquid membrane of a small ball is renewed incessantly owing to the intensive interaction among gas, liquid, and solid phase, thus the contact and mass transfer between gas and liquid phase is enhanced, desulphurization and dust removal efficiency is improved. At last, the clean flue gas is discharged through a mist eliminator.

Basis equation. The temperature field in a TCA tower was considered as a steady problem, and the rate of each round section of the calculation field was in axis symmetry distribution. Thus, temperature distribution was regarded as in axis symmetry [2]. The energy equation based on symmetry reference frame of column axis.

$$\frac{\partial}{\partial x}(\rho u C_p T) + \frac{1}{\gamma}\frac{\partial}{\partial \gamma}(r\rho v C_p T) = \frac{\partial}{\partial \chi}(k\frac{\partial T}{\partial \chi}) + \frac{1}{\gamma}\frac{\partial}{\partial \gamma}(\gamma k\frac{\partial T}{\partial \gamma}) + S \quad (1)$$

where T--temperature, u、v--flue gas rate of axis and radial direction, respectively, k--heat transfer coefficient, c_p--specific heat at fixed pressure, S--source terms.
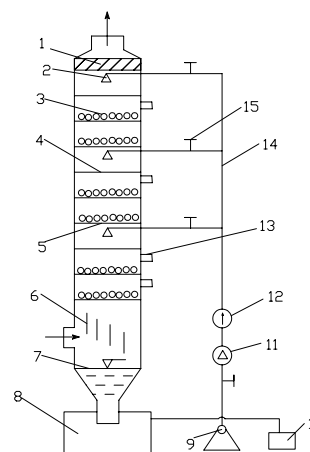
1--mist eliminator, 2—spray nozzle, 3--stuffing balls, 4--upper fence, 5--lower fence, 6--commute board, 7--liquid surface, 8--overflow slot, 9—pump, 10--slurry tank, 11—flow meter, 12--pressure meter, 13--test hole, 14--entering liquid tube, 15--flux regulate valve.
Figure 1. Schematic map of a TCA tower

Difference equations. The successive iterations approach was adopted to disperse the field of calculation, the control volume method was adopted to establish difference equation, the disperse equation of formula (1) can be expressed as follows:

$$a_p T_P = a_E T_E + a_w T_W + a_N T_N + a_S T_S + b \quad (2)$$
$$a_E = D_e A(|P_e|) + [|-F_e, 0|] \quad (3)$$
$$a_w = D_W A(|P_W|) + [(F_W, 0|)] \quad (4)$$
$$a_N = D_n A(|P_n|) + [|-F_n, 0|] \quad (5)$$
$$a_s = D_S A(|P_S|) + [|F_S, 0|] \quad (6)$$
$$b = s_c \Delta v \quad (7)$$
$$a_p = a_E + a_w + a_N + a_S - s_p \Delta v \quad (8)$$

Where: source terms were linearized $s = s_c + s_p T_p$; as to even grid, $\Delta v = r\Delta r\Delta x$; a_E, a_w, a_N, a_S were viewed as coefficients of each node adjacent to P, representing the influences of four control volumes on heat transfer and convection heat transfer; F, D, P denoted the intensity of convection heat transfer and heat transfer, and Berkeleian's number of column respectively; $A(|P|)$ was the function of Berkeleian's number of column, the math expression was related with difference format. The program of power function was adopted in the calculation, thus:

$$A(|P|) = [|0, (1-0.5|P|)^5|] \quad (9)$$

Boundary conditions. The boundary condition of inlet was viewed as the first category, which meant inlet flue gas temperature was known.

The boundary condition of wall surface was also viewed as the first category, and the vicinal area of the wall surface was confirmed according to wall surface function methods.

The variety rate of each parameter in outflow direction was defined as zero by the boundary condition of outlet.

The variety rate of each variable in plumbing axis direction was defined as zero on the symmetry axis.

The influence of stuff balls and fences and nozzles on temperature field were neglected in calculation.

Source terms. Source terms in calculation include liquid water decalescence s_1 when the temperature increased, heat of variety phase

s_2, and chemistry reaction heat s_3, were all included in source terms in calculation:

$$s_1 = -1355.28(T_g - T_s)M_s \qquad (10)$$

Where: T_g--flue gas temperature, T_s--slurry temperature, M_s--slurry spraying rate.

$$s_2 = [-2256 + 751(T_g - T_s)](M''_{H_2O(g)} - M'_{H_2O(g)}) \qquad (11)$$

Where: M''_{H_2O} was the quality flux of water moisture contained in outlet flue gas, kg/s, which was confirmed by the below expression:

$$M''_{H_2O(g)} = P''_{H_2O(g)}Q''\rho''_{H_2O(g)} /(3600P) \qquad (12)$$

Where: $P''_{H_2O(g)}$ --saturation vapor partial pressure of outlet flue gas, P-- local atmospheric pressure, Q'' --outlet flue gas flux, ρ''_{H_2O} -- saturation vapor density in outlet flue gas; M'_{H_2O} was the quality flux of water contained in inlet, kg/s, it was confirmed by the below expression:

$$M'_{H_2O} = X_{H_2O}Q'\rho'_{H_2O(g)} / 3600 \qquad (13)$$

Where: Q' --inlet flue gas flux, m^3/h, ρ'_{H_2O} --saturation vapor density in inlet flue gas, kg/m^3, X_{H2O}--inlet flue gas water contained, %.

$$s_3 = 2437\rho_{so_2}\eta Q' C_{SO_2} / 3600 \qquad (14)$$

Where: ρ_{so_2}--SO$_2$ density kg/m^3, c_{SO_2} --volume concentration of inlet flue gas, %, η--desulphurization efficiency.

Thus the source term s was expressed as follow:

$$s = (s_1 + s_2 + s_3)/(\frac{\pi}{4}R^2H) \qquad (15)$$

Where: R-- diameter of a TCA tower, m, H--the length of calculation field, m.

Results and discussions

Primary data. The TCA tower designed and fabricated by our own was showed in **Figure 1**, which was equipped with a horizontal chain boiler with the nominal output capability of 1t/h.

The calculated field was regulated as the section between the board upside and the mist eliminator inlet bottom. The height is 5cm, tower diameter is 0.6cm, inlet flue gas temperature was 150ºC, wall surface temperature was 20ºC, the calculation grid field was plot evens, Δx=0.1m, Δγ=0.5m.The velocity field and some else data were come from literature cited [2].
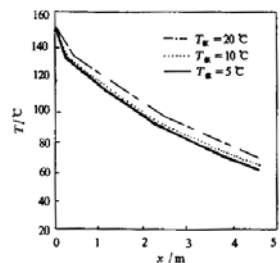
Temperature distribution. The temperature distribution in the TCA was calculated under the conditions of spray slurry temperature is 5ºC, 10ºC, 20ºC, respectively, and simulated results was shown in **Figure 2~Figure 4**, respectively.
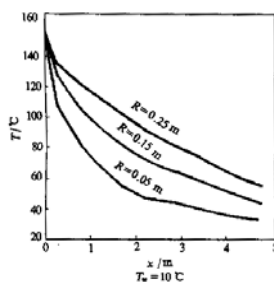
Figure 2. Temperature distribution along the height of TCA tower
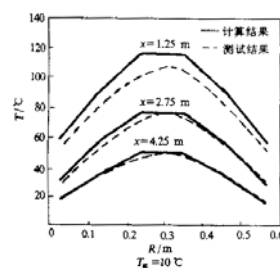
Figure 3. Temperature distribution along radial direction of TCA

Figure 4. Temperature distribution of axis direction along the height of tower at different spray slurry temperature in the TCA tower

As can be seen from **Figure 2**, the temperature is decreased along the height of the TCA tower. Further, the range of decrease is comparatively higher at the bottom of tower, while the range of decrease is comparatively lower at the top of the tower.

As can be seen from **Figure 3**, the temperature gradually increases from the wall surface to the center. The temperature gradient nearby the wall surface is very large, and the trend gradually becomes weakened along the height of tower, the temperature gradient near the center areas is comparatively lower.

As can be seen from **Figure 4**, with the decrease of spray slurry temperature, the temperature within TCA tower decline, and the trend of decrease is almost the same.

The experiment results showed in **Figure 3** were compared with the calculated results, the calculation results are relatively higher than that of experiments in general, and the errors decreases gradually along the height of tower. The overall trends of the calculation curves agreed well with that of test, and the two curves were almost superposition in the middle-top of TCA tower.

Conclusions

The temperature field distribution in TCA tower was investigated through numerical simulation and calculation. The calculation result agreed with the experimental results by in general. It implied that the selection of calculation model and the disposal of source terms were reasonable and feasible. The calculation models could offer the prediction for the temperature field, and the calculation results could use as reference for chemical reaction dynamics research and the design and operation of TCA tower.

References

(1) The State Environmental Protection Agency (SEPA). Report On the State of the Environment In China 2003, 2004.7
(2) Liu Z., Numerical Calculation of the 3-Dimensional Flow Field within Turbulent Contract Absorber Column, master thesis, 1996.11

# STRAINED HYDROCARBONS AS POTENTIAL HYPERGOLIC FUELS

W. Eccles, P. Kaszynski, R. Gostowski, B. Stulgies

Vanderbilt University, Nashville, TN

Overview

We are in search of a storable combination of high-energy hypergolic fuel and oxidizer to increase the efficiency of RLVs. The proposed fuel should increase the amount of energy provided per unit volume of fuel, eliminate the need of toxic oxidizers such as nitric acid, and eliminate the need of an inorganic catalyst. Amines, boranes, and phosphorus functional groups have been found to induce hypergolicity with nitric acid based oxidizers[1]. Initially, the project focus was on the synthesis of polycyclic systems, such as triangulanes and cubanes. A combination of strain and functional groups will perhaps create the desired fuel system.

Compounds **4**, **5**, and **8** were synthesized[2,3,4] and tested (Scheme 1). Compounds **8** and **5** did not ignite upon addition of H_2O_2 and 4 required addition of a catalyst.
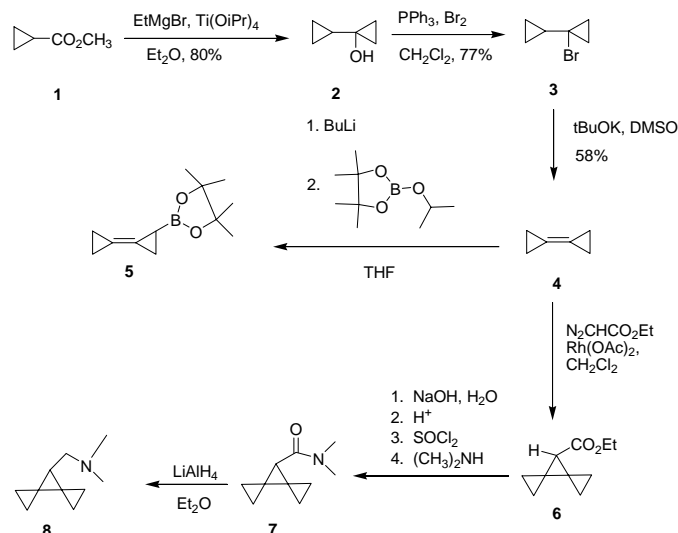
Scheme1.

These results are presumably due to vapor pressure, H_2O_2 miscibility, and amine substitution of the fuel. Thus, a new approach has been taken to the project. Synthesis of lower molecular weight amines such as those seen in Figure 1 has begun. These compounds will be tested and compared to their corresponding straight chain amines. Most of these compounds are commercial and all are known.
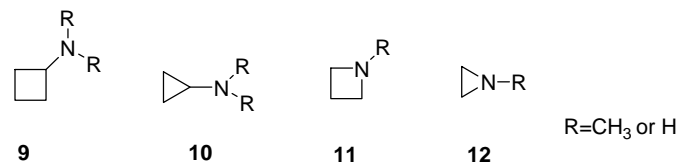

R=CH_3 or H

Figure 1.

References

(1) Rapp, L. R.; Resseler, D. "Investigation of the Correlation between Chemical Structure of Propellants and Self-Ignition for Nitric Acid and Hydrogen Peroxide Oxidizers," Reaction Motors Inc., 1952.
(2) de Meijere, A.; Kozhushkov, S. I.; Späth, T. *Org. Syn.* **2003**, *78*, 142.
(3) Löhr, S.; de Meijere, A. *Synlett.* **2001**, *4*, 489.
(4) de Meijere, A.; Kozhushkov, S. I.; Spaeth, T.; Zefirov, N. S. *J. Org. Chem.* **1993**, *58*, 502.

NOVEL CYANINE DYES WITH DIFFERENT METHINE CHAINS AS SENSITIZERS FOR NANOCRYSTALLINE SOLAR CELL

Xiuying Chen[a], Xiaojun Peng[a,], Yongqian Xu[a], Lei Shi[a], Chunli Liang, Shiguo Sun[a]*

[a]State key laboratory of fine chemicals, Dalian University of Technology, Dalian 116012, PR China

Jiahao Guo[b], c, Min Guo[b], Shengmin Cai[b],*

[b]College of Chemistry and Molecular Engineering, Peking University, Beijing 100871, PR China
[c]Department of Chemistry, China West Normal University, Sichuan Nanchong 637002, PR China

Introduction

Increasing attention[1,2] has been focused on nanocrystalline TiO_2 electrode sensitized by organic photosensitized dye since Grätzel[3] utilized cis-Ru[4,4'-(LL)]$_2$(NCS)$_2$ (L=2,2'-bipyridyl-4,4'-dicarboxylate) to sensitized TiO_2 nanocrystalline and photoelectric transfer efficiency can be up to 10%. Compared to the ruthenium bipyridyl complex, organic dyes are easier to be synthesized and cost less. Recently, organic dye sensitized TiO_2 solar cells have made great progress, and the highest overall yield of solar cells sensitized by organic dyes has exceeded 6%.[4,5] To obtain high efficient photosensitizer for solar cells material, the investigation on new dyes with improved molecular structure is necessary. Cyanine dyes have intense and broad absorption band in the visible and near-infrared regions, excellent sensitizing properties in photography. However, few works have been done on their application as sensitizers for solar cells. Sayama studied merocyanines with different chain length (-(CH2)n-COOH) anchoring on TiO_2 surface via ester group and found that IPCE value of the TiO_2 electrode sensitized by various dyes increased with the decrease of the distance from dye chromophore to TiO_2 surface, which is very worthwhile to design a new sensitizer.[6] Simultaneously, they found that the increase of methine chain (-(CH=CH)m-) of the dyes enhances the difficulty of the electron transfer from the excited dye to the conduction band of TiO_2.[7] As organic sensitizers for nanocrystalline solar cell material, the high photostabilities of the dyes play a significant role in photoelectrochemical introduing of large benzyl group on nitrogen atom improved the photostability greatly.[8] In this article, we report the synthesis and photoelectric properties of novel cyanine dye (Cyb3) and squarylium dye (Sqb) with common 3H-indole-N-carboxylbenzyl groups anchoring on nano-TiO_2, and two different kinds of methine chains.
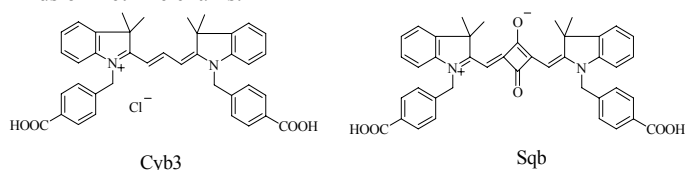
Figure 1. Chemical structures of Sqb and Cyb3

Experimental

Materials and instruments. Oxide of indium and stannum were used as the photoanode electric fundus. (South Glass Science and Technology Holding Ltd., China). All other chemicals and solvents involved were analytical reagents of the highest available purity. Redistilled water was used for the solution. ^{1}H NMR spectra were recorded on a Varian INOVA 400M NMR spectrometer, and elemental analysis were performed on a PE 2400 Ⅱ elemental analyzer.

Syntheses. 2,3,3-Trimethyl-3H-Indolenine (**1**) was synthesized according to the reference.[9]

N-(4-Carboxyl)benzyl-3,3-dimethyl-3H-indolenine quaternary salt (**2**): 1.59g(10mmol) of **1** and 1.8g(10.1mmol) of p-chloromethyl benzoic acid were added into 25ml flask containing 10ml o-dichlorobenzene under N_2. After heating the mixture at 110°C for 12h, the precipitate was filtered and washed with acetone. 1.9g of rose pink powder was obtained with no further purification, and the crude yield was 58%.

Sqb: 0.658g (2mmol) indolenine quaternary salt (**2**) and 0.114g (1mmol) squaric acid were heated in butanol (9ml)/toluene (9ml) mixture solvents with 5ml pyridine as catalyst for 6h.[10] The resulting precipitate was filtered and recrystallized from acetic acid to give 0.271g of blue powder with 40% yield. Elemental analysis: calcd for $C_{42}H_{36}N_2O_6$ (%), C, 75.89; H, 5.46; N, 4.21; found, C, 75.81, H, 4.92, N, 3.95. ^{1}H NMR (400MHz, DMSO): δ=1.72(s, 12H, C(CH$_3$)$_2$),5.48(s, 4H, N-CH$_2$), 5.77(s, 2H,=CH), 7.18(t, 2H, Ar-H), 7.26(m, 4H, Ar-H), 7.31(d, 4H, Ar-H, J=8Hz), 7.55(d, 2H, Ar-H, J=7.6Hz), 7.93(d, 4H, Ar-H, J=8Hz).

Cyb3: 0.658g (2mmol) of **2** was added into 25ml flask containing 8ml pyridine under N_2. After refluxing for 10 min, 0.9ml (6mmol) trimethyl orthoformate was added by portions. The resulting precipitate was recrystallized from acetone to give 0.750g pink product with 60% yield. Elemental analysis: calcd for $C_{39}H_{37}ClN_2O_4$ (%), C, 73.98; H, 5.89; N, 4.42; found, C, 73.42, H, 5.23, N, 4.12. ^{1}H NMR (400MHz, DMSO): δ=1.73(s, 12H, C(CH$_3$)$_2$), 5.49(s, 4H, N-CH$_2$), 6.44(d, 2H, CH=CH, J=13Hz),7.29(m, 10H, Ar-H), 7.68(d, 2H, Ar-H, J=7.6Hz), 7.92(d, 4H, Ar-H, J=8Hz), 8.36(t, 1H, Ar-H, J=13Hz).

Preparation of nanoparticle colloid solution and nanocrystalline TiO2 electrode. The preparation of TiO_2 nanoparticle colloid solution was prepared as described in referenc.[11] A conductive glass of 2cm×2cm cleaned by redistilled water was coated by TiO_2 nanoparticle colloid uniformly, and then heated to 450°C for 30 min in the air, cooled down to room temperature (forming non-sensitized electrode) or to 80°C, immediately soaked in the methanol with concentration of 0.5mmolL^{-1} dye for 12h at room temperature, washed in ethanol, and finally dried in the air (forming sensitized electrode). The amount of adsorbed dye was determined by spectroscopic measurement of dye desorbed from the semiconductor surface in the dilute methanol solution of KOH. Film thickness was confirmed using a DEKTAK step apparatus.

Photoelectrochemical experiments. Photoelectrochemical measurements were made with a thin-layer solar cell comprising a nanocrystalline TiO_2 working electrode and a thin platinum layer sputtered on conducting glass as counter electrode. The redox electrolyte solution consisted of a mixture of LiI (0.3molL^{-1}), I_2 (0.03molL^{-1}) and PC (1,2-propanediol carbonate) as the solvent. The area of the semiconductor electrodes was 0.27×0.27cm^2. In photocurrent-photovoltage characteristics measurement, a 150W xenon lamp served as a light source. A high-intensity grating monochromator (DWA10, Optical instrument Factory, Beijing, China) was introduced into the path of the excitation beam to produce incident monochromatic light. Electrochemistry workstation (CHI650A, Chenhua instrument Company, Shanghai) was used to measure the working curve of the photoelectrode and white light as incident light. Light intensity meter (Model 550-1) was used and photocurrent reaction spectrum was corrected to normalization for light source spectrum. A three-electrode cell was composed of a platinum wire as working electrode, a platinum slice as counter

electrode, and Ag/AgCl as reference electrode. The supporting electrolyte was $NaClO_4$ (0.1mmolL^{-1}).

Characterization of absorption spectra. JASCO V550 UV-Vis and PTI-700 spectrophotometer were used to measure the absorption and emission spectra of the two dyes in methanol and sensitized electrode. References are methanol and indium stannum oxide conductive glass. All measurements were performed at room temperature.

Results and Discussion

Synthesis and UV-Vis spectral properties of Sqb and Cyb3 in solution. Cyb3 and Sqb with different methine chains have been synthesized (**Scheme 1**). The dyes can anchor on nano-TiO$_2$ surface via *N*-carboxylbenzyl group.
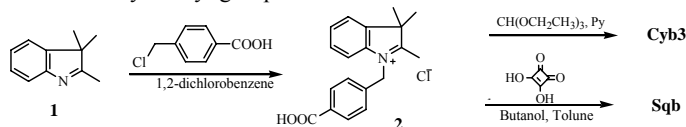
Scheme 1. Synthesis routes of Sqb and Cyb3

The absorption spectra of the two dyes in methanol are shown in **Figure 2**. The spectral properties are summarized in **Table 1**. The λ^{abs}_{max} are 554 and 632 nm in methanol respectively, with a little negative solvatochromism from methanol to chloroform as solvent. The λ^{em}_{max} of Cyb3 is 573 nm with Stockes shift ($\Delta\lambda$) 19nm in methanol. For Sqb, however, $\Delta\lambda$ is only 13 nm with λ^{em}_{max} 645nm in methanol. Compared to Cyb3, λ^{abs}_{max} of Sqb shifts to the longer wavelength by ca. 80nm with increasing length of the conjugated methine chain.
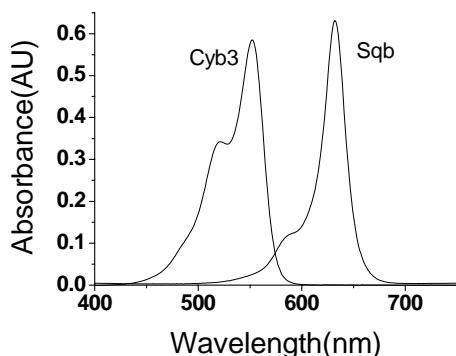
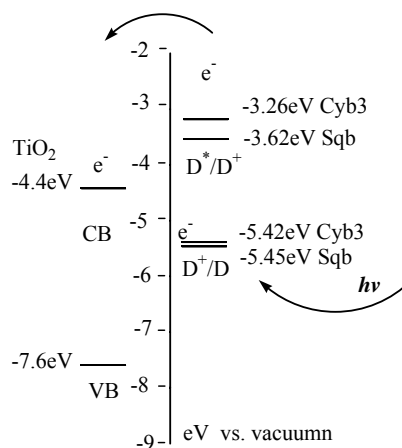**Figure 2.** Absorption spectra of Cyb3 and Sqb in methanol

Table 1. Spectral properties of Cyb3 and Sqb in different solvents

Solvent	Cyb3			Sqb		
	λ^{abs}_{max} (nm)	λ^{em}_{max} (nm)	$\Delta\lambda$ (nm)	λ^{abs}_{max} (nm)	λ^{em}_{max} (nm)	$\Delta\lambda$ (nm)
Methanol	554	573	19	632	645	13
Ethanol	560	577	17	636	649	13
Acetonitrile	550	571	20	634	647	13
Chloroform	561	581	22	637	649	12

Energy level diagram. To judge the possibility of electron transfer from the excited dye molecules to the conductive band of TiO$_2$, cyclic voltammograms was performed to determine the redox potentials for the two dyes. Redox potentials of 0.37V (vs. SCE) or 0.61V(vs. NHE) or -5.45eV (vs. vacuum) and 0.32V(vs. SCE) or 0.58V(vs. NHS) or -5.42eV (vs. vacuum) averaging the related

oxidation and reduction potentials are roughly regarded as the energy level of the ground state ($E^0(D^+/D)$) for Sqb and Cyb3 dye respectively. Considering the UV-Vis absorption spectra, the lowest energy of the excited state ($E^0(D^*/D^+)$) of the two dyes are about -3.62eV (vs. vacuum) and -3.26eV (vs. vacuum) (**eq.1**). Major absorption at 550-680nm and 450-570nm wavelengths corresponding to the energy difference between the ground state and the lowest excited state (*Eg*) of 1.83eV and 2.16eV for Sqb and Cyb3 respectively. Fig.3 shows the energy level diagram of the two dyes in methanol. Obviously, the excited-state energy levels for the two dyes are more negative than the energy level of TiO$_2$ conductive band edge (-4.4eV, vs. vacuum),[1,12,13] suggesting that the electron injection should be possible thermodynamically. The driving force for charge displacement into the oxide is about 0.99eV and 1.35eV for Sqb and Cyb3 respectively. The redox potential of Sqb is less positive than the corresponding potential of Cyb3. The excited state of Sqb matches better the lower bound of the conduction band of the semiconductor than the LUMO of Cyb3, thus decreasing the energy loss during the electron transfer process.

$$E^0(D^*/D^+)= E^0(D^+/D)+Eg \qquad \text{(eq.1)}$$
$$\text{Dye}$$

Figure 3. Energy level diagram for Cyb3 and Sqb

Absorption spectra of the two dyes on TiO$_2$ electrode. The absorption peaks of the two dyes on TiO$_2$ films are all extremely broadened (**Fig.4**), compared with their corresponding absorption peaks in methanol. It suggests that the dye molecules have formed H-aggregate or J-aggregate.[14] **Fig.5** is the proposed structure based on the geometry of the single crystal molecule (unpublished data). The dye moiety performs a plane due to the conjugated molecular structure and with the tilted large carboxylbenzyl group linked to the TiO$_2$ film surface via carboxylate form. To obtain the exact thickness of film and the optimal sensitized time, different sensitized conditions were investigated. 6.5μm thickness of film and sensitized time of 4h and 6h for Cyb3 and Sqb are obtained respectively.
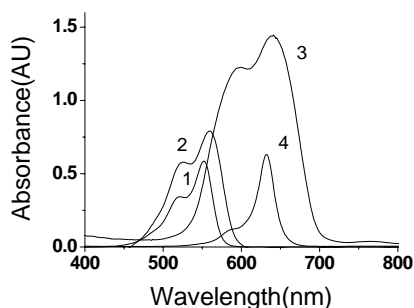
**Figure 4.** (**1**) absorption spectrum of Cyb3 in methanol, (**2**) absorption spectrum of TiO$_2$ electrode sensitized by Cyb3, (**3**) absorption spectrum of TiO$_2$ electrode sensitized by Sqb, and (**4**) absorption spectrum of Sqb in methanol. All electrodes were dried in air. Dyes were adsorbed in methanol solution (5×10^{-4}M). Total amount of the adsorbed dye was ca. 0.96×10^{-8}mol/cm^2 for Cyb3, 1.9×10^{-8}mol/cm^2 for Sqb respectively.
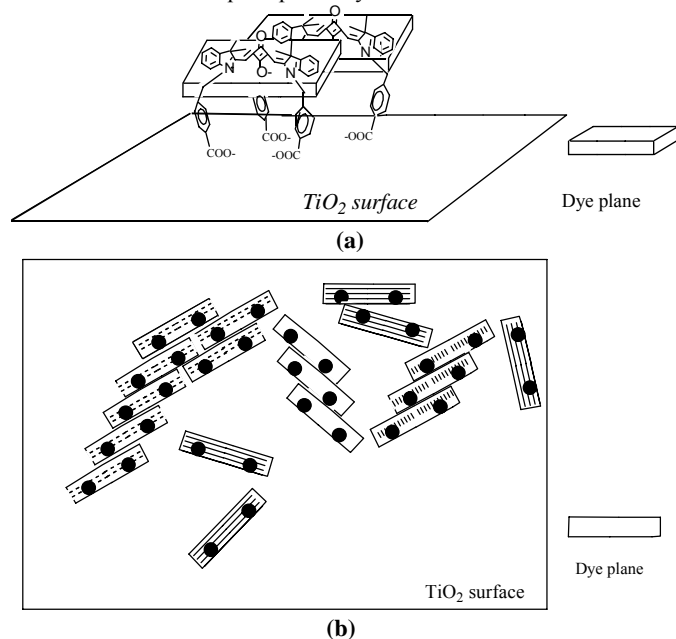
Figure 5. (**a**): Proposed structure of the aggregated dyes on TiO$_2$ surface (**b**): top view of the J-aggregated dyes on TiO$_2$ surface, closed circle is the carboxylbenzyl group anchoring on TiO$_2$ surface.

Photocurrent action spectra. Fig.6 demonstrates the photocurrent action spectra of the dye-sensitized nanocrystalline TiO$_2$ electrodes normalized by incident light intensity for the two dyes. Sqb shows high light harvesting ability in the red visible region above 600nm, which indicates that Sqb can expand the photoresponse of large band gap semiconductor TiO$_2$ into the red visible region. Comparing the action spectra with the absorption spectra of TiO$_2$ electrode sensitized by the dyes (**Fig.4**), the two dyes have spectra selectivity for different regions of visible light. Cyb3 converts more efficiently the light in the shorter wavelength region, but Sqb does in the long wavelength region. The action spectra and the absorption spectra of the two dyes resemble well, which indicates that the photocurrent is generated by the injection of electrons from the excited molecules into the conduction band of the TiO$_2$ electrode. Cyb3 and Sqb convert visible light to photocurrent in the region from 400 to 600nm and 550 to 700nm. The maximum IPCE values for

Cyb3 and Sqb are about 36% and 46% respectively. The latter is 1.3 times much higher than that of the former. Therefore, Sqb has higher electron injection efficiency than Cyb3 dye.
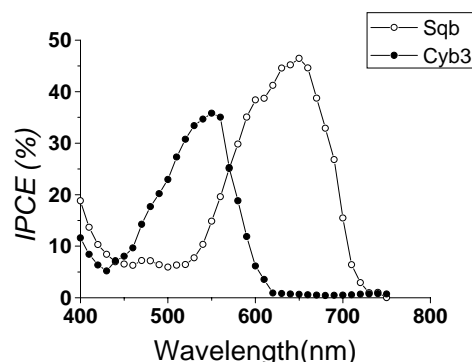
Figure 6. Action spectra of the two dyes sensitized TiO$_2$ electrodes

IPCE is the monochromatic incident photon-to-current conversion efficiency, defined as the number of electrons injected by the excited dye in the external circuit decided by the number of incident photons, is observed from the short-circuit photocurrents recorded at various excited wavelengths by means of the following expression:

$$IPCE(\%) = I/P_{in}(1240/\lambda), \qquad (2)$$

Where I is the short-circuit photocurrent (μA/cm^2), P_{in} is the incident light intensity (μW/cm^2) and λ is the excitation wavelength(nm).

Photocurrent-photovoltage characteristics curve and photoelectrochemical solar cells. The photocurrent and photovoltage curves are shown in **Fig.7**. The photoelectrochemical properties of dye sensitized TiO$_2$ electrode are given in **Table 2.**

Based on the characteristics curve, fill factor FF and the whole photo-electro transfer efficient η are obtained. FF is defined as

$$FF = P_{max}/(V_{oc} \cdot I_{sc}) \qquad (3)$$

Where P_{max} is the largest output power of solar cells, I_{sc} is the short-circuit photocurrent, V_{oc} is the open-circuit photovoltage, η is defined as

$$\eta = (FF \cdot V_{oc} \cdot I_{sc})/P_{in} \qquad (4)$$

Where P_{in} is the input power.

From Table 2, the I_{sc} (2.76mA/cm^2), IPCE (46%) and η (1.7%) of Sqb sensitized TiO$_2$ solar cell performs preferable IPCE values to Cyb3 sensitized one.

Several reasons were considered to lead to the different photoelectric properties of the two TiO$_2$ electrodes sensitized by Sqb and Cyb3. Firstly, as a sensitizer for solar cells material, it must possess the high photostability. In Sqb dye structure, Squarylium ring substituted the conjugated chain, which leads to the dye more stable under irradiation.[15] And spectrum range of Sqb shifts to the long wavelength region, which is favorable to absorb solar light. Moreover, the lowest excited energy level of Sqb dye matches well to that of TiO$_2$ nanoparticle conductive band gap (**Fig.3**). And the photoisomerization is one of the major decay pathways for methine dyes.[16] Sqb with methine chain substituted by squaric acid ring reduces cis-trans isomers. It is favorable to form ordered orientation on TiO$_2$ surface so as to increase the electron injection efficiency obviously.
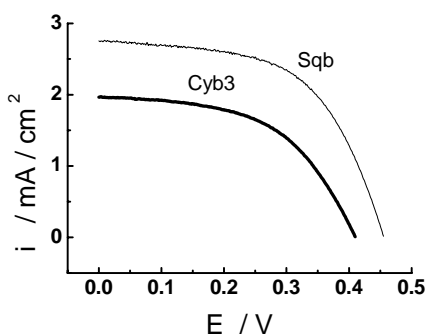
Figure 7. Photocurrent and photovoltage curves

Table 2. Parameters of the dye sensitized solar cells

	I_{SC}[a] / mA·cm^{-2}	V_{OC}[b] / mV	FF[c]	η /%	T[d]/ hour
Cyb3	1.97	410	0.527	1.01	4
Sqb	2.76	455	0.567	1.70	6

(a) I_{SC} is the short-circuit photocurrent

(b) V_{OC} is the open-circuit voltage

(c) FF is the fill factor of cell

(d) T is the sensitized time, and film thickness is 6.5μm, irradiated by 42mWcm^{-2} white light.

Conclusions

In this article, we synthesized two novel cyanine dyes to be used as the sensitizer for solar cells material. The photoelectrochemical properties of TiO_2 nanocrystalline solar cells sensitized by the two dyes were investigated. The I_{sc} (2.76mA/cm^2), IPCE (46%) and η (1.7%) of Sqb sensitized TiO_2 solar cell performs preferable IPCE values to that of Cyb3 sensitized one. The relationship of the molecule structure and the photoelectric properties were discussed, which is important to design an efficient molecule sensitizer.

Acknowledgement

References

(1) Hagfeldt, A.; Grätzel, M., *Chem. Rev.*, **1995**, *95*, 49.

(2) Nazeeruddin, M. K.; Kay, A.; Rodicio, K.; Humphry-Baker, T.; Muller, E.; Liska, P.; Vlachopoulos N.; and Grätzel, M., *J. Am. Chem. Soc.* **1993**, *115*, 6382.

(3) Regan, O. B.; Grätzel M., *Nature.* **1991**, *353*, 737.

(4) Hara, K.; Sayama, K.; Ohga, Y.; Shinpo, A.; Suga S.; and Arakawa, H., *Chem. Commun.* **2001**, *6*, 569-570.

(5) Kitamura, T.; Ikeda, M.; Shigaki, K.; Inoue, T.; Anderson, N. A.; Ai, X.; Lian, T. Q.; Yanagida, S., *Chem. Mater.* **2004**, *16*, 1806-1812.

(6) Sayama, K.; Tsukagoshi, S.; Hara, K.; Ohga, Y.; Shinpou, A.; Abe, Y.; Suga, S.; Arakawa, H., *J. Phys. Chem. B.* **2002**, *106*, 1363-1371.

(7) Sayama, K.; Tsukagoshi, S.; Mori, T.; Hara, K.; Ohga, Y.; Shinpou, A.; Abe, Y.; Suga, S.; Arakawa, H., *Sol. Energy Mater. Sol. Cells.* **2003**, *80*, 47-71.

(8) Chen, X.; Yao, Z. G., *Chemical Journal of Chinese Universities.* **1996**, *17*, 1613-1616.

(9) Mujumdar, R. B.; Ernst, L.A.; Mujumdar, S. R.; Lewis, C.J.; Waggoner, A.S., *Bioconjugate Chem.* **1993**, *4*, 105.

(10) Sprenger, H. E.; Ziegenbeim, W., Angew. *Chem. Internat. Edit.* **1967**, *6*, 553.

(11) Shen, Y. C.; Wang, L., Lu, Z. H.; Wei, Y., *Chinese J. Materials Research.* **1995**, *9*, 81.

(12) Liska, P.; Ulachopoulos, N., *J. Am. Chem. Soc.* **1988**, *110*, 3686.

(13) Vogel, R.; Hoyer, P.; Weller, H., *J. Phys. Chem.* **1994**, *98*, 3183.

(14) Mishra, A.; Behera, R. K.; Behera, P. K.; Mishra, B. K.; Behera, G. B., *Chem. Rev.* **2000**, *100*, 1973.

(15) Wang, W.; Yao, Z. G., *Photographic Science and Photochemistry.* 1997, *15*, 321-326.

(16) Khazraji, A. C.; Hotchandani, S.; Das, S.; Kamat, P. V., *J. Phys. Chem. B.* **1999**, *103*, 4693.